# AEROELASTIC EFFECTS OF MISTUNING AND COUPLING IN TURBOMACHINERY BLADINGS

THÈSE N$^o$ 2629 (2002)

PRÉSENTÉE À LA FACULTÉ DES SCIENCES ET TECHNIQUES DE L'INGÉNIEUR

SECTION DE GÉNIE MÉCANIQUE

## ÉCOLE POLYTECHNIQUE FÉDÉRALE DE LAUSANNE

POUR L'OBTENTION DU GRADE DE DOCTEUR ÈS SCIENCES TECHNIQUES

PAR

## Gerhard KAHL

Diplom-Ingenieur, Universität Hannover, Allemagne
et de nationalité allemande

accepté sur proposition du jury:

Prof. A. Bölcs, directeur de thèse
Dr V. Carstens, rapporteur
Prof. M. Deville, rapporteur
Dr T. Sommer, rapporteur

Lausanne, EPFL
2002

## Acknowledgements

The present study was conducted during my work at the Aeroelasticity and Acoustics Department of MTU Aero Engines in Munich. In this position, I have benefited from an atmosphere of creative curiosity. I would like to thank my head of department, Dr. Klaus Heinig, for always giving me the liberty to exploit the new ideas that were sparked by the tasks he assigned me to. Similarly, the many discussions with my colleagues have been of great value, viewing seemingly dead-ended topics from a fresh angle or making me aware of inconsistencies or weaknesses in my approach that I would otherwise have overlooked.

Nevertheless, this work would have remained piecemeal and would not have condensed into a thesis, had it not been for Prof. Albin Bölcs of the Laboratoire Thermique Apliquée et de Turbomachines at the Swiss Federal Institute of Technology in Lausanne (LTT-EPFL). With a (figurative) kick in the backside and with a little assistance from Prof. Torsten Fransson of KTH in Stockholm, he set me in motion in the right direction to bring this work to fruition. I am very grateful for his continued support and for giving me the opportunity to finish and present this thesis at the LTT.

During the times I worked at the LTT as well as in many phone calls and email threads, I have enjoyed the multi-national, friendly and open atmosphere and the assistance of all the staff. I would especially like to thank Dr. Peter Ott for his efforts to help me convert this thesis into something readable and (hopefully) understandable and Mrs. Annick Despont for quietly moving all those little administrative obstacles out of my way that I would inevitably have run into. This has sped up my progress immensely.

Finally, a large part of the credit goes to my family: My parents brought me up in a stable, enriching environment and supplied me with a solid foundation through my education. In the time of writing the thesis, my wife Kirsten supported me all the way through this work. When I could not spend enough time with the family, she always made up for it and took a lot of the burden on herself. Finally, my fabulous kids Karina and Ulrike never lost their good humour, even at times when I had so many other things on my mind ("What's he gonna be – a doctor? Cool!").

Thank you all - without you, I would not have made it.

## Abstract

A numerical method has been developed to study the effects of structural mistuning on the aeroelastic behaviour of turbomachinery cascades.

The specific objectives of the work presented here were the following:

- A method was to be developed that can assess the major effects of structural mistuning in a cascade in sub- and transonic flow situations.
- The influence of mechanical and aerodynamic coupling between the blades as well as coupling between multiple modes for each blade was to be included.
- Accurate representations of the aerodynamic forces, taken from a modern three-dimensional unsteady aerodynamic solver were to be used.
- The method should be applicable for design use, meaning that it has to supply results quickly for a large number of configurations.
- The applicability and accuracy of the method was to be demonstrated by comparison of numerical results to available data from recent experiments.
- The influence of major parameters on the aeroelastic stability and on the resonant amplitude of representative test cases should be assessed.

The approach used to achieve these goals is the combination of a linearised Euler method for the aerodynamic calculations with a modal reduction technique, where the structural properties of each blade are represented by only a few eigenmodes. The method is validated and applied to two test cases, comprising of a transonic compressor rotor and a high pressure turbine rotor. Both are representative of modern turbomachinery designs.

The final conclusions of this work are:

- The newly developed method is capable to assess the dominant effects of structural mistuning in turbomachinery cascades, including the mechanical and aerodynamic coupling of adjacent blades and the aerodynamic coupling of multiple modes with arbitrarily complex modeshapes.
- In this method, the aerodynamic characteristics of the cascade are accurately represented using the generalised unsteady aerodynamic coefficients derived from a modern three-dimensional flow solver, applicable to and validated for both sub- and transonic configurations.

- The simplifications employed significantly contribute to the computational efficiency of the method, making it applicable for design purposes as well as for the assessment of large parametric variations or for statistical studies of stochastically mistuned configurations.
- The current method is successfully validated by a comparison of numerical to experimental data. The applicability and accuracy is demonstrated by the favourable agreement between measured and computed results.
- Based on these validations, the method is applied to study the influence of major parameters on the aeroelastic behaviour of the selected test cases. The results show a wide range of phenomena, dependent on the type and strength of mistuning, frequency, modeshape and interblade phase angle. The results highlight the close inter-dependence of the aeroelastic stability derived from the eigenvalue analysis and the resonant amplitudes derived from the forced response analysis.

## **Zusammenfassung**

Ein numerisches Verfahren wurde entwickelt, um den Einfluss kleiner Verstimmungen der strukturellen Eigenschaften von Turbomaschinen - Beschaufelungen auf deren aeroelastisches Verhalten zu untersuchen.
Die Ziele der hier vorgestellten Arbeiten waren:

- Ein Verfahren war zu entwickeln, welches die wesentlichen Effekte von struktureller Verstimmung in Beschaufelungen mit sub- und transsonischen Strömungen richtig wiedergibt.
- Der Einfluss mechanischer und aerodynamischer Kopplung zwischen den Schaufeln sowie der Kopplung zwischen verschiedenen Eigenformen der Schaufeln sollte berücksichtigt werden.
- Das Verfahrens musste auch bei komplexen dreidimensionalen, sub- und transsonischen Strömungszuständen anwendbar sein.
- Das zu entwickelnde Verfahren sollte für den Entwurfsprozess tauglich sein, also in kurzer Zeit Ergebnisse für eine große Anzahl verschiedener Konfigurationen liefern können.
- Die Anwendbarkeit und Genauigkeit des neu entwickelten Verfahrens war durch den Vergleich numerischer Ergebnisse mit experimentellen Resultaten zu zeigen.
- Der Einfluss der wesentlichen Parameter auf die aeroelastische Stabilität und auf die Resonanzamplituden unter Zwangserregung sollte an repräsentativen Testfällen untersucht werden.

Das zur Erreichung dieser Ziele gewählte Vorgehen besteht in der Kombination eines zeitlinearisierten Euler-Verfahrens zur instationären Strömungsberechnung mit einem modalen Ansatz, bei dem das strukturelle Verhalten jeder Schaufel durch wenige Eigenformen wiedergegeben wird.

Das Verfahren wurde auf zwei Testfälle angewandt und daran validiert. Dabei handelt es sich um einen transsonischen Verdichterrotor und den Rotor einer Hochdruckturbinen - Versuchsturbine. Beide entsprechen in ihrer Auslegung den Komponenten moderner Turbomaschinen.

Die wesentlichen Ergebnisse der vorliegenden Arbeit sind:

- Das neu entwickelte Verfahren ist in der Lage, die wesentlichen Effekte von Kopplung und Verstimmung in den Beschaufelungen von Turbomaschinen richtig zu erfassen, einschließlich der mechanischen Kopplung benachbarter Schaufeln und der aerodynamischen Kopplung unterschiedlicher Moden. Dabei bestehen keine Einschränkungen hinsichtlich der Komplexität der untersuchten Moden.

- Die verwendeten generalisierten Luftkraft-Koeffizienten liefern eine exakte Beschreibung des instationären Verhaltens der untersuchten Beschaufelungen. Die Koeffizienten werden mit Hilfe eines modernen dreidimensionalen Strömungslösers ermittelt, der für sub- wie auch transsonische Strömungen anwendbar und validiert ist.

- Die verwendeten Vereinfachungen tragen wesentlich zu der Geschwindigkeit des entwickelten Verfahrens bei. Dadurch wird einerseits die Anwendbarkeit im Auslegungsprozess ermöglicht, andererseits sind dadurch auch Parametervariationen oder statistische Untersuchungen stochastisch verstimmter Konfigurationen durchführbar.

- Das vorgestellte Verfahren ist durch den Vergleich numerischer Ergebnisse mit experimentellen Daten validiert. Die Anwendbarkeit und Genauigkeit wird durch die gute Übereinstimung zwischen Rechnungen und Messungen bestätigt.

- Abgesichert durch diese Validierungen wurde das Verfahren für verschiedene Parametervariationen angewandt, bei denen der Einfluss der wesentlichen Parameter auf das aeroelastische Verhalten der ausgewählten Testfälle untersucht wurde. Die Ergebnisse lassen eine Vielfalt verschiedener Phänomene erkennen, die große Unterschiede in Abhängigkeit von der Stärke der Verstimmung, der Frequenz, den Eigenformen und dem Phasendifferenzwinkel aufweisen. Insbesondere wird an vielen Ergebnissen das enge Zusammenspiel zwischen der Veränderung der aeroelastischen Eigenwerte und den Resonanzamplituden unter Zwangserregung deutlich.

**Table of Contents**

# 1   Introduction

## 1.1   Aeroelasticity in Turbomachines

Turbomachinery technology has made tremendous progress over the last decades, starting from the first steam turbines at the turn of the $20^{th}$ century, through the design of the first jet engines in the 1940s up to the high performance engines of today's modern power generation machines, bypass fan jet engines and supersonic fighter engines. Most of the impetus in these developments was sparked by the requirements of modern aircraft for reliable, efficient, affordable and environmentally acceptable propulsion systems. Especially aircraft engine design raises extremely demanding requirements that are more often than not fundamentally conflicting – try to reduce the overall engine weight while increasing the blade loads, necessitating heavier blades and discs; try to improve efficiency by increasing the turbine gas temperatures while at the same time lengthening the blade life and inspection intervals and reducing the manufacturing cost. On top of these complications, the available "design space" is in most cases strongly limited by considerations like maximum allowable material temperatures, restrictions on allowable engine length and diameter, or by tradeoffs between gains on efficiency and engine cost.

Finding an acceptable near-optimum design in this complex situation requires the designer to have access to highly sophisticated analysis tools for the prediction of the overall engine behaviour, for example in terms of flow, temperatures, stresses and vibrations. One of the major concerns in this context is the structural integrity of the engine under all operating conditions. The structural analysis tools – mostly based on commercially available Finite Element Method (FEM) systems, have reached impressive capabilities and fidelity, enabling the designer to calculate centrifugal loads, deformations and stresses under external loads or eigenfrequencies and eigenmodes of highly complex components or even complete assemblies. Similarly, the analysis of the flow through the bladings of the turbomachine can be predicted very accurately using modern methods of Computational Fluid Dynamics (CFD).

However, in many instances the merits or drawbacks of a particular design can only be judged when the various physical aspects can be assessed simultaneously using

inter-disciplinary analysis tools. A particular combination of such inter-disciplinary analysis concerns the interaction of the vibrational dynamics with the fluid dynamic forces and the structural elastic forces.

Arranging these three types of forces in a triangle, as in Fig. 1, clarifies the different disciplines defined by the interactions between these forces, for example, to study the structural vibrations of a certain configuration, knowledge of the elastic and inertial forces is required.
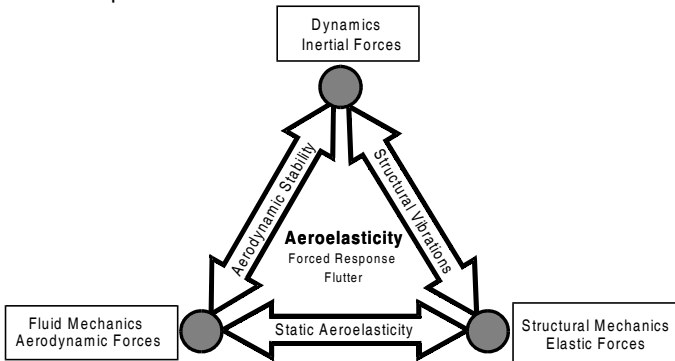


*Fig. 1: The Collar Triangle of aeroelastic forces*

This figure was first shown by Collar [14] in 1946, after whom it is referred to as the "Collar Triangle". It illustrates the definition of the term "aeroelasticity" as the interdisciplinary approach taking into account all three types of forces shown - elastic, inertial and aerodynamic. Today, the conventional Collar definition has been expanded to include forces derived from other sources as well, such as temperature induced stresses and control system inputs.

The parts of a turbomachine that are most strongly affected by aeroelastic phenomena are the bladings, where the high aerodynamic loads required to generate the energy transfer from the fluid to the rotating machinery or vice versa are paired with large structural loads and an inherently unsteady flow environment.

In this situation, the danger for the bladings is found in flow induced vibrations.

Two fundamentally different effects can cause flow induced vibrations in turbomachinery bladings. First, the relative motion of the stator and rotor blade rows leads to a situation where each blade row is subjected to an unsteady periodically disturbed flow due to the wakes of the upstream blade rows and the potential effect

of the downstream blade rows, as schematically shown in Fig. 2. This unsteady flow field leads to periodically unsteady forces acting on the blades, inducing blade vibrations. Due to the fact that this phenomenon is governed by the response of the vibrating structure to external forcing, it is referred to as "Forced Response".
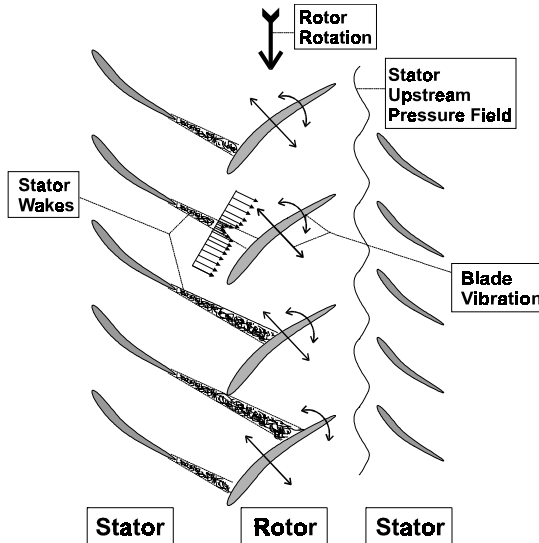


*Fig. 2: Sketch of a compressor rotor under up- and downstream disturbances*

The blade vibration amplitudes can grow to very high levels if the forcing frequency meets a structural resonance condition, i.e. if the forcing frequency coincides with a structural eigenfrequency of the blading. When the amplitudes are so high that the blade can sustain them only for a limited number of cycles, cracks will initiate in the blade structure after a certain time, leading ultimately to the failure of the blade due to so-called High Cycle Fatigue (HCF). The rotation speed of turbomachines is usually quite high – typically a few thousand rotations per minute (rpm), in some cases like small turbochargers even up to 100.000 rpm. Typical blade numbers of a stator or rotor cascade are commonly on the order of 60 to 120. The excitation frequency that a blade periodically passing through the wake of an upstream stator is subjected to, can be calculated by rotation speed times the number of stator airfoils. For a typical case of 6000 rpm and 100 stator airfoils, this amounts to 10,000 cycles per second (10 kHz). Due to these high frequencies, HCF failure can occur in

a very short time span, once the blade is subjected to the high vibration amplitudes in a resonance condition.

Such a blade failure, if it occurs in the jet engine of an airplane, will at least result in the shutdown of the engine, if not even in further damage on the airplane itself, if the blading fragments are not contained within the casing. Such a scenario definitely poses a safety risk for airplane passengers, even more so in the case of the increasingly popular twin-engined aircraft.

The second important aeroelastic effect that can be found in turbomachinery bladings is the appearance of self excited excitations. In this case, the structure is not subjected to external excitations, but encounters an instability through positive feedback of the vibration induced blade forces on the vibration itself. The fundamental mechanism is schematically shown in Fig. 3. Consider a cascade of airfoils as indicated at the top of the figure. In a turbomachinery environment, these airfoils will always perform slight oscillations, for example due to random excitation caused by flow turbulence. These oscillations alter the flow around the airfoils and consequently induce aerodynamic forces on the oscillating airfoils themselves as well as on the neighbouring airfoils in the cascade, as is indicated on the left part of the figure, for example due to the change in incidence on an airfoil performing a torsional motion.
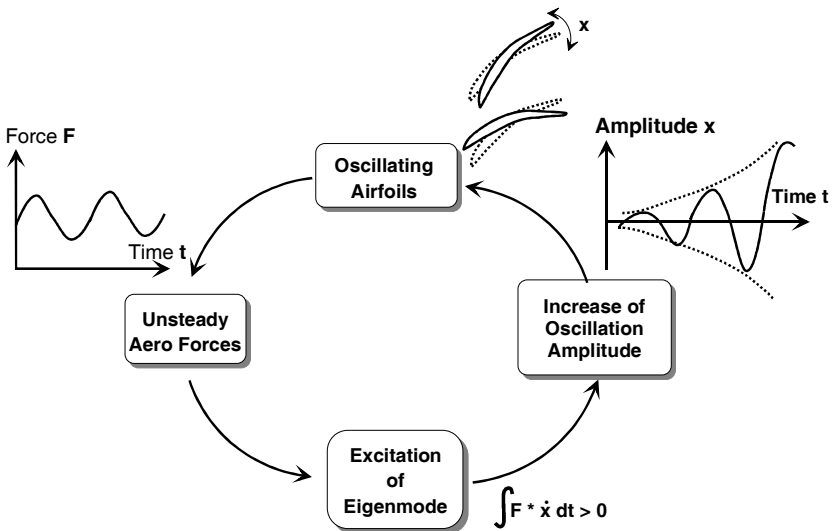


*Fig. 3: Schematic of the positive feedback loop leading to flutter in turbomachinery cascades.*

The effect that these unsteady aerodynamic forces have on the oscillation amplitudes depends on the relative time lag between the motion itself and the induced aerodynamic forces, which in turn is dependent on the specific flow conditions, frequency and modeshape of the oscillation, blade geometry and the temporal relation of the movements of the blades in the cascade. If the integral of force times velocity over one period of oscillation is negative, then energy is transferred from the oscillating structure into the flow, hence the amplitude of the oscillation decays – the oscillation is damped out. If however the same integral yields a positive value, then energy is transferred from the fluid into the oscillating structure, as indicated at the bottom of Fig. 3. In this case, the amplitude grows, as shown on the right of the figure. This increased amplitude consequently leads to increased unsteady aerodynamic forces, which further increase the amplitude and so on – the positive feedback loop is closed. This implies that small initial vibrations of the structure are not damped out, but grow exponentially, quickly leading to catastrophic HCF failure. This aeroelastic instability is generally known as flutter.

From the earliest turbomachine designs, the flow-induced destructive vibrations - either caused by forced response or by flutter - have troubled the designers. Numerous failures of experimental as well as of in-service engines have been traced to aeroelastic causes [30], and it has been estimated that up to 40% of the problems encountered during the development of modern aircraft gas turbine engines are related to HCF. Furthermore, HCF problems account for approximately 5% of commercial sector maintenance costs. In the military sector, HCF related maintenance costs are estimated to total in the billions of dollars over the next 20 years [40]. More importantly, these types of blade failures in aircraft applications, though rare, pose an obvious risk to passenger safety.

## 1.2   State of the art

Various analytical methods to assess the aeroelastic characteristics of turbomachinery bladings have been developed over the past decades, their increasing complexity mirroring the exponential growth of available computing power. In general, the more physical properties of the "real world" are contained in the models, the less input of empirical constants or calibration is needed for the application. Consequently, the simplest flutter clearance criteria, based on the

Strouhal number alone, require a large knowledge base from previous experience to yield sensible results for a new, untested design.

On the topic of the analysis of unsteady flows in vibrating cascades, more physical modelling was included in the flat plate models for unsteady cascade flow of Whitehead [59] and Smith [56]. These are strictly valid for infinite two-dimensional cascades in subsonic flow without blade thickness or flow turning and produce acceptable results when applied in a strip-theory manner for thin, lightly loaded, subsonic cascades. More realistic configurations could be analysed with the advent of the linearised potential methods of Verdon [59] or Whitehead [62]. Based on the assumption of two-dimensional, inviscid, irrotational but not homogeneous flow, the unsteady flow is modelled as a small perturbation to the time mean (steady) flow field. Both approaches were extended to include some three-dimensional effects on the steady flow through variable stream tube height and could also model weak shocks through a shock fitting [59] or a shock capturing [62] procedure. A different approach was taken by Namba [44], who included three dimensional effects but retained limitations on the blade loading in his Double Linearisation Theory (DLT).

In the following, the unsteady CFD community split up into two camps. A large amount of research was performed on non-linear time stepping methods. These were developed starting from two-dimensional Euler methods (e.g. Giles [21], He [25], Ott [47]) and have since been extended to highly sophisticated three dimensional, multi-stage Navier-Stokes methods. These methods hold the promise to be able to model all the important features of the highly complex unsteady flow situations in a turbomachinery blading, regardless of flow separation, shocks or large levels of unsteadiness. Two drawbacks, however, remain with these methods. The first is the amount of computing power required for such analyses. While the capabilities of modern computers have improved dramatically over the time, a single simulation using all the features of a modern non-linear time-stepping method may still take days or weeks to complete, even on high performance parallel computers. The second drawback of these methods is the immense amount of data produced by a single run, that may make the interpretation of the results almost as difficult as the analysis of the measurements in a highly instrumented rig test.

Both these problems make non-linear time stepping methods not so well suited for parametric studies where influence of various variables is to be assessed. For this purpose, the linearised methods are very useful and also very popular. Similar to the non-linear methods, their scope was extended from the mentioned potential

methods, through the pioneering work on linearised Euler Methods by Ni [45], taken up by Hall and Crawley [22], as well as Kahl and Klose [32] and Holmes and Chuang [27], extended to three dimensional linearised Euler by Hall and Lorence [23] and to Navier-Stokes by Holmes and Lorence [28]. Currently, these linearised methods are widely used in the industry, especially for flutter calculations, where a large number of cases have to be assessed in a reasonable time span.

Most of the aforementioned methods focus on the computation of the unsteady flow field in a rigid cascade under incoming unsteady flow disturbances or in a oscillating cascade undergoing prescribed harmonic motion, making them basically rather methods for unsteady aerodynamics than for aeroelasticity. The coupling to the structural behaviour of the vibrating cascades was mostly achieved through the calculation of energy transfer, determining whether a prescribed amplitude would increase or decrease. Only recently were simplified structural models included in the non-linear time stepping methods to perform coupled aero-mechanical simulations (e.g. Chew et al. [12] ).

While these analyses rely on the assumption of a perfectly symmetric structure, where all blades are structurally and aerodynamically identical, in practice small differences between the individual airfoils of a cascade are unavoidable. The reasons for these differences can be for example the manufacturing tolerances or slight differences in the way a blade firtree is seated in the disc. All these differences lead to small variations in the structural characteristics of the individual airfoils. Small as these variations may be, it has been found that their effects can be drastic. For example, strain gauge tests of complete rotors often show a spread in the measured response amplitudes of the different blades of a factor of more than two. Given the fact that mostly only a few blades are instrumented, this leads to the question what the true maximum amplitude of all blades might be, since this is what the design of the blade has to take into account. Furthermore, the question arises what the effect of the small structural variations on the aeroelastic stability may be, which can often not be measured as readily as the forced response amplitudes.

A large number of publications are assessing the effects of imperfections in the symmetry on the eigenmodes, eigenvalues and on the forced response of turbomachinery bladings. However, most of these analyses cover the structural aspects alone and neglect the unsteady aerodynamic effects, a notable exception being the works of Kielb and Kaza ([38] and [39]), where a simple flat 2D plate model is used to include the aerodynamic coupling effects.

Typical examples of the wide range of publications on the structural aspects of mistuning are the works of Afolabi ([1] and [2]), where the frequency response and the eigenvalue spectra of mistuned bladed disc assemblies are studied. A range of methods were devised to reduce the number of degrees of freedom necessary to capture the relevant system characteristics. These fall into two categories, either a component mode synthesis or a modal reduction. In the first case, the system is split into different components and the behaviour of the complete mistuned system is retrieved by a superposition of the modes of the subsystems with certain constraints applied at the interfaces. This approach is used in the classical Craig and Bampton method [15] and in variants thereof (e.g. Bladh et al, [4], [5], [6], Seinturier et al. [53], [54]). The second method is based on performing an analysis of the complete tuned system and then retaining only a few of the resulting modes for the analysis of the mistuned system (e.g. Yang and Griffin [63], Afolabi [1], [2]). In both cases, the mistuning is regularly applied to the generalised properties of the individual blade modes, assuming that the modeshapes themselves remain unaffected by these changes.

A comparison of the two methods has recently been published by Moyroud et al. [43], concluding that both approaches yield comparable results. It was also concluded that the modal reduction method is computationally more efficient, while the component mode synthesis method can be applied more flexibly to certain problems.

## 1.3    Goals of the present study

In the previously published studies, a number of limitations are apparent. In many cases the aerodynamic damping and coupling is neglected altogether ([4], [5], [6], [43], [52]) or is limited to two-dimensional rigid motions of the blade sections ([38], [39]). In other instances, the aerodynamic interaction between different structural modes is neglected ([53]).

In order to fill some of the gaps left by the previous researchers, the goals of the work presented here are the following:

- A method shall be supplied that can assess the major effects of mistuning and coupling in a cascade.
- The influence of mechanical and aerodynamic coupling is to be included.
- Multiple modes for each blade are to be considered.

- Sub- and transonic flow situations shall be addressed.
- Accurate representations of the aerodynamic forces, taken from a modern three-dimensional unsteady aerodynamic solver, shall be used.
- The proposed method must be applicable for design use, meaning that it has to supply results quickly for a large number of configurations.
- The applicability and accuracy of the method is to be demonstrated by comparison of numerical results to available data from recent experiments.
- The influence of major parameters on the aeroelastic stability and on the resonant amplitude of representative test cases shall be assessed.

The approach used to achieve these goals is the combination of a linearised Euler method for the aerodynamic calculations with a modal reduction technique. This method is an extension of the work presented by the author in [35], where some aspects of mistuning were studied for a configuration with a single mode per blade.

## 1.4   Structure of the thesis

The structure of this thesis is the following:
- In chapter 2, the theoretical background and the fundamental ideas of the proposed mistuning method are developed. The combined aero-elastic equations for free and forced vibration are set up and the projection to an eigenmode formulation is performed. Inclusion of structural and inter-modal aerodynamic coupling as well as the variability of aerodynamic coefficients with frequency are discussed.
- In chapter 3, the method is applied to the rotor of an existing compressor rig. After validation by comparison to the energy method, the influence of major parameters on the aeroelastic stability as well as on the resonant amplitudes under aerodynamic excitation is studied. For tuned configurations as well as for configurations with deterministic and stochastic mistuning of stiffness, damping and modal spacing, the aeroelastic characteristics of the compressor rotor are evaluated.
- Chapter 4 uses recently acquired experimental data from an HP turbine rig rotor to demonstrate the predictive capabilities of the current method for the mistuned forced response problem. Using the same rotor as a test case, additional parametric studies are performed. These are used to assess the

relevance of the comparison of experimental versus numerical results and to conclude on the generality of the findings from these comparisons.

- In chapter 5, the results are summarised, the key findings are assembled and some general conclusions are drawn.

- Finally, the appendices A, B and C contain the theory for calculating the generalised aerodynamic forces, a detailed description of the linearised Euler solver developed by the author and a derivation of a sideband intensity estimate. In Appendix D, the computational procedures and resource requirements are detailed. The information contained in the appendices is not essential for the central ideas of this thesis, but without this preliminary work the successful application of the mistuning methodology would not be feasible. As such, the appendices may be helpful for some readers who are interested in the details of the underlying methods and tools.

## 2   Structural mistuning and modal coupling

### 2.1   Identification of the problem

Most current structural, aerodynamic and aeroelastic analyses of turbomachinery cascades assume that all blades in a cascade are strictly identical with respect to their geometric shape as well as to their structural behaviour. In reality, many factors like inevitable manufacturing tolerances or material imperfections lead to blade-to-blade variations. Obviously, the small variations in the geometric or material properties will also be reflected in a slightly altered structural behaviour of the cascade. These variations, also termed structural mistuning, may in turn have a significant impact on the overall aeroelastic behaviour of the cascade, although their magnitude is seemingly minor. The purpose of this section is to present an analytical model that facilitates a study of the structural mistuning effects in more detail.

Strain gauge measurements in full-scale engines as well as in test rigs have often shown large variations of the resonance peak amplitude of the instrumented blades in a cascade, sometimes exceeding a factor of 2 between the maximum measured amplitudes of the blades. In most cases only a few blades in a cascade are instrumented with strain gauges, so that it is doubtful whether the blade exhibiting the highest amplitude in the whole cascade is captured by this approach. Consequently, it is important to understand the underlying effects leading to this large scatter in response amplitudes and to improve the predictive tools to include these effects reliably.

Modern turbomachinery bladings often feature a fairly complicated geometry. To assess their vibratory behaviour, advanced structural dynamic methods like FEM are needed. These methods rely on a discretisation of the structures, more often than not resulting in many thousands of degrees of freedom for the numerical model. Due to this complexity, certain simplifications from the "real world" are almost inevitably introduced in the analysis.

For example, blade-to-blade variations, like the ones resulting from manufacture imperfections, are usually neglected when analysing the vibratory behaviour of such cascades. Small as these imperfections may seem, they can nevertheless have significant effects on the structural and aeroelastic properties of the cascade. To be able to evaluate these effects, the number of degrees of freedom in the utilised model needs

to be drastically reduced. In the approach presented here, the deformation of the individual blades will therefore be described using a number of in-vacuo eigen-modeshapes as basis functions, this number being some orders of magnitude smaller than the number of degrees of freedom in the original FEM model.

## 2.2   Solution approach

The starting point of this analysis are the fundamental equations of motion in physical space and in the time domain for a discretised system of coupled blades, for example conforming to a FEM approach. For a linear elastic system, these can be formally written as

$$\tilde{\mathbf{M}}\ddot{\tilde{x}} + \tilde{\mathbf{D}}\dot{\tilde{x}} + (\tilde{\mathbf{K}} + \tilde{\mathbf{C}})\tilde{x} + \tilde{\tilde{F}}_c(\tilde{x},\dot{\tilde{x}}) = \tilde{\tilde{F}} \tag{1}$$

Here, $\tilde{\mathbf{M}}$, $\tilde{\mathbf{D}}$ and $\tilde{\mathbf{K}}$ are the mass, damping and stiffness matrices, respectively, while $\tilde{\tilde{F}}_c$ introduces the aerodynamic coupling between the blades and is dependent on the deflection and velocity of the blades. The damping is assumed to be of viscous type, i.e. the damping forces are proportional to the velocity. The right hand side, $\tilde{\tilde{F}}$, contains the external forces acting on the structure while the vector $\tilde{x}$ holds the displacement degrees of freedom for the finite elements of the complete model. For an accurate representation of the vibratory behaviour, the number of degrees of freedom (DOF) for a typical cascade will have to be on the order of more than 10,000 times the number of blades.

### 2.2.1  Structural analysis and blade eigenmodes

The common approach of structural mechanics to investigate the oscillatory behaviour of such a system is to perform an eigen-analysis of the undamped system in the absence of aerodynamic coupling forces and external excitations. This is often termed in-vacuo analysis, since it corresponds to the analysis of the structure as it would behave in a vacuum. In the case of periodic structures like turbomachinery bladings with identical blades, it is sufficient to analyse a single segment, e.g. a single blade with the corresponding sector of the disc. With the suffix $b$ indicating the specific blade being analysed, eq. (1) then reduces to

$$\tilde{\mathbf{M}}_b \ddot{\tilde{x}}_b + \tilde{\mathbf{K}}_b \tilde{x}_b = \vec{0} \tag{2}$$

With a harmonic assumption

$$\tilde{\vec{x}}_b(r,\Theta,z,t) = \vec{x}_b(r,\Theta,z)e^{i\omega t} \tag{3}$$

this can be written as

$$-\omega^2\tilde{\mathbf{M}}_b\vec{x}_b + \tilde{\mathbf{K}}_b\vec{x}_b = \vec{0} \tag{4}$$

and can be reduced to an eigenvalue problem

$$\left(\tilde{\mathbf{M}}_b^{-1}\tilde{\mathbf{K}}_b - \omega^2\mathbf{E}\right)\vec{x}_b = \vec{0} \tag{5}$$

where $\mathbf{E}$ denotes the unit matrix. Solving this problem yields the in-vacuo eigenmodes $\vec{\Phi}$ and eigenvalues $\omega$ (oscillation frequencies) of the blade / disc segment. Any deformation vector $\vec{x}_b$ on a specific blade $b$ can be expressed as a linear combination of theses eigenvectors $\vec{\Phi}$. By arranging all the eigenvectors in a matrix $\mathbf{\Phi} = \left[\vec{\Phi}_1, \vec{\Phi}_2,...,\vec{\Phi}_{DOF}\right]$ this is written as

$$\vec{x}_b = \mathbf{\Phi}\,\vec{a}_b \tag{6}$$

where $\vec{a}_b$ contains the respective factors by which the individual eigenvectors contribute to the deformation vector.

Since the mass and stiffness matrices are positive definite and non-singular, $\mathbf{\Phi}$ forms a set of orthogonal eigenvectors that can be used to diagonalise the original equation (4). Pre- multiplying with the Hermitian $\mathbf{\Phi}^*$ (conjugate-transpose) and inserting eq. (6) yields

$$-\omega^2\,\mathbf{\Phi}^*\tilde{\mathbf{M}}_b\mathbf{\Phi}\,\vec{a}_b + \mathbf{\Phi}^*\tilde{\mathbf{K}}_b\mathbf{\Phi}\,\vec{a}_b = \vec{0} \tag{7}$$

or

$$-\omega^2\mathbf{M}_b\,\vec{a}_b + \mathbf{K}_b\,\vec{a}_b = \vec{0} \tag{8}$$

Due to the properties of the eigenvector matrix $\mathbf{\Phi}$, eq. (8) constitutes a set of decoupled equations, each of which describes the behaviour of a single eigenmode $\vec{\Phi}_m$ of the blade / disc segment through the properties generalised mass, $m_m$, and generalised stiffness, $k_m$, which are the diagonal elements of the corresponding matrices $\mathbf{M}_b$ and $\mathbf{K}_b$, so that

$$\mathbf{M}_b = diag(m_1, m_2,...,m_{DOF}) = \mathbf{\Phi}^*\tilde{\mathbf{M}}_b\mathbf{\Phi} \tag{9}$$

and

$$\mathbf{K}_b = diag(k_1, k_2,...,k_{DOF}) = \mathbf{\Phi}^*\tilde{\mathbf{K}}_b\mathbf{\Phi} \tag{10}$$

The generalised mass and stiffness quantities are also known as modal mass and stiffness. This term is indicative of the fact that the generalised properties are scalar representations of the structural properties that include the specific modeshapes of this structure. For this reason, the generalised masses of a specific structure will be different for different modes, and the same holds true for the generalised stiffnesses.

The decoupled formulation of eq. (8) with its diagonal mass and stiffness matrices implies that the behaviour of each individual eigenmode $m$ can be characterised by a simple scalar equation, namely

$$-\omega_m^2 m_m \, a_{b,m} + k_m \, a_{b,m} = 0 \qquad\qquad (11)$$

In the case of nonzero oscillation amplitudes, the angular frequency of oscillation for this mode is easily found as

$$\omega_m = \sqrt{\frac{k_m}{m_m}} \qquad\qquad (12)$$

Although decoupled, the formulation of eq. (8) is completely equivalent to eq. (4). This also means that it contains the same number of degrees of freedom. However, for practical systems of interest, previous experience has shown that the dynamic behaviour can often be described using a drastically reduced set of eigenmodes without significant loss of accuracy. Furthermore, although the preceding argument was based on an undamped system, the description of the blade dynamics by a reduced set of in-vacuo eigenmodes is also very suitable for lightly damped systems like turbomachinery bladings. Consequently, the reduced set of eigenmodes will be used as generalised coordinates for the following analysis. However, since the focus of the present study is on the interactions of slightly varying blades in a cascade, each blade $b$ will be assigned *individual* modal amplitudes $a_{b,m}$, while the modeshapes $\vec{\Phi}_m$ for each mode $m$ themselves are assumed to be *identical* for all blades.

The preceding analysis is based on the assumption of a linear elastic system in the absence of damping, external and aerodynamic coupling forces. In the case of damped and aerodynamically coupled systems, the amplitudes of the free vibration need not remain constant over time, so that the assumption of eq. (3) must be modified to

$$\tilde{\vec{x}}_b(r,\Theta,z,t) = \vec{x}_b(r,\Theta,z)e^{i\lambda t} = \sum_{m=1}^{n_{modes}} a_{b,m}\vec{\Phi}_m(r,\Theta,z)e^{i\lambda t} \qquad\qquad (13)$$

with

$$\lambda = \omega + i\gamma \tag{14}$$

Here, the complex exponent $\lambda$ consists of a real part $\omega$ that represents the angular frequency of oscillation and an imaginary part $\gamma$ that characterises the evolution of the amplitude with time, representative of the effective damping present in the system under consideration.

In this respect, a positive value of $\gamma$ implies an exponentially decaying oscillation amplitude, hence positive damping, while a negative value of $\gamma$ consequently yields exponentially growing amplitudes, corresponding to negative damping, as in the case of a flutter instability.

### 2.2.2  Reduced order modelling of the complete cascade

Relying on the preceding arguments, eq. (1) can be approximated using a reduced set of eigenmodes as

$$\left[ -\lambda^2 \mathbf{M} + i\lambda \mathbf{D} + (\mathbf{K} + \mathbf{C}) \right] \vec{a} = \vec{F} \tag{15}$$

In this equation, only generalised quantities are used. The vector $\vec{a}$ contains the complex amplitudes for all modes retained for the complete set of blades, hence for an annular cascade consisting of $n_{blades}$ individual blades, each of which retains $n_{modes}$ modeshapes, the number of degrees of freedom in this reduced set of equations is $n_{modes} \cdot n_{blades}$. The matrix $\mathbf{D}$ holds the modal damping values that, just like the generalised masses and stiffnesses, can be assigned to each blade and mode individually.

The vector $\vec{F}$ in eq. (15) contains the generalised external forces on the individual blades and modes that result from the projection of the physical forces $\tilde{\vec{F}}$ on the eigenmodes $\vec{\Phi}$ by

$$\vec{F} = \mathbf{\Phi}^* \tilde{\vec{F}} \tag{16}$$

Similarly, the aerodynamic coupling forces have been transformed into the modal domain, additionally assuming that a linear aerodynamic approach is valid. Then the modal forces due to the aerodynamic interactions $\vec{F}_c$ can be written as the product of the complex aerodynamic influence coefficient matrix $\mathbf{C}$ and the modal amplitudes $\vec{a}$:

$$\vec{F}_c = \mathbf{C}\,\vec{a} = \mathbf{\Phi}^* \tilde{\vec{F}}_c \tag{17}$$

It should be noted that, unlike the real and diagonal mass and damping matrices, the matrix of aerodynamic influence coefficients $\mathbf{C}$ will generally be complex and fully populated, thus accounting for all damping, stiffening and coupling forces between all blades and modes of the cascade that are caused by the aerodynamic interaction.

Using this reduced model, blade-to-blade variations can be readily introduced into the system by changing the generalised properties mass, stiffness or damping assigned to any of the individual blade modes. Additionally, it is possible to add a mechanical coupling stiffness between adjacent blades. It must be stressed, however, that the blade modeshapes are assumed to remain unchanged when varying any of these parameters.

A simplified physical interpretation of this model is shown in Fig. 4. Here, a section of the cascade is shown, comprising of the blade 1 and its neighbours, blade 2 and blade n. Each blade has one degree of freedom in the lateral direction, indicated by its deflection amplitudes $a_1$, $a_2$ and $a_n$, respectively. The modal masses are indicated by the grey squares denoted with the letters m. The stiffness and damping properties are plotted as the spring and damper symbols, denoted by the letters k and d, each with its respective subscripts. These springs and dampers join the masses to the fixed frame of reference, given by the dark grey region below the masses. Additionally, mechanical coupling is included by the springs linking adjacent blade masses, which are labelled $k_c$. In this example, it is assumed that all coupling stiffnesses are identical, hence they carry no additional subscript.
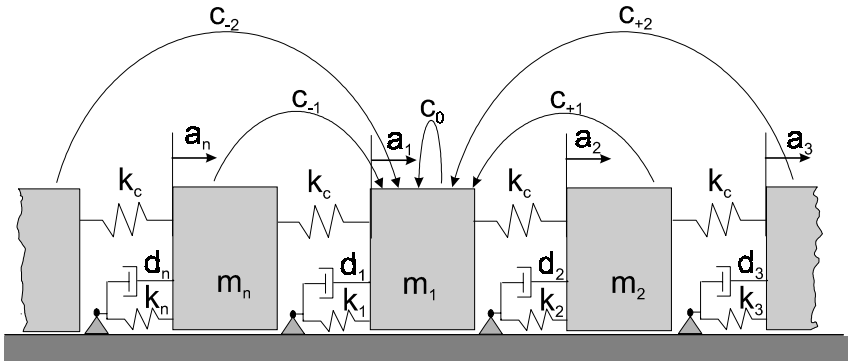


*Fig. 4: Simplified physical interpretation of reduced order cascade model. One degree of freedom per blade shown, aerodynamic forces shown on blade 1 only.*

Finally, the aerodynamic forces among the blades are indicated by the arcs, for clarity these are only shown for the forces acting on blade 1. Of course, analogous aerodynamic forces are acting on all other blades as well, but including all these in the figure would result in an overly cluttered picture. According to the previously used nomenclature, the aerodynamic force representing the eigen-influence of blade 1 on itself is labelled $c_0$, the influence of blade 2 on blade 1 is labelled $c_{+1}$ and so forth.

Since eq. (15) will form the basis of the future analysis, the structure of the constituting matrices will be discussed using a simple example. Consider a cascade of three blades, each of which is assigned two modes as degrees of freedom. In this case, the number of degrees of freedom for the whole problem is six, the amplitudes are arranged in the vector $\vec{a}$ as

$$\vec{a} = \begin{bmatrix} a_{1,1} & a_{2,1} & a_{3,1} & | & a_{1,2} & a_{2,2} & a_{3,2} \end{bmatrix}^T \tag{18}$$

Here, the superscript T indicates the transpose operator. In this notation, $a_{b,m}$ is the complex amplitude of the mode $m$ on blade $b$, so that the first three entries relate to the amplitudes of the three blades for the first mode and the last three entries account for the amplitudes of the three blades for the second mode.

The mass matrix $\mathbf{M}$ is diagonal, containing the following entries

$$\mathbf{M} = \begin{bmatrix} m_{1,1} & & & & & \\ & m_{2,1} & & & & \\ & & m_{3,1} & & & \\ \hline & & & m_{1,2} & & \\ & & & & m_{2,2} & \\ & & & & & m_{3,2} \end{bmatrix} \tag{19}$$

Here, $m_{b,m}$ denotes the generalised mass of blade $b$ for mode $m$.

The stiffness matrices without mechanical coupling will be diagonal as well, with the inclusion of mechanical coupling of the same kind as shown in Fig. 4, it will be block-diagonal. Note that, like in the previous single-mode example, the coupling stiffnesses are assumed to be identical for all blades. They are however different for the two modes, $k_{c,1}$ for mode 1 and $k_{c,2}$ for mode 2.

Thus the stiffness matrix $\mathbf{K}$ reads

$$\mathbf{K} = \left[\begin{array}{ccc|ccc} k_{1,1}+2k_{c,1} & -k_{c,1} & -k_{c,1} & & & \\ -k_{c,1} & k_{2,1}+2k_{c,1} & -k_{c,1} & & & \\ -k_{c,1} & -k_{c,1} & k_{3,1}+2k_{c,1} & & & \\ \hline & & & k_{1,2}+2k_{c,2} & -k_{c,2} & -k_{c,2} \\ & & & k_{c,2} & k_{2,2}+2k_{c,2} & -k_{c,2} \\ & & & -k_{c,2} & -k_{c,2} & k_{3,2}+2k_{c,2} \end{array}\right] \quad (20)$$

Contrary to the mass and stiffness matrices, the aerodynamic coupling matrix $\mathbf{C}$ is fully populated. In this example, it is partitioned into four blocks, $\hat{\mathbf{C}}_{1,1}, \hat{\mathbf{C}}_{2,1}, \hat{\mathbf{C}}_{1,2}$ and $\hat{\mathbf{C}}_{2,2}$, which describe the interaction of the different modes. The complete matrix $\mathbf{C}$ can be written as

$$\mathbf{C} = \left[\begin{array}{c|c} \hat{\mathbf{C}}_{1,1} & \hat{\mathbf{C}}_{2,1} \\ \hline \hat{\mathbf{C}}_{1,2} & \hat{\mathbf{C}}_{2,2} \end{array}\right] = \left[\begin{array}{ccc|ccc} c_{0,1,1} & c_{+1,1,1} & c_{-1,1,1} & c_{0,2,1} & c_{+1,2,1} & c_{-1,2,1} \\ c_{-1,1,1} & c_{0,1,1} & c_{+1,1,1} & c_{-1,2,1} & c_{0,2,1} & c_{+1,2,1} \\ c_{+1,1,1} & c_{-1,1,1} & c_{0,1,1} & c_{+1,2,1} & c_{-1,2,1} & c_{0,2,1} \\ \hline c_{0,1,2} & c_{1,1,2} & c_{-1,1,2} & c_{0,2,2} & c_{+1,2,2} & c_{-1,2,2} \\ c_{-1,1,2} & c_{0,1,2} & c_{1,1,2} & c_{-1,2,2} & c_{0,2,2} & c_{+1,2,2} \\ c_{1,1,2} & c_{-1,1,2} & c_{0,1,2} & c_{+1,2,2} & c_{-1,2,2} & c_{0,2,2} \end{array}\right] \quad (21)$$

The blocks on the main diagonal, $\hat{\mathbf{C}}_{1,1}$ and $\hat{\mathbf{C}}_{2,2}$ denote the aerodynamic forces induced by the airfoil oscillation in modes 1 and 2 on the generalised forces in the direction of the same mode, while the blocks $\hat{\mathbf{C}}_{2,1}$ and $\hat{\mathbf{C}}_{1,2}$ are representative of the generalised forces generated by oscillation in mode 2 in the direction of mode 1 and vice versa. In the blocks themselves, the individual elements denote the interaction between the blades of the cascade. Here, the entries on the main diagonal refer to the eigen-influence of the blades, i.e. the generalised forces induced by an oscillating blade on the blade itself. As long as all blades are assumed to be aerodynamically identical, these coefficients are the same for all blades. The off-diagonal elements of the blocks in turn represent the influence of an oscillating blade on the other blades. Again, in case of all blades being aerodynamically identical, these coefficients are only dependent on the distance between the blades, so that this distance is also used for the first index of the coefficients. As an example, the coefficient $c_{2,j,k}$ characterises the influence of blade number 3 vibrating in mode $j$ on the generalised force on blade 1 in the direction of mode $k$. Similarly, it represents the influence of blade 4 on blade 2, blade 5 on blade 3 and so

forth. In the present study, the condition of aerodynamically identical blades was always assumed, although the theoretical framework of this analysis does not require this prerequisite. In case of this assumption, only $n_{blade} \cdot \left( n_{mode} \right)^2$ independent coefficients are needed to fill the matrix $\mathbf{C}$, although it contains $\left( n_{blade} \cdot n_{mode} \right)^2$ entries. The individual influence coefficients faithfully represent the aerodynamic behaviour for arbitrary modeshapes, as long as the underlying unsteady aerodynamic solver used to derive them is capable of adequately resolving them. In the current analysis, a three-dimensional linearised Euler solver developed by the author is used, which is able to calculate the unsteady aerodynamics for arbitrary modeshapes. The computational accuracy of the solver has been validated for sub- and transonic flow configurations of compressor and turbine cascades. For further details the reader is referred to the appendices, where the theory and implementation of the solver is found in Appendix B and the computational procedures and resource requirements are outlined in Appendix D.

### 2.2.3  Energy method

A significant simplification of the problem can be achieved if a cascade of identical blades is considered. For this case it has been shown that the cascade eigenvectors are travelling wave modes, in which all blades oscillate at the same frequency and in the same motion, with a constant phase difference between the motions of neighbouring blades. This phase difference is known as the interblade phase angle, $\sigma$.

A further simplification arises if the blade's mass parameter is very high. The mass parameter, defined as blade mass per unit span divided by gas density and by blade chord squared, is a measure of the ratio between the blade mass and the mass of a representative fluid volume that is influenced by the oscillating blade. If this mass parameter is very high, as in the case of solid metal turbomachinery blades, then it can be assumed that the changes in the eigenmodes and eigenfrequencies of the tuned cascade due to the aerodynamic forces are negligible.

Under these assumptions, Carta [11] has shown that the aerodynamic damping (logarithmic decrement) $\delta_{aero}$ of the cascade can be calculated separately for each travelling wave mode of the cascade.

The aerodynamic damping $\delta_{aero}$ is then only dependent on the unsteady aerodynamic work per period, $W_{aero}$ of the flow performed on the vibrating blade and on the mean kinetic energy $KE_{mean}$ of the vibrating blade itself, so that

$$\delta_{aero} = -\frac{W_{aero}}{4KE_{mean}} \tag{22}$$

Here, the mean kinetic energy can be calculated from the generalised mass $m$ and the oscillation angular frequency $\omega$ by

$$KE_{mean} = \frac{1}{4}m\omega^2 \tag{23}$$

In case of additional mechanical damping being present, this can be included simply by addition to the aerodynamic damping, so that

$$\delta_{total} = \delta_{aero} + \delta_{mech} \tag{24}$$

Using eq. (24), it can be stated that flutter instability will occur if $\delta_{total} < 0$, indicating a situation where the amplitude and hence the oscillatory energy of each blade increases continuously - in practice until the blade breaks or other nonlinear effects become dominant.

Due to the fundamental idea of this method, which is to use the energy balance on the blade to derive the damping, it is also well known as the *energy method*. The values of damping derived from the energy method will be used as reference data in the following chapters.

## 2.2.4 Eigenvalue analysis

We will now return to the general case of a mistuned cascade without the assumption of a high mass parameter. In the absence of external forces, the prime interest is on the eigenmodes and eigenvalues of the cascade, describing the flutter stability and the free vibration behaviour of the cascade. For this purpose, eq. (15) can be reformulated as

$$\left[ \mathbf{M}^{-1}(\mathbf{K}+\mathbf{C}) + i\mathbf{M}^{-1}\mathbf{D}\lambda - \mathbf{E}\lambda^2 \right]\vec{a} = \vec{0} \tag{25}$$

Being a non-linear eigenvalue problem, this is fairly inconvenient to solve numerically. Two possibilities exist to revert to a linear eigenvalue problem from here. The first of these requires the assumption that the ratio of modal damping $d$ to modal mass $m$ is the same for all of blades and all modes.

In this case, a transformation of the eigenvalues $\lambda \to \zeta$ is helpful with

$$\zeta = (\lambda - i\frac{d}{2m})^2 \tag{26}$$

The transformed eq. (25) then reads

$$\left[ \mathbf{M}^{-1}(\mathbf{K} + \mathbf{C}) - \mathbf{E}\frac{d^2}{4m^2} - \mathbf{E}\zeta \right] \vec{a} = \vec{0} \tag{27}$$

This constitutes a linear eigenvalue problem for $\zeta$ and can be readily solved using standard numerical analysis methods. However, the underlying assumption of constant modal damping prohibits the assessment of the effects of damping mistuning on the aeroelastic eigenvalues and eigenvectors of the cascade. Therefore, a different approach is proposed below, relying on the assumption that the aeroelastic eigenvalues do not differ much from the in-vacuo eigenvalues of the individual blades. In this approach, the eigenvalue $\lambda$ as a factor of the damping matrix in eq. (25), is replaced by the in-vaco eigenvalue $\lambda_0$ for the corresponding blade and modeshape. The value of $\lambda_0$ is analytically known in advance from the generalised mass, stiffness and damping values $m$, $d$ and $k$ for this degree of freedom as

$$\lambda_0 = \sqrt{\frac{k}{m} + \frac{d^2}{4m^2}} + i\frac{d}{2m} \tag{28}$$

Consequently, eq. (25) is approximated by

$$\left[ \mathbf{M}^{-1}(\mathbf{K} + \mathbf{C}) + i\mathbf{M}^{-1}\mathbf{D}\lambda_0 - \mathbf{E}\lambda^2 \right] \vec{a} = 0 \tag{29}$$

In this approach, no assumption concerning the distribution of damping in the cascade is made, so that the effect of damping mistuning can be studied. On the other hand, the approach can only be expected to yield valid results as long as the computed eigenvalues are similar to the in-vacuo eigenvalues of the individual blades. In the following argument, it will be shown that, for practical purposes, this condition is usually well met.

The approximation of eq. (25) by eq. (29) effectively introduces an extra term $i\mathbf{M}^{-1}\mathbf{D}(\lambda_0 - \lambda)$, so that eq. (29) can also be written as

$$\left[ \mathbf{M}^{-1}(\mathbf{K} + \mathbf{C}) + i\mathbf{M}^{-1}\mathbf{D}\lambda + i\mathbf{M}^{-1}\mathbf{D}(\lambda_0 - \lambda) - \mathbf{E}\lambda^2 \right] \vec{a} = \vec{0} \tag{30}$$

Obviously, if the value of $\lambda_0$ is exactly equal to the true value $\lambda$, no error at all is made. Let now the in-vacuo frequency $\omega_0 = \mathrm{Re}(\lambda_0)$ differ slightly from the aeroelastic eigenfrequency $\omega$ and the in-vacuo decay rate $\gamma_0 = \mathrm{Im}(\lambda_0)$ differ slightly from the aeroelastic decay rate $\gamma$. Then we can write

$$\left[ \mathbf{M}^{-1}\left[ (\mathbf{K} + \mathbf{C} - \mathbf{D}(\gamma_0 - \gamma) \right] + i\mathbf{M}^{-1}\mathbf{D}(\lambda + (\omega_0 - \omega)) - \mathbf{E}\lambda^2 \right]\vec{a} = 0 \qquad (31)$$

From this, it can be seen that the effect of a slight deviation of $\omega_0$ from $\omega$ will lead to a change in the imaginary (damping) terms of the system, while a deviation of $\gamma_0$ from $\gamma$ will change the real (stiffness) terms of the system. Considering the fact that the deviation of the aeroelastic eigenfrequencies from the mechanical in-vacuo eigenfrequencies is usually well below 1% for turbomachinery applications, the error associated with using $\omega_0$ will lead to no more than an associated variation of below 1% in the mechanical damping associated with the individual blade modes. The difference $(\gamma_0 - \gamma)$ is pre-multiplied by the damping matrix $\mathbf{D}$ whose terms are some orders of magnitude smaller than the stiffness terms of matrix $\mathbf{K}$ to which they are added. Consequently, this effect is almost completely negligible.

## 2.3   Dependence of aerodynamic coefficients on frequency

In the preceding sections, it was assumed that the aerodynamic coefficients contained in the matrix $\mathbf{C}$ were independent of the frequency of oscillation $\omega$ for the small variations of $\omega$ considered in this context. However, for some cases of large mistuning it might be of interest to study the effect of the variability of the aerodynamic coefficients with $\omega$. For the eigenvalue analysis, this variability of $\mathbf{C}$ poses a problem, since the oscillation frequency $\omega$ of the aerodynamic eigenmodes is not known a priori but rather is a result of the calculation. In the cases considered here, it is known that the deviation of the aeroelastic eigenfrequencies from the in-vacuo blade eigenfrequencies is small. Consequently, it is sensible to deduce the variable values of $\mathbf{C}$ from some pre-calculated values using values of $\omega$ in the vicinity of the in-vacuo frequencies $\omega_0$.
This can be achieved by assuming a quadratic dependency of the individual elements of $\mathbf{C}$ on $\omega$, that is, by setting

$$\mathbf{C} = \mathbf{C}_0 + \mathbf{C}_2\omega^2 \qquad (32)$$

The coefficient matrices can easily be computed using, for example, three frequencies at and around the vacuum eigenfrequencies of the respective blade modes, $\omega_0$. Using this approach, eq. (29) can be modified to read

$$\left[ \mathbf{M}^{-1}(\mathbf{K} + \mathbf{C}_0 + \mathbf{C}_2\omega^2) + i\mathbf{M}^{-1}\mathbf{D}\lambda_0 - \mathbf{E}\lambda^2 \right]\vec{a} = 0 \tag{33}$$

Remembering that $\lambda = \omega + i\gamma$ and that we are dealing with lightly damped systems, hence $\omega \gg \gamma$, we can approximate:

$$\mathbf{C}_2\omega^2 \approx \mathbf{C}_2\lambda^2 \tag{34}$$

Using this approximation, eq. (33) then reads:

$$\left[ \mathbf{M}^{-1}(\mathbf{K} + \mathbf{C}_0) + i\mathbf{M}^{-1}\mathbf{D}\lambda_0 - \mathbf{E}\lambda^2 \right]\vec{a} \approx \mathbf{M}^{-1}\mathbf{C}_2\lambda^2\vec{a} \tag{35}$$

Hence, we now have a general linear eigenvalue problem for $\lambda^2$. Note that we could also retain the standard eigenvalue formulation by pre-multiplying eq. (35) with $(\mathbf{E} - \mathbf{M}^{-1}\mathbf{C}_2)^{-1}$, as long as the bracketed term is non-singular, but solving the form shown in eq. (35) can be done more efficiently using standard numerical procedures, for example using the Open Source LAPACK routines.

## 2.4 Forced response analysis

If external forces are present, then the forced response of the oscillation system is of interest, namely the amplitudes and phases of all the blades after the transients have decayed. For this reason, it is sufficient to set $\lambda = \omega$ in eq. (15), because $\omega$ is now known in advance to be the frequency of the excitation force $\vec{F}$ and hence is also the oscillation frequency in which the coupled aeroelastic system responds. The resulting linear system of equations

$$\left[ -\omega^2\mathbf{M} + i\omega\mathbf{D} + (\mathbf{K} + \mathbf{C}) \right]\vec{a} = \vec{F} \tag{36}$$

can then be directly solved. In doing so, the appropriate dynamic properties of the individual blades and modes are inserted in the corresponding matrices for any prescribed value of the excitation frequency $\omega$.

For the case of calculating the blade response under external forces, the variability of the aerodynamic coefficients with the excitation frequency does not pose a serious problem, since for each case the excitation frequency and consequently also the oscillation frequency of all blades in the cascade is known in advance and is prescribed, so that, if it is required for accuracy, the exact aerodynamic coefficients can be

calculated for this frequency. In most cases however, an interpolation procedure using a range of pre-calculated sets of aerodynamic coefficients for different values of $\omega$ will be sufficient to yield very accurate results.

## 2.5   Summary of chapter 2

This chapter described the theoretical background of the current method. Starting from the results of standard FEM structural analysis tools, the aeroelastic system of the cascade is set up using a restricted set of structural modeshapes for each blade. These blade specific modeshapes are calculated for in-vacuo conditions, i.e. in the absence of aerodynamic forces. A restricted set of these modeshapes is then used as generalised co-ordinates for the description of the aeroelastic behaviour of each of the blades in the aerodynamically coupled complete cascade. The resultant matrix equations contain the generalised structural parameters from the FEM analysis and the generalised aerodynamic coupling coefficients that are derived from tuned, travelling wave unsteady 3D aerodynamic calculations. The use of a simple spring model enables the incorporation of structural coupling between the modes of neighbouring blades.

Dependent on the nature of the problem under consideration, an eigenvector / eigenvalue problem has to be solved for the flutter problem or a complex linear set of equations has to be solved for the forced response problem.

Using this model for the aeroelastic system, mistuning can be easily incorporated in any of the modal parameters mass, stiffness or damping. For the case of damping mistuning, the resulting nonlinear eigenvalue problem is reduced to a linear problem by an approximation that is valid for all cases where the difference between the eigenvalues of the tuned and the mistuned system can be assumed to be small.

Finally, a method is presented to compensate for the frequency dependence of the aerodynamic influence coefficients in the flutter and in the forced response calculations.

With respect to previously published work by other authors, the following aspects are new to the present approach

- The complete model is formulated in blade specific modal coordinates, resulting in a very compact set of matrix equations. This compares to other approaches using complete FEM models with tens of thousands of degrees of freedom.
- The use of aerodynamic influence coefficients facilitates the analysis of arbitrary blade modeshapes and allows the inclusion of the coupling effect between different modeshapes. The few previous works that included aerodynamic

coupling effects at all were either fully coupled non-linear methods with prohibitively high demands for computing resources [9], [12], were neglecting the coupling between different modes [54], or they relied on simple 2D bending and torsional modeshapes [38], [39].

- Since the generalised mass, stiffness and damping quantities are clearly attributed to specific blades and their modeshapes, any kind of mistuning can be easily incorporated into the model. Although not used in the present study, the model can also handle cascades where the individual blades are aerodynamically not identical (aerodynamic mistuning).

- The dependence of aerodynamic coefficients on the frequency is properly included in the eigenvalue analysis, so that no iterative process is required in the derivation of the true aeroelastic eigenfrequencies.

- The computational method derived from this analytical model is sufficiently fast, so that it lends itself to parametric studies. Similarly, it is suitable to be included in Monte-Carlo methods for the statistical analysis of randomly mistuned cascades.

### 3    Case study 1: Single stage compressor rig

In the following two chapters, the previously developed methods will be applied to existing turbomachinery cases. The first test case studied here is the rotor of a transonic compressor rig [7].

### 3.1   Design parameters and steady flow conditions

The geometry of this first test case is representative of a modern HP compressor front stage. The main design parameters of the rig are given in Table 1.

| Number of stages | 1 |
|---|---|
| Number of rotor blades | 16 |
| Number stator vanes | 29 |
| Number of outlet struts | 5 |
| Tip diameter | 0.38 m |
| Inlet hub to tip ratio | 0.51 |
| Shaft speed | 20.000 rpm |
| Mass flow | 16 kg/s |
| Pressure ratio $p_{2s}$ / $p_{t1}$ | 1.5 |
| Tip speed | 398 m/s |

*Table 1: Design parameters of the transonic compressor rig*

The blades of the rotor under consideration are manufactured of carbon fibre reinforced plastics (CFRP), giving it a relatively low mass parameter compared to standard design titanium blades. Fig. 5 shows a virtual cutaway view of a section of the compressor blading, picturing the three blade rows of rotor, stator and the struts, which are needed to support the hub and the rotor bearing. The compressor rotor hardware is shown in Fig. 6, before it is mounted into the complete rig. The CFRP blades are assembled into the disc, along with the inlet cone. The stand visible below the rotor is used for assembly purposes only.
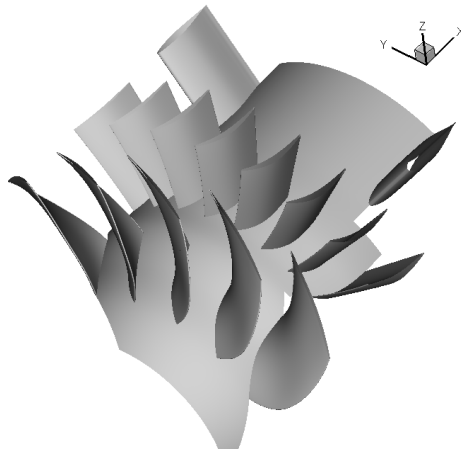
*Fig. 5: Cutaway view at the transonic compressor rig, front looking aft, rotor, stator and struts.*
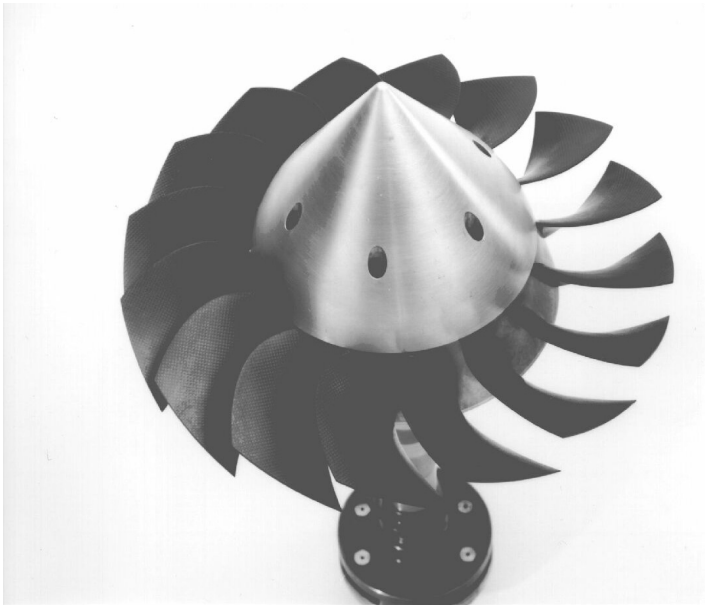


*Fig. 6: Transonic compressor rotor hardware*

Fig. 7 depicts the iso-Mach contours on a plane at approximately 85% blade height. The Mach numbers are given in the respective relative frame of reference, hence the isolines are discontinuous at the rotor / stator interface. The stage has no inlet guide vane, so that the inflow to the rotor is axial. The tip relative inlet Mach number is approximately 1.4.
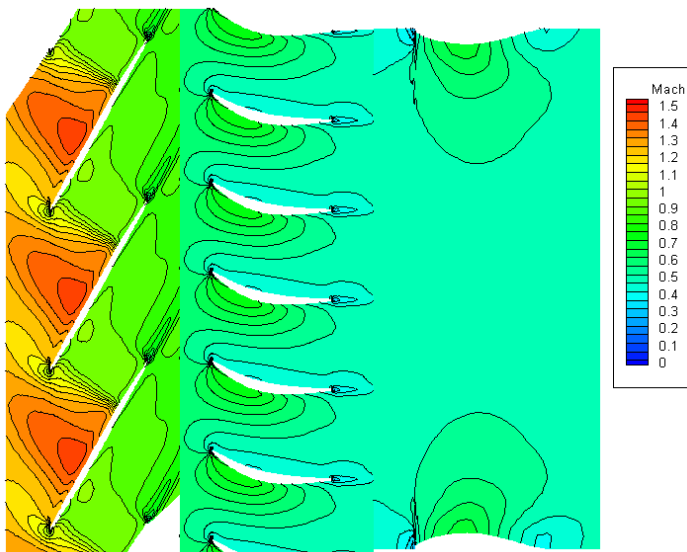


*Fig. 7: Transonic compressor rotor, iso-Mach contours at 85% blade height*

## 3.2  Eigenvalue analysis

### 3.2.1  Tuned cascade results

Fig. 8 shows the Campbell diagram of this rotor, giving the frequencies of the lowest 4 eigenmodes, namely the 1st bending (1F), 1st torsional (1T), 2nd bending (2F) and 2nd torsional (2T) mode. These were calculated using a commercial FEM analysis tool under the assumption of in-vacuo conditions, i.e. in the absence of aerodynamic forces. As a consequence of the twisted and tapered blade shape, these modeshapes are not purely bending and purely torsional, but the bending modeshape contains a small torsional component and vice versa.

In Fig. 8, the dependence of the blade natural frequencies on the rotational speed is visible, the increase in eigenfrequencies with rotor speed being due to the stiffening effect of the centrifugal forces. In the following sections, we will concentrate on the lowest two eigenmodes. At the design speed of 20,000 rpm, the FEM analysis yields the frequency of the 1F eigenmode at 762 Hz and that of the 1T eigenmode at 1505 Hz.
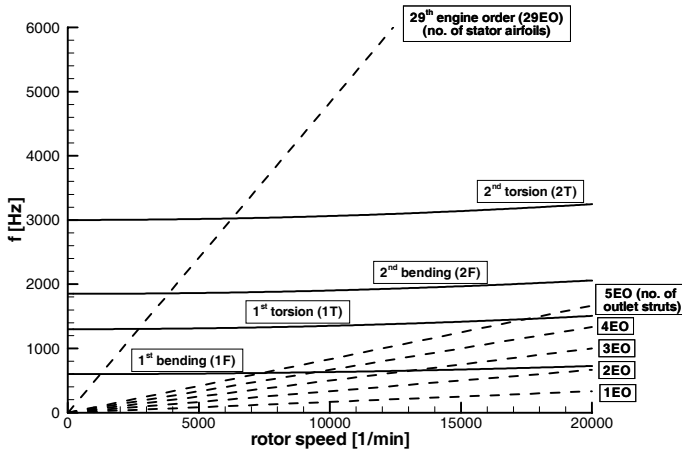


*Fig. 8: Campbell diagram of the transonic compressor rotor, lowest 4 eigenmodes shown.*

For this cascade, the unsteady aerodynamic coefficients are calculated for the two eigenmodes under consideration. Following the methodology described in Appendix B, these coefficients were computed for all travelling wave modes, immediately yielding the aerodynamic damping under the energy method assumptions. For the eigenvalue methodology, the travelling wave mode coefficients are transformed to influence coefficients, conforming to Appendix B (section B.5). Fig. 9 shows the magnitudes of the influence coefficients for this configuration. The upper figure shows the intra-mode coefficients, i.e. the generalised force exerted by a blade oscillating in a particular mode on itself or another blade oscillating in the same mode, while the lower figure shows the inter-mode, or cross-coupling coefficients, i.e. the generalised force exerted by a blade oscillating in a particular mode on another blade oscillating in a different mode. The x-axis denotes the index of the oscillating blade relative to the blade that the force acts on.
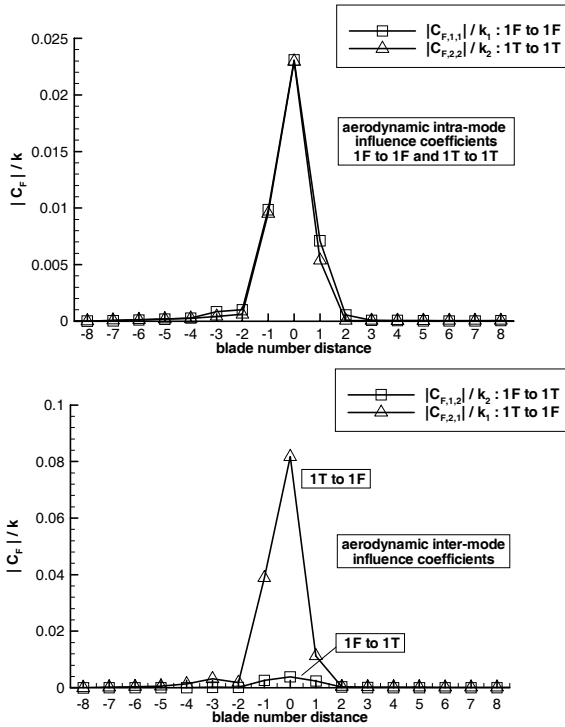
*Fig. 9: Normalised generalised force influence coefficients for transonic compressor rotor, 1F and*
*1T eigenmodes – top: Intra-mode coefficients, bottom: inter-mode coefficients*

For example, the points at x=-1 indicate the influence coefficients describing the magnitude of the forces due to the oscillation of the blade –1 (the direct neighbour to the pressure side of blade 0) acting on blade 0, which, due to the symmetry of the cascade, are equal to the forces due to the oscillation of any blade n-1 acting on its immediate suction side neighbour, blade n.

The values of the generalised force coefficients are of the dimension of generalised force per generalised deflection, which is identical to the dimension of the generalised stiffness. Since the effect of these forces depends on their magnitude in proportion to the generalised stiffness of the mode they are acting on, this value of general stiffness has been used to normalise the respective generalised force influence coefficients. For example, the coefficients $C_{F,1,2}$, describing the force on the torsional mode (no. 2) due to a bending mode (no. 1) oscillation, is normalised by the generalised stiffness of the

torsional mode (no. 2). In the simplified case of a pure bending and a pure torsional mode of a 2D airfoil section, $C_{F,1,2}$ would relate to the moment due to bending. Similarly, $C_{F,1,1}$ would describe lift due to bending, $C_{F,2,1}$ would be lift due to torsion and $C_{F,2,2}$ would be the moment due to torsion.

The actual magnitudes of the influence coefficients show a very similar behaviour for the intra-mode coefficients $C_{F,1,1}$ and $C_{F,2,2}$. In both cases, the influence of the oscillating blade on itself (at x=0) is by far the largest, and for both modes, the normalised value is almost identical. Furthermore, the –1 values are significantly higher than the +1 values, manifesting that the influence of the oscillating suction side on the neighbouring pressure side is much higher than vice versa. Finally, the coefficients for –2 and lower as well as for +2 and higher are of almost negligible magnitude. Looking at the inter-mode influence coefficients, the dominance of the eigen-influence and the influence of the two neighbouring blades is similar to the intra-mode coefficients. However, when comparing the coefficients for the two modes, the values of the cross-coupling coefficients differ significantly in magnitude. For the eigen-influence of the oscillating blade on itself (distance=0), the coefficient indicating the influence of the torsional mode on the bending mode is approximately 8 times as large as the corresponding coefficient describing the generalised forced in the direction of the torsional mode generated by the bending. The physical explanation for this phenomenon is straightforward: The torsional motion of an airfoil section changes the angle of attack of the oscillating profile, which is well known to cause a major change in the lift generated - the lift being nothing else than a force in the bending direction. On the other hand, the bending motion of an airfoil section will only cause a minor change in the torsional moment on the airfoil, hence the small values for this coefficient.

Given these coefficients, the resulting aerodynamic damping for both the energy method as well as for the eigenvalue method can now be readily calculated.

Fig. 10 shows the total damping, resulting from aerodynamic and mechanical damping, as a function of the interblade phase angle $\sigma$ for both eigenmodes. The large, open symbols connected by the dashed lines are the results obtained using the energy method, while the small, filled symbols connected by solid lines are the results from the eigenvalue method. In this and all further calculations of the transonic compressor, a value of $\delta_{mech} = 0.01$ is assumed for the mechanical damping of all modes, unless a different value is stated explicitly.
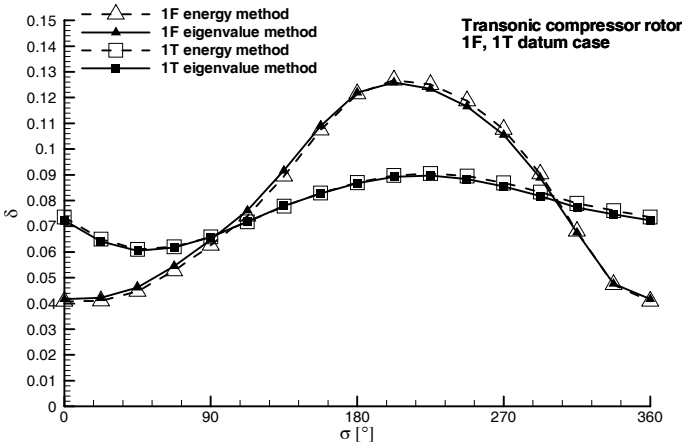
*Fig. 10: Transonic compressor rotor damping $\delta$ over interblade phase angle $\sigma$ for 1F and 1T eigenmodes*

The first observation which is most important from the designer's perspective is that the cascade is aeroelastically stable. The total damping is positive for all interblade phase angles $\sigma$, hence no flutter will occur at this operating point. Secondly, the figure shows that the computed differences in damping between the simple energy method and the more elaborate eigenvalue method are minimal for this cascade, even though the mass parameter is fairly low for a turbomachinery cascade due to the use of carbon-fibre reinforced plastics (CFRP). This supports the conclusion that, for a typical tuned turbomachinery cascade where the mass parameter is even higher, the energy method simplification is well justified.

Fig. 11 shows the influence of the aerodynamic forces on the eigenfrequencies of the cascade, using the same lines and symbols for the different cases as in Fig. 10. Plotted is the frequency ratio $\eta = f / f_0$ as a function of the interblade phase angle $\sigma$, where $f_0$ is the respective in-vacuo eigenfrequency of the corresponding mode. As the basic idea of the energy method (see section 2.2.3) implies that the frequencies remain unchanged by the aerodynamic forces, the value of the frequency ratio is always exactly equal to one in these cases.
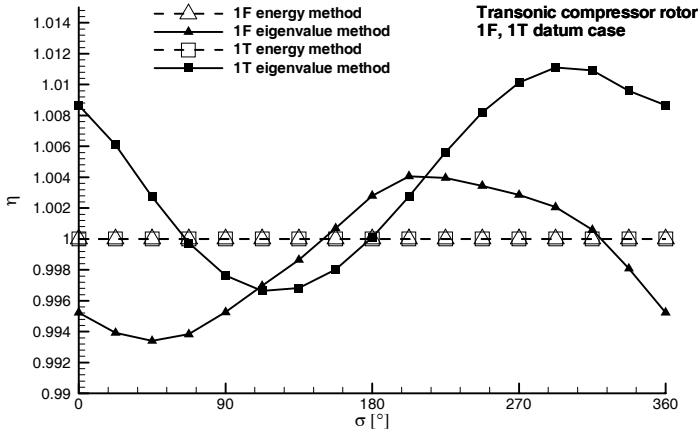
**Fig. 11: Transonic compressor rotor frequency ratio for 1F and 1T eigenmodes**

The eigenvalue method, on the other hand, includes the effect of the aerodynamic forces on the eigenfrequencies. It can be seen that the aerodynamic forces, dependent on the interblade phase angle $\sigma$, can act either stiffening the system - thus bringing up the eigenfrequency ratio to values above one - or can also act softening the system, hence reducing the eigenfrequency ratio. The maximum change in eigenfrequencies, however, is fairly small, the maximum deviation from the in-vacuo eigenfrequency reaching +1.1% at $\sigma =292.5°$ for the 1T eigenmode.

In this situation of a perfectly tuned configuration, where each blade is strictly identical to all the others, the eigenvectors belonging to the eigenvalues shown above necessarily have identical amplitudes for all blades. For reasons of symmetry, no single blade is in any way distinguished from the rest, and this reflects in the structure of the eigenvectors. In each eigenvector, there is a constant phase angle difference between the motions of any two neighbouring blades, resulting in the familiar travelling wave modes with constant interblade phase angle, that form the basis for the energy method calculation.

Combining the previous figures (Fig. 10 and Fig. 11) yields a picture showing the locus of the eigenvalues as damping over eigenfrequency, with the interblade phase angle $\sigma$ as a parameter. Fig. 12 a and b show the corresponding plot for the 1F and 1T eigenmode, respectively. The interblade phase angle $\sigma$ is indicated by the labels at the respective data points. This type of diagram will be used throughout the following section since it is well suited to show the effects of mistuning and coupling on the aeroelastic

eigenvalues. For this purpose, we will first concentrate on the 1T eigenmode of this cascade.
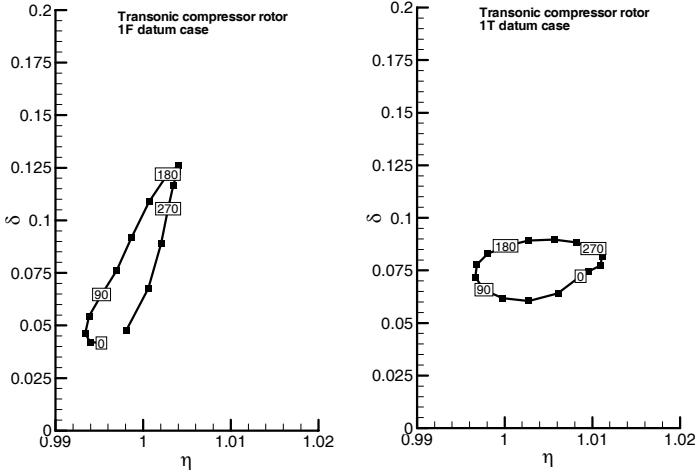


**Fig. 12 Eigenvalues of the tuned transonic compressor rotor, shown as damping δ over frequency ratio η.  Left : (a) 1F eigenmode; Right: (b) 1T eigenmode**

### 3.2.2  Single blade frequency mistuning

The first, most simple case of mistuning consists of a cascade where a single blade's stiffness is mistuned from the rest of the cascade, all the remaining blades featuring identical structural properties. The amount of mistuning will be defined by the mistuning parameter $\varepsilon$ :

$$\varepsilon = \frac{\omega_{vac,blade}}{\omega_{vac,blade,tuned}} - 1 \tag{37}$$

Using this definition, $\varepsilon = 0$ corresponds to the tuned case, positive values of $\varepsilon$ indicate an in-vacuo eigenfrequency higher than the tuned value and negative values indicate a lower eigenfrequency. In Fig. 13, the gradient symbols show the locations of the eigenvalues for a situation, where the torsional eigenfrequency of blade no. 8 is 2% lower than the rest of the blades, hence $\varepsilon$ = -0.02. The circles denote the tuned configuration ($\varepsilon$ =0) of Fig. 12b for reference. For the eigenvalues of the mistuned configuration, five of them are labelled to identify them for further discussion. The numbering is according to increasing values of $\eta$. In the mistuned case, the eigenvalue

no. 1 is distinctly segregated from the rest of the eigenvalue cluster, having a lower eigenfrequency and a damping value of approximately the average of the rest of the eigenvalues. The remaining eigenvalues converge into a smaller cluster, centred around the mean of the tuned configuration cluster. This implies that the damping of the least stable eigenvalue (no. 7) increases with increasing mistuning, resulting in an increase of aeroelastic stability of the cascade. One eigenvalue (no. 12) at higher values of $\eta$ seems to show a different behaviour from the remaining ones. While all other eigenvalues except from no. 1 seem to be aligned on an ovoid similar in shape to that of the tuned configuration, the eigenvalue no. 12 stands apart significantly.
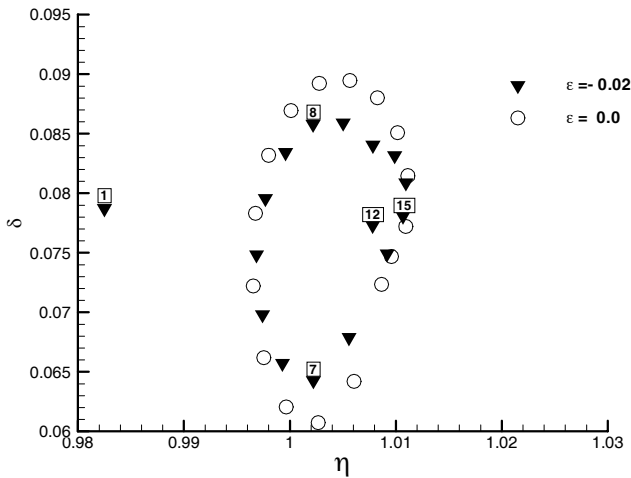


*Fig. 13: Eigenvalues for transonic compressor rotor 1T eigenmode with one blade (no.8) mistuned*
*($\nabla$: mistuned case $\varepsilon$ = -0.02;  o: datum case $\varepsilon$ = 0)*

Each of the eigenvalues shown in Fig. 13 is associated to a specific cascade eigenvector, which describes the amplitude and phase distribution of all blades in the cascade. While in the tuned case all blades have equal amplitudes with a constant interblade phase angle, this is no longer true for the mistuned case. In the mistuned case, the perfect symmetry of the tuned case is no longer existent, and this is reflected in the structure of the eigenvectors. A closer inspection of the eigenvectors shows that the mistuned blade is strongly decoupled from the rest of the cascade in this case of single blade mistuning. This can be seen in the eigenvector amplitude distribution, shown in Fig. 14. This graph shows the individual participation of the blades for some of

the 16 eigenvectors. Due to the nature of the eigenvalue problem, the norm of the eigenvectors is arbitrary, in this case it was adjusted to yield an Euclidian norm of 1 for each eigenvector.
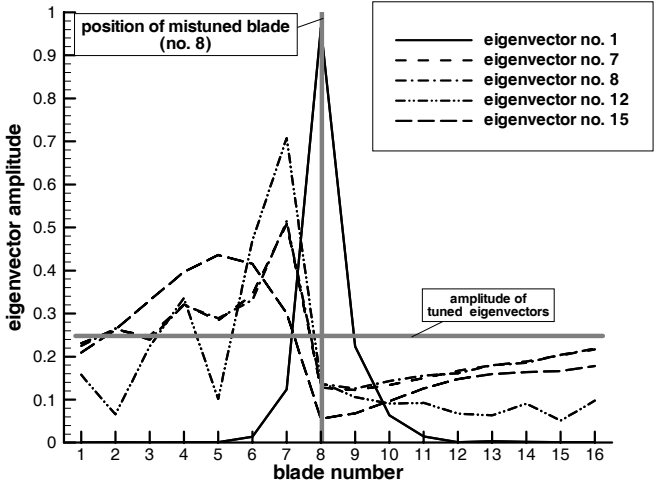


*Fig. 14: Selected eigenvector amplitudes for transonic compressor rotor 1T eigenmode with blade no.8 mistuned, ε = -0.02.*

The eigenvector corresponding to the segregated eigenvalue is represented by the solid line. The other four eigenvectors shown are typical for the rest of the complete set, hence the figure was restricted to these eigenvectors for clarity. The numbering of the eigenvectors is according to ascending frequencies of the corresponding eigenvalues, hence the eigenvector 1 corresponds to the lowest frequency, which is the segregated eigenvalue. The position of the mistuned blade no. 8 is indicated by the vertical grey bar, the horizontal grey bar indicates the amplitude of the tuned eigenvectors, which is identical for all blades and for all eigenvectors.

It can be seen that eigenvector no. 1 is dominated by the mistuned blade itself, with some participation from its immediate neighbours. The other blades show hardly any participation for this eigenvector. On the other hand, the participation of the mistuned blade for the remaining eigenvectors is fairly small. However, blade no. 9, which is adjacent to the suction side of the mistuned blade, also has a very low participation for these eigenvectors. This points to the fact that the aerodynamic influence on the blade located next to the suction side is fairly high, as already shown in the previous section. While the eigenvectors 7, 8 and 15 do not differ much from the tuned eigenvector

values, apart from in the vicinity of the mistuned blade, eigenvector 12 shows larger deviations over the whole set of blades.

In Fig. 15, the interblade phase difference distributions are plotted for the same eigenvectors as in Fig. 14.
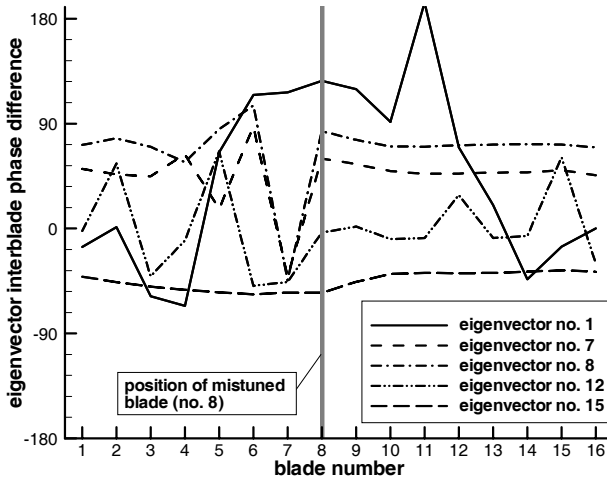


*Fig. 15: Selected eigenvector interblade phase difference distributions for transonic compressor rotor 1T eigenmode with blade no.8 mistuned, ε = -0.02.*

Recall that for the tuned configuration, each eigenvector corresponds to a specific interblade phase difference, which is constant for all blades in this eigenvector. For the mistuned configuration, this is no longer the case. Fig. 15 shows that for the eigenvectors 7, 8 and 15, the interblade phase differences smooth out and settle to an almost constant value away from the mistuned blade 8. For the eigenvectors 1 and 12, that exhibited significantly different characteristics from the tuned values already in the eigenvalues and in the eigenvector amplitudes, the interblade phase differences show large variations over the whole set of blades.

Obviously, the detailed analysis of the eigenvector characteristics is very laborious, even for this simplest example of a mistuned cascade, where only a single blade mode is considered and only one blade is mistuned. To achieve a more condensed representation of the large amount of data available from the computation, a scalar parameter that describes the localisation characteristics of a complete eigenvector is

defined. This value, termed "localisation parameter $\psi$" will be used in the following sections. It is calculated using the ratio of the maximum magnitude $a_{max}$ of a single element in the eigenvector to the mean value $a_{mean}$ of all the elements. This is done in such a way that a "tuned" eigenvector, where all elements are of the same magnitude, yields a localisation parameter of $\psi = 0$, while a fully localised eigenvector, where all elements except one are zero, yields a value of $\psi = 1$. This is achieved by the following formulation:

$$\psi = \frac{1}{2\left(n_{blade}-1\right)} \sum_{k=1}^{n_{blade}} \left| \frac{a_k}{a_{mean}} - 1 \right| \tag{38}$$

where

$$a_{mean} = \frac{1}{n_{blade}} \sum_{k=1}^{n_{blade}} a_k \tag{39}$$

Using this definition, the localisation parameter $\psi$ has been evaluated for the case of $\varepsilon = -0.02$, shown in Fig. 14. The result is given in Fig. 16..



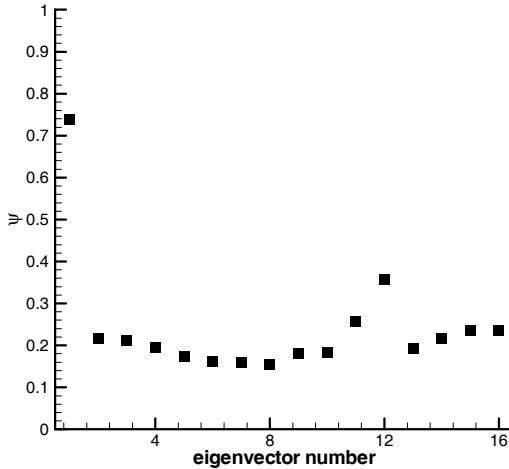*Fig. 16: Eigenvector localisation parameter $\Psi$ for transonic compressor rotor 1T eigenmode with blade no.8 mistuned, $\varepsilon = -0.02$*

The previously described characteristics of the individual eigenvector are faithfully reproduced by the selected parameter, showing a strong localisation for eigenvector 1, a moderate localisation for eigenvector 12 and low values, indicating largely distributed

eigenvectors, for the remaining ones, including the eigenvectors 7, 8 and 15 discussed above.

The finding that the strong single blade mistuning decouples the mistuned blade from the rest of the cascade also explains the damping value of the segregated eigenvalue no. 1, since the mean value of the tuned configuration corresponds to the self-induced damping of the blade, without any influence of the neighbouring blades. Similarly, the remaining eigenvalues of the mistuned configuration tend to converge towards the mean damping, while their frequency ratio values are changed only very slightly.

In Fig. 17, the eigenvalues of the transonic compressor rotor are shown for a whole range of mistuning strengths, ranging from $\varepsilon = $ -0.02 to $\varepsilon = $ +0.02. The gradient, circle and delta symbols represent the cases of maximum negative mistuning, no mistuning and maximum positive mistuning, respectively. Additionally, the trajectories of the eigenvalues for all values of the mistuning parameter in between these extrema are indicated by the lines. The results for $\varepsilon = $ +0.02 are seen to be very similar to those for $\varepsilon = $ -0.02, apart from the fact that the segregated eigenvalue now lies to the right of the remaining eigenvalue cluster. Again, the remaining eigenvalues tend towards a mean damping value, while their frequency shift is small.
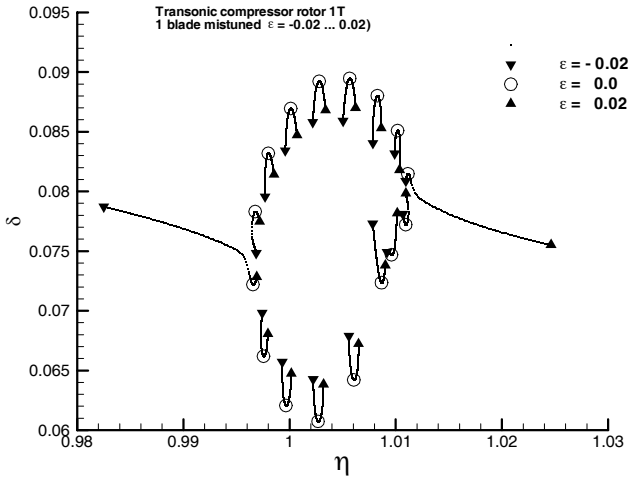


**Fig. 17: Eigenvalue trajectories for transonic compressor rotor 1T eigenmode with one blade mistuned ( ▼ : ε =-0.02, O : ε = 0, ▲ : ε = +0.02)**

The damping of the segregated eigenvalue tends to a slightly smaller value than for negative $\varepsilon$. This effect is explained by the type of mistuning introduced here: since we are changing the generalised stiffness, the elastic forces increase with increasing stiffness and hence with increasing frequency. The aerodynamic forces that supply the damping, on the other hand, remain unchanged, so that the ratio of damping to elastic forces goes down with increasing frequency.

Examining the trajectories of all eigenvalues for the whole range of $\varepsilon$ from –0.02 to +0.02, it can be found that the eigenvalues transition smoothly from $\varepsilon = -0.02$ via the tuned configuration to $\varepsilon = +0.02$, as could be expected. It is however interesting to note that the segregated eigenvalue for the negative values of $\varepsilon$ transitions into the lowest frequency eigenvalue of the tuned configuration, and is almost completely unaffected by the positive mistuning. On the other hand, the segregated eigenvalue for positive mistuning corresponds to the highest frequency eigenvalue for the tuned configuration, and again, its locus is hardly affected at all for the cases of negative mistuning.

The evolution of the localisation parameter $\psi$ for all eigenvectors over the whole range of the mistuning parameter $\varepsilon$ covered here is shown in Fig. 18. Starting from the values for $\varepsilon = -0.02$ that were given in Fig. 16, the values of $\psi$ converge towards 0 for the tuned configuration and then separate again for the positive values of $\varepsilon$, resulting in a configuration for $\varepsilon = +0.02$ that is very similar to the case of $\varepsilon = -0.02$. Interesting to note are the two small "humps" at $\varepsilon \approx \pm 0.002$. These indicate that one eigenvector shows a higher localisation for small values of $\varepsilon$, then "falling back" into line with the remaining, less localised eigenvectors. This behaviour can be explained by the asymmetry of the aerodynamic coupling coefficients, shown previously in Fig. 9. The higher induced forces in the direction of the suction side of the oscillating blade enable the mistuned blade to couple its suction side neighbour to its own vibration more strongly, so that these two blades separate slightly from the rest of the cascade. Since the in-vacuo eigenfrequency of this suction side neighbour is the same as for the rest of the cascade, this decoupling is only effective for a moderate magnitude of $\varepsilon$, forming the observed pair of localised eigenvectors. For higher magnitudes of $\varepsilon$, the aerodynamic forces cannot overcome the large eigenfrequency difference between the mistuned blade and its suction side neighbour, so that the localisation parameter drops back into the cluster of values that result from the eigenvectors with little participation of the mistuned blade.
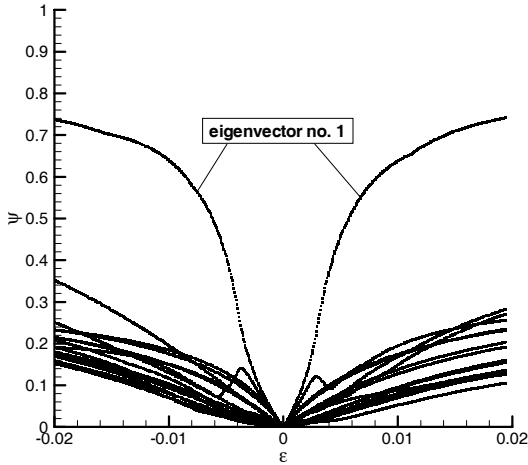
*Fig. 18: Eigenvector localisation parameter for transonic compressor rotor 1T eigenmode with*
*blade no.8 mistuned, ε = -0.02 to +0.02*

### 3.2.3 Alternating frequency mistuning

Another interesting configuration of mistuned blades is the case where the blade frequencies have one value for all the odd numbered blades and a different value for the even numbered blades. This is often termed "alternating mistuning". Fig. 19 shows the eigenvalue trajectories for the case with alternating mistuning ranging from the tuned case, denoted by the circles, up to a mistuning parameter of $\varepsilon = -0.02$ for the odd numbered and $\varepsilon = +0.02$ for the even numbered blades.

The picture shows that the eigenvalues for the mistuned configuration form two separate clusters, each of which constitutes a loop of 8 eigenvalues. The damping values tend towards the mean tuned value, very similar to the situation of the single mistuned blade. Consequently, the aeroelastic stability is increased with alternating mistuning, just like for the case of single blade mistuning. Furthermore, the eigenvalue trajectories show that the 8 low frequency eigenvalues of the mistuned configuration correspond to the lower frequency half of the tuned configuration eigenvalues, while the 8 high frequency eigenvalues of the mistuned configuration correspond to the high frequency half of the tuned configuration eigenvalues. Therefore, no eigenvalues travel "across" the tuned eigenvalue loop.
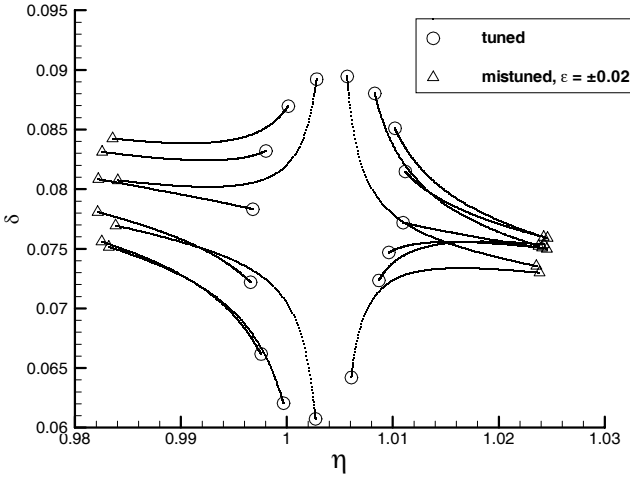
*Fig. 19: Eigenvalue trajectories for transonic compressor rotor 1T eigenmode with alternating mistuning, ( o: $\varepsilon = 0$, $\triangle$: $\varepsilon = \pm 0.02$)*

In Fig. 20, the localisation parameter $\psi$ is shown for all eigenvectors and for all values of the mistuning parameter $\varepsilon$ for the alternating mistuning case. Obviously, the individual modes are not very localised, even for the highest values of mistuning, where values of $\psi \approx 0.4$ are reached. This behaviour can be attributed to the fact that the cascade is actually split into two separate systems of 8 blades each, which for themselves remain tuned. Hence every second blade in each eigenvector will have identical amplitudes, explaining the moderate values of the localisation parameter $\psi$. On the other hand, the values of $\psi$ are considerably different for the different eigenvectors at constant values of the mistuning parameter. The reason for this is probably to be found in the variability of the unsteady aerodynamic forces with interblade phase angle, as seen in Fig. 10 and Fig. 11. Due to the different resulting coupling strengths, neighbouring blades with differing in-vacuo eigenfrequencies are interacting more or less, depending on the actual value of the interblade phase angle, and consequently the corresponding eigenvectors are more or less localised, as seen in Fig. 20.
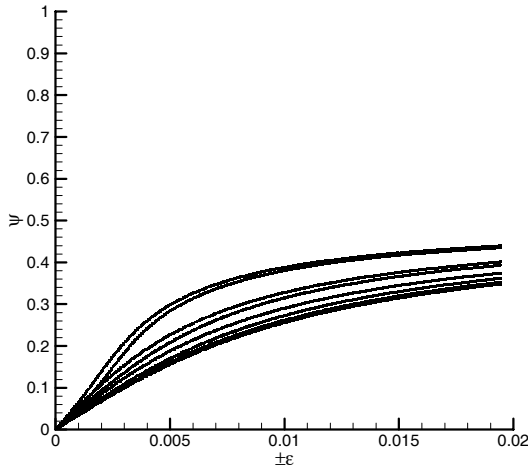
**Fig. 20: Localisation parameter for transonic compressor rotor 1T eigenmode with alternating mistuning, ε = 0 to ±0.02.**

### 3.2.4 Mechanical coupling

In the preceding examples, any mechanical coupling through the rotor disc has been neglected. In the following, the effect of mechanical coupling will be studied using a simplified model.

When the blades are mounted on a flexible disc, the disc adds flexibility at the blade root and introduces a coupling between the blades. The resulting system typically exhibits families of nodal diameter modes, for example a family of 1T modes [17]. In such a family, the frequency of the individual nodal diameter (ND) modes are different. For fairly stiff discs, the eigenmodes tend to be little different from the rigid disc ones. The eigenfrequencies for the low ND modes tend to be somewhat lower than the ones for the rigid disc, while the high ND eigenfrequencies are almost identical to the rigid disc ones. This behaviour can easily be modelled by reducing the generalised stiffnesses of the blades while at the same time introducing coupling stiffnesses between the identical modes of neighbouring blades. Setting the coupling stiffness $k_c$ as a fraction $\xi$ of the generalised stiffness k so that

$$k_c = \xi k \qquad (40)$$

then the condition of identical frequencies for the highest possible ND mode ( $ND = n_{blades}/2$ ) at $\sigma = 180°$ leads to the reduction of the generalised stiffness to

$$k^* = k \cdot (1 - 4\xi) \tag{41}$$

so that the reduction in generalised stiffness exactly compensates the coupling stiffnesses at this interblade phase angle. This will be termed "compensated coupling" in the following section.

Using this approach, the transonic compressor rotor was studied with a compensated coupling of 4%, i.e. $\xi = 0.04$.

Fig. 21 shows the corresponding eigenvalue locations (solid lines), with the dashed lines giving the rigid disc datum cases as reference. In these figures, the inset labels for some of the eigenvalues indicate the nodal diameters of the corresponding modes. It is obvious that the mechanical coupling leads to a spread of the eigenvalue frequencies, the lowest frequencies corresponding to the 0 ND ( $\sigma = 0°$ ) modes and the highest frequencies corresponding to the 8 ND ( $\sigma = 180°$ ) modes.
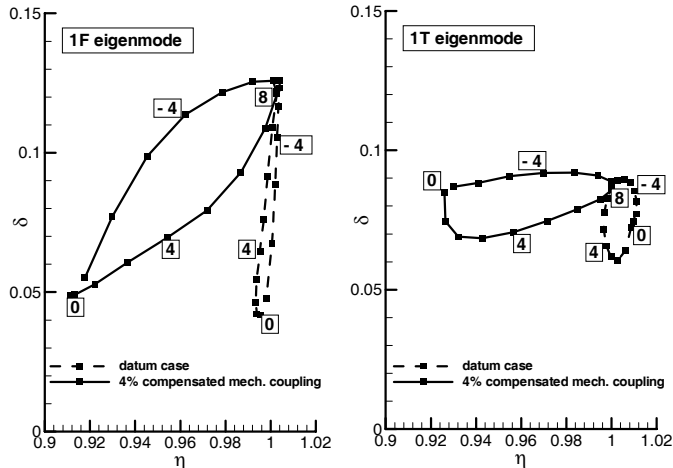


*Fig. 21: Eigenvalues of the transonic compressor rotor with 4% compensated mechanical coupling.*

*Left: (a) 1F eigenmode; Right: (b) 1T eigenmode.*

*Nodal diameters are indicated by the labels.*

For the latter ones, the resulting eigenvalues are identical to the rigid disc ones, just as expected. A significant difference between the flexible and the rigid disc eigenvalue solutions, however, is the direction in which the eigenvector loop is traversed for increasing nodal diameters, where the eigenvalue loops of the flexible disc are traversed in the opposite direction compared to the loops of the rigid disc. This holds true for both blade eigenmodes, 1F and 1T.

To assess the combined effects of mechanical coupling and frequency mistuning, the same frequency mistuning cases as for the mechanically uncoupled rotor have been evaluated. Fig. 22 shows the eigenvalue trajectories for the case with one blade mistuned from $\varepsilon = -0.02$ to $\varepsilon = +0.02$ and 4% compensated mechanical coupling. The meaning of the symbols used is the same as in Fig. 17.

In comparison to the mechanically uncoupled case, the cascade eigenfrequencies are less affected, while the change in the damping values is comparable in both cases. Similar to the mechanically uncoupled case, the eigenfrequencies do not show a notable change until the magnitude of the mistuning exceeds the frequency spread of the tuned eigenvalues.
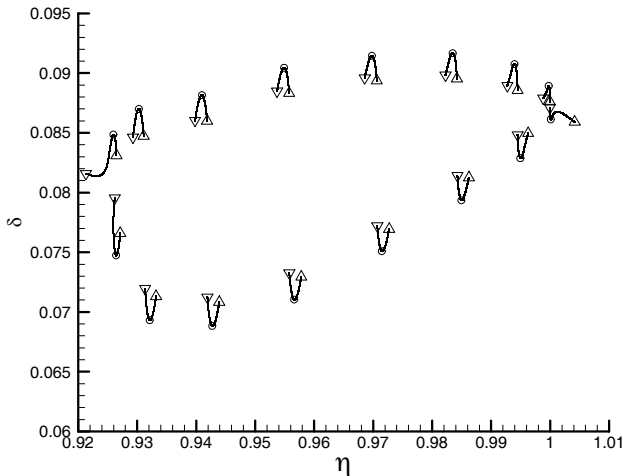


**Fig. 22: Eigenvalue trajectories for transonic compressor rotor 1T eigenmode with one blade mistuned ( ∇: ε = -0.02, o: ε = 0, Δ: ε = 0.02) and 4% compensated mechanical coupling**

The same effect is obvious in Fig. 23, where the alternating mistuning pattern of Fig. 19 is imposed on the mechanically coupled rotor. Again, the changes in eigenfrequencies are much less pronounced than for the mechanically uncoupled system, while the changes in the damping values are of comparable magnitude in both cases. Just like previously observed for the cases without mechanical coupling, where the damping of the least stable eigenvalue increases with increasing mistuning, the same holds true for the cases with mechanical coupling as well. In the case shown here, the increase in damping for the least stable eigenmode is so strong that the least stable eigenvalue of the mistuned configuration is different from the one of the tuned configuration.
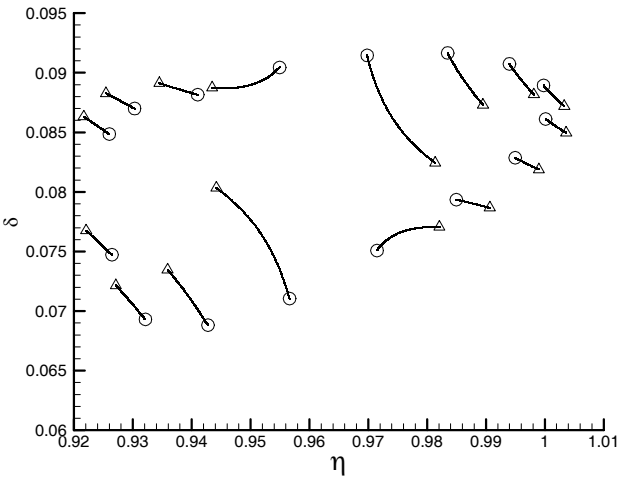


**Fig. 23: Eigenvalue trajectories for transonic compressor rotor 1T eigenmode with alternating mistuning, ( o: ε = 0, Δ: ε = ±0.02) and 4% compensated mechanical coupling.**

### 3.2.5  Damping mistuning

The individual blades in a real turbomachine cascade will differ from each other not only with respect to their in-vacuo eigenfrequency, but also with respect to their individual mechanical damping. This can be attributed for example to small differences in the firtree roots that will influence the precise location of contact points between the blade and the disc. Although this will certainly be the case, the actual amount of damping mistuning occurring in practice is very hard to assess. Since this property cannot be measured for a blade alone but only becomes apparent for the assembled, rotating cascade where the

blades are forced into their operating position by the centrifugal forces, it is almost impossible to accurately measure the amount of mechanical damping acting on each blade. Nevertheless, the possible effects of damping mistuning will be demonstrated for a generic example in the following section.

For this purpose, the 1T eigenmode of the transonic compressor without mechanical coupling between the blades is used, where mechanical damping is assigned to every second blade while the rest of the blades remain free of mechanical damping.
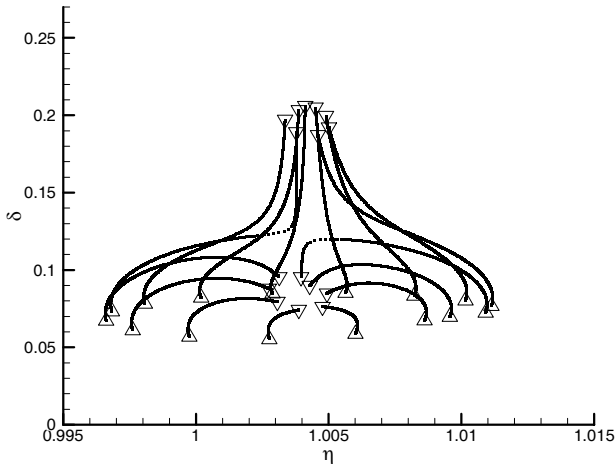


*Fig. 24: Eigenvalue trajectories for transonic compressor rotor 1T eigenmode with alternating damping mistuning, (Δ: $\delta_{mech} = 0$, ∇: $\delta_{mech} = 0 / 0.14$).*

In Fig. 24 the eigenvalue trajectories for this case of alternating damping mistuning are shown for mechanical damping values varying from $\delta_{mech} = 0$ to $\delta_{mech} = 0.14$. The Δ symbols denote the tuned situation without mechanical damping, while the ∇ symbols indicate the configuration with maximum mistuning, where every second blade has a mechanical damping value of $\delta_{mech} = 0.14$. Similar to the situation with alternating frequency mistuning shown in Fig. 19, the eigenvalues separate into two distinct clusters with increasing mistuning strength. Unsurprisingly, one of the clusters shows much larger damping values, indicative of the fact that these eigenvalues correspond to the eigenvectors with strong participation of the mechanically damped blades, while the damping values for the remaining eigenvalues stay at approximately the same level as for the tuned eigenvalues. What is interesting, though, is the observation that the

aeroelastic eigenfrequencies converge with increasing mistuning. This could be due to the circumstance that the influence of neighbouring blades, corresponding the strongest influence coefficients in the tuned case, is much decreased as the neighbouring blades get more and more decoupled due to the damping mistuning.

The damping of the least stable eigenvalue increases with increasing damping mistuning, so that the cascade becomes aeroelastically more stable, just like in the previously investigated cases of frequency mistuning. Some of the eigenvalues exhibit a more complicated behaviour. A number of the eigenvalues that converge towards the cluster with lower damping exhibit an increase in damping values for moderate damping mistuning, then their damping values drop down again for the high damping mistuning cases. This indicates that these specific eigenvalues become less stable, although more mechanical damping is introduced into the complete system.

### 3.2.6 Modal coupling

The previous examples addressed the effects of various types of mistuning and coupling of a single mode on the eigenvalues of the cascade. In the following, the effects of coupling between two different modes will be studied.

In the current rotor, the 1F and 1T eigenfrequencies are spaced far apart. Due to this large frequency separation, the two eigenmodes show no coupling due to structural or aerodynamic interaction in practice. To evaluate the effects of such coupling, it is therefore necessary to significantly change the structural parameters of the rotor.

In this example, the generalised stiffness of the bending mode is increased, so that the bending eigenfrequency comes close to the torsional eigenfrequency. This is not achieved by any special geometric modification, but by assuming unchanged eigenmodes and just varying the generalised quantities accordingly. It is of course realised that in a real configuration, such a change in bending eigenfrequency cannot be achieved without a change in geometry so significant that it will also significantly affect the bending eigenmode as well as the frequency and modeshape of the torsional eigenmode. As such, the current study is intended as an academic example to show the effects of modal coupling that can arise if the eigenfrequencies lie close to one another, but not as a real-world case closely linked to the existing rotor geometry.

To quantify the effects of the coupling between different structural modes of the blades on the aeroelastic eigenvalues and eigenvectors of the cascade, two additional parameters are needed. The first of these describes the magnitude of the frequency split between the bending and torsional in-vacuo eigenfrequencies on the blades.

Due to its similarity to the single mode mistuning parameter, it will be termed "modal mistuning" and is defined by

$$\varepsilon_m = \frac{\omega_{vac,1F}}{\omega_{vac,1T}} - 1 \qquad (42)$$

Accordingly, a value of $\varepsilon_m = 0$ corresponds to the case where the bending and torsional in-vacuo eigenfrequencies coincide. The original case, where the bending and torsional blade in-vacuo eigenfrequencies differed by a factor of almost 2 ($\varepsilon_m \approx$ -0.5), showed aeroelastic eigenvectors of the cascade that either were of a predominantly torsional or predominantly bending type. This may not be the case if the value of $\varepsilon_m$ is close to zero. To asses the amount of coupling between bending and torsion for these cases, a modal coupling parameter $\chi$ is defined. It is calculated for each blade $k$ of the cascade by relating the difference between the magnitudes of the torsional component $a_{k,1T}$ and the bending component $a_{k,1F}$ to the sum of the two. The resulting value is averaged over all the blades of the cascade:

$$\chi = \frac{1}{n_{blade}} \sum_{k=1}^{n_{blade}} \frac{|a_{k,1T}| - |a_{k,1F}|}{|a_{k,1T}| + |a_{k,1F}|} \qquad (43)$$

In the current case, where all blades of the cascade have identical ratios of bending to torsional in-vacuo eigenfrequencies, the amplitude ratios will also be identical, so that the averaging over all blades is not strictly necessary. It is nevertheless retained for completeness.

The values of $\chi$ give a clear indication of the cascade eigenvector types. A pure bending eigenvector will have no torsional component, resulting in a value of $\chi =$ -1. Similarly, a pure torsional cascade eigenvector will yield a value of $\chi =$ +1. In case of a strong coupling between bending and torsion, where both components are of the same magnitude in an individual eigenvector, the modal coupling parameter will be $\chi = 0$.

In the first example, the generalised stiffness of the 1F mode is adjusted so that the in-vacuo eigenfrequency of the bending mode is equal to 0.97 of the torsional eigenmode, hence $\varepsilon_m =$ -0.03. In Fig. 25 (left), the resulting eigenvalues of the cascade are shown, where the damping $\delta$ is plotted over the frequency ratio $\eta_{1T}$ relative to the torsional in-vacuo eigenfrequency. In this case, the eigenvalues still form two distinct clusters, one cluster corresponding to the cascade eigenvectors with predominantly bending motion, the other, with significantly higher damping, belonging to the eigenvectors with predominantly torsional motion.

*Fig. 25: Eigenvalues of the transonic compressor rotor for the 1F in-vacuo eigenfrequency set to 97% of the 1T in-vacuo eigenfrequency ($\varepsilon_m$= -0.03).*

*Left: Damping over frequency ratio. Right: Coupling parameter over frequency ratio.*

This is confirmed by Fig. 25 (right), where the modal coupling parameter $\chi$ is plotted over $\eta_{1T}$ for all eigenvalues. The lower cluster corresponds to the (low frequency) bending eigenvectors / eigenvalue pairs, while the upper cluster corresponds to the ones dominated by torsional motion. The latter exhibit a certain amount of coupling with the bending modes already, which is expressed by the values of $\chi$ ranging from approximately 0.35 to 0.75.

By further increasing the generalised stiffness of the bending eigenmode, we arrive at a case where the in-vacuo bending eigenfrequency almost coincides with the torsional eigenfrequency. This case is shown in Fig. 26. Here, the previous structure of two separate clusters has almost completely dissolved into a single cluster of eigenvalues. This behaviour implies a case with strong coupling between the two structural blade eigenmodes, where a clear distinction of the aeroelastic cascade eigenmodes into "bending" and "torsion" modes is no longer possible, since most eigenvectors contain significant contributions of both bending and torsional components. In Fig. 26 (right), it can also be found that the values of $\chi$ do not form two distinct clusters any more, but rather merge into one another, very similar to the damping values.
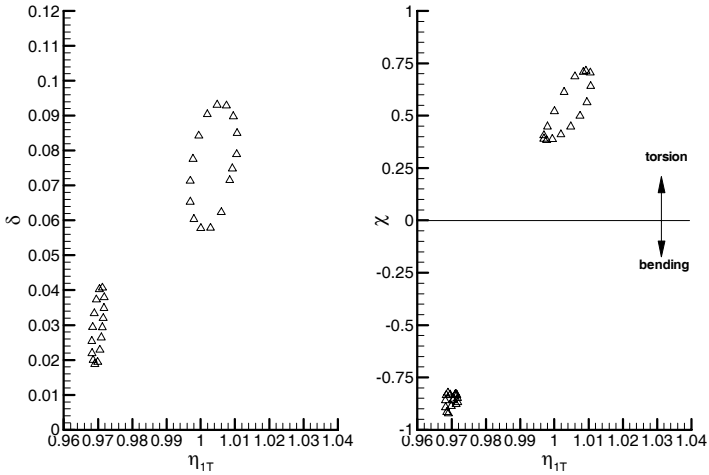
*Fig. 26: Eigenvalues of the transonic compressor rotor for the 1F in-vacuo eigenfrequency at 0.997 of the 1T in-vacuo eigenfrequency ($\varepsilon_m$= -0.003).*

*Left: damping over frequency ratio. Right: Coupling parameter over frequency ratio.*

The values range from approximately $\chi$ = -0.8 to $\chi$ = +0.5, with a large number of eigenvectors clustering about $\chi$ = 0, which corresponds to equal magnitudes of the bending and torsion components.

Increasing the bending generalised stiffness even further, so that the in-vacuo bending eigenfrequency now is at 1.03 times the in-vacuo torsional eigenfrequency yields the eigenvalue distribution shown in Fig. 27. In this case, the eigenvalues (Fig. 27, left) have again separated into two distinct clusters, indicating a much lower coupling of the blade structural eigenmodes. However, the deformations apparent in the two eigenvalue clusters indicate that some coupling still is present in this configuration.

This is confirmed by Fig. 27 (right), where the modal coupling parameter for the torsion dominated eigenvectors ranges between 0.25 and 0.6, indicating considerable bending components in these eigenvectors.
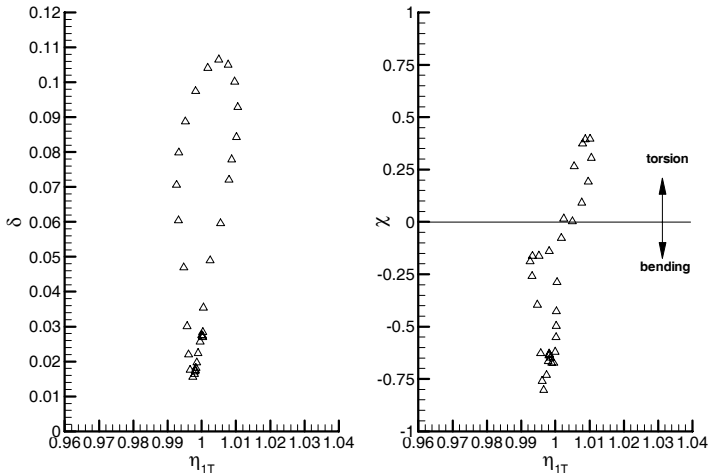
*Fig. 27: Eigenvalues of the transonic compressor rotor for the 1F in-vacuo eigenfrequency at 1.03*

*of the 1T in-vacuo eigenfrequency ($\varepsilon_m$= +0.03).*

*Left: damping over frequency ratio. Right: Coupling parameter over frequency ratio.*

Finally, the trajectories of the eigenvalues for the whole range of generalised bending stiffnesses is depicted in Fig. 28. In this picture, the three previous left-hand side figures have been assembled, and the trajectories of the eigenvalues for the values in between are indicated by dotted lines. For clarity, only every second eigenvalue has been plotted in this picture. It is interesting to note that the eigenvalues can be classified into two groups for this case. Two eigenvalues initially belonging to the 1F cluster actually merge into the 1T cluster, being replaced by the two of the eigenvalues initially belonging to the 1T cluster, which move down into the 1F cluster for the high 1F stiffness cases. The remaining eigenvalues of the 1F cluster actually travel across the plot with only a small "dip" in their damping values. Correspondingly, the remaining 1T eigenvalues traverse a small loop through somewhat higher damping values and finally end up very close to their initial locations.
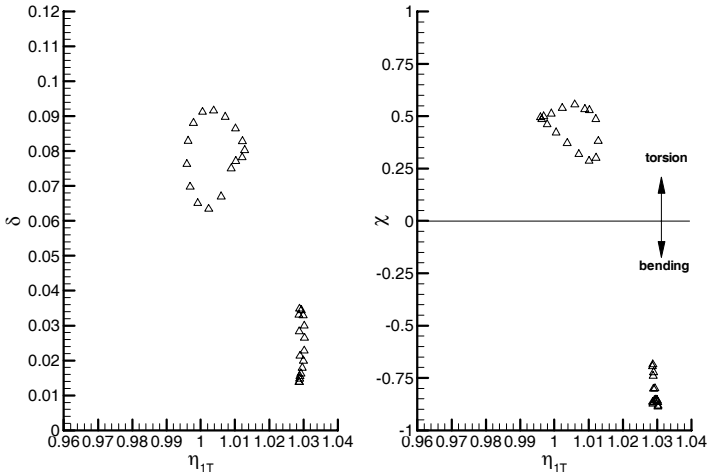
**Fig. 28 Eigenvalues of the transonic compressor rotor for the 1F in-vacuo eigenfrequency varying from 0.97 to 1.03 of the 1T in-vacuo eigenfrequency ($\varepsilon_m$= -0.03 to +0.03). Every second eigenvalue shown.**

The described behaviour is confirmed by the variation of the coupling parameter $\chi$ shown in Fig. 29. Here, $\chi$ is plotted as a function of the modal mistuning parameter $\varepsilon_m$. The range of $\varepsilon_m$ has been extended to $\varepsilon_m = \pm 0.05$. The figure shows how the modal coupling increases when the bending and torsional in-vacuo eigenfrequencies grow close to each other. Near $\varepsilon_m = 0$, the transition of a number of eigenvectors from predominantly bending to torsional behaviour or vice versa is apparent, while others only show increased coupling for a certain interval of $\varepsilon_m$ and then return to their original motion type. Another observation is that the maximum coupling levels for the individual eigenvalues do not all occur when the in-vacuo eigenfrequencies of bending and torsion are identical (i.e. $\varepsilon_m = 0$), but occur at different values of $\varepsilon_m$, ranging from approximately $\varepsilon_m = -0.01$ to $\varepsilon_m = +0.02$. This effect corresponds to the spread of the tuned aeroelastic eigenvalues over different values of $\eta$ (see Fig. 12) due to the in-phase components of the aerodynamic forces.

These observations are consistent with the ones made for the single mode mistuning cases. The initial configuration as well as the final one, with a fairly large separation of the in-vacuo eigenfrequencies, can be understood as a case with large "mistuning"

between the two modes. This leads to well separated eigenvalue clusters with a small spread in the damping values, just as shown in the single mode / alternating mistuning case of Fig. 19. In the case of large coupling, when the in-vacuo eigenfrequencies of the torsional and the bending mode are very close, the complete system forms a single cluster of eigenvalues and the spread of the corresponding damping values is maximised. This in turn corresponds to the "tuned" configuration in Fig. 19.



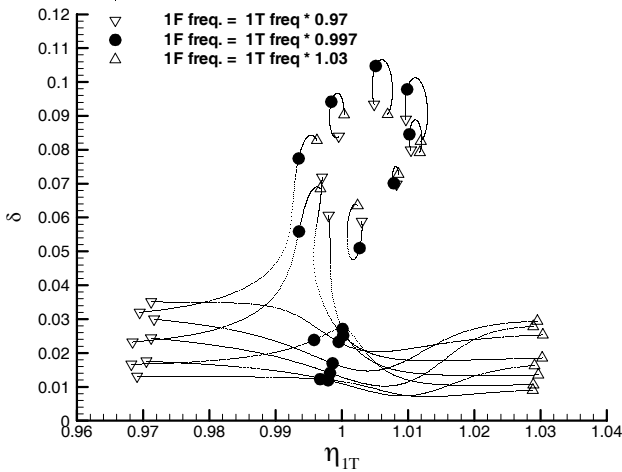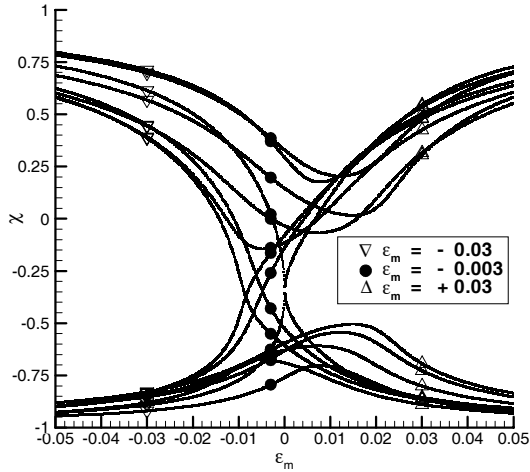*Fig. 29: Modal coupling of the transonic compressor rotor for the 1F in-vacuo eigenfrequency*
*varying from 0.95 to 1.05 of the 1T in-vacuo eigenfrequency ($\varepsilon_m$= -0.05 to +0.05) .*

### 3.2.7   Summary of section 3.2

In this section, the transonic compressor rotor was exhaustively analysed with respect to its aeroelastic eigenvalues.

- Analysis of the aerodynamic influence coefficients revealed significant directional asymmetry, the forces exerted by the suction side pressure field on the pressure side of the neighbouring blade are considerably larger than vice versa.

- Starting from the tuned datum configuration, it was shown that the effect of the unsteady aerodynamic forces on the aeroelastic eigenfrequencies is small, with at most 1.1% change in frequency. Consequently, the resulting distribution of aerodynamic damping when computed using the energy method is almost indistinguishable from the values resulting from the eigenvalue method. The

cascade under consideration features blades made of carbon fibre reinforced plastics with a small mass parameter, while commonly used cascades are made of metal, where the mass parameter is significantly higher and the corresponding effects will be even smaller. It is concluded that the energy method is well justified for tuned turbomachinery cascades.

- Three parameters were defined, the mistuning parameter $\varepsilon$ characterising the amount of variation of the in-vacuo eigenfrequencies, the localisation parameter $\psi$ indicating how strongly a certain eigenvector is localised on one or a few blades of the cascade and the modal coupling parameter $\chi$, which relates to the amount of coupling between different blade structural eigenmodes in a single cascade eigenvector.

- Frequency mistuning of a cascade with a single degree of freedom on each blade was studied for single blade mistuning and alternating mistuning, with and without structural coupling between adjacent blades. In any case, the mistuning results in the decoupling of the mistuned blade(s) from the rest of the cascade, which in turn leads to the aeroelastic eigenfrequencies separating from one another. At the same time, the decoupling results in the damping of the eigenvalues converging towards a mean value. This implies that the damping of the least stable eigenvalue increases, making the cascade aeroelastically more stable. When structural coupling is present, it inhibits the decoupling of the blades to a certain degree, so that the separation of the eigenvalues is less pronounced.

- If alternating damping mistuning is introduced in the cascade, a similar decoupling is apparent, where now the damping values of the two sets of eigenvalues separate, while the frequencies converge towards a mean value.

- Assigning each blade two eigenmodes as degrees of freedom and varying their frequency separation, a strong coupling between the different modes becomes apparent when the difference in the in-vacuo eigenfrequencies is small. For the current case, significant effects were observed if the differences in frequencies were below approximately 3%. Under these conditions, the formerly separated clusters of eigenvalues unite into a single set, where each eigenvector contains considerable components of both vibration modes. In such cases, the simplifications used in the energy method cannot be applied any longer, since this relies on the assumption that each mode can be treated separately. Consequently, an approach like the one presented here is an absolute necessity for the analysis of cases with closely spaced eigenmodes.

- When comparing the alternating frequency mistuning and the modal coupling cases, large similarities can be observed. If the frequencies of the same mode on neighbouring blades or of the two modes on the same blade are spaced far apart, two separate clusters of eigenvalues are formed. Each cluster is restricted to a comparably small range of damping values. When the frequencies are very close to one another, the two clusters merge into a single, large one, where the spread of the damping values is increased significantly.

## 3.3    Forced excitation

### 3.3.1   Datum case

In this section, some examples of the mistuning and coupling effects on the resonant response of the transonic compressor rotor will be shown and discussed in detail. For these analyses, it will be assumed that the inflow into the rotor is not circumferentially uniform, but contains some small variations. For example, a square inlet section would create an inflow pattern with four similar disturbances spaced evenly around the circumference. As the rotor blades rotate through these disturbances, each blades is subjected to the changes in inflow conditions four times per revolution, hence it is excited at a frequency of four times the rotational speed of the rotor. These excitations with excitation frequencies as multiples of the engine shaft speeds are typical for turbomachinery rotors. They are often referred to as "engine order excitations", hence the example of the square inlet given above would cause a 4th engine order excitation. In the case of a tuned rotor with identical blades, such an engine order excitation will cause all blades to vibrate identically, but with a constant phase shift between the motions of the individual blades. This phase shift corresponds to the   time delay with which neighbouring blades pass through the disturbed inflow, and it is also referred to as the interblade phase angle, $\sigma$. With the excitation engine order $EO$, $\sigma$ can be calculated as

$$\sigma = \pm \frac{EO \cdot 360°}{n_{blades}} \qquad (44)$$

where the sign of $\sigma$ is defined by the direction of the rotor rotation. With the co-ordinate conventions used in the current analysis, $\sigma$ is negative for compressors and positive for turbines.

For the tuned transonic compressor rotor with 16 blades, the given example of a 4th engine order excitation corresponds to a backward travelling disturbance in the rotor frame of reference. The interblade phase angle for this case is $\sigma$ = -90°, which is equivalent to $\sigma$ = 270° in terms of blade vibration.

In the following, the steady flow is assumed to remain fixed at the design flow conditions, while the excitation frequency is varied so that all blades sweep through their resonant frequency. The strength of the excitation is set to a fixed value that corresponds to the force necessary to produce 1µm static deflection (at zero frequency) at the tip trailing edge. This point is the location of the maximum deflection for the 1T mode, and it is close to the point of maximum deflection for the 1F mode.



**Fig. 30: Tip trailing edge response amplitude (left) and phase (right) of the transonic compressor rotor under 4th EO excitation. Phases individually referenced to each blade's excitation.**

Fig. 30 (left) shows the resulting response amplitude of all blades. Naturally, all blades show the same response to the excitation, since the rotor is tuned and all blades are assumed to be identical. The in-vaco eigenfrequencies and the response amplitudes at the corresponding excitation frequencies are marked by symbols. These indicate that the maximum response amplitude for the 1T mode occurs at a slightly higher frequency than the in-vacuo eigenfrequency of the blades, while the 1F maximum response coincides almost exactly with its in-vacuo eigenfrequency value. The 4th EO excitation acting on the cascade leads to a corresponding phase difference of $\sigma$ = 90° in the responses of neighbouring blades. For the tuned case, all blades have the same phase delay with respect to the generalised forces acting on themselves. This is shown in Fig. 30 (right), where the phases of all blades are individually referenced to the 1F generalised force

acting on the respective blade, so that the identical behaviour of all blades becomes apparent.

### 3.3.2   Single blade frequency mistuning

The simplest case of mistuning, again, is the variation of one eigenfrequency of a single blade. As an example, the 1T eigenfrequency of blade number 8 will be lowered by 2%, i.e. $\varepsilon = $ -0.02. For the case under consideration here, the 1F and 1T eigenfrequencies differ by a factor of almost 2, so that there is very little interaction between the two eigenfrequencies and eigenmodes in the datum case. Consequently, the mistuning in the 1T eigenmode produces no visible changes for the 1F responses, as can be found in Fig. 31.
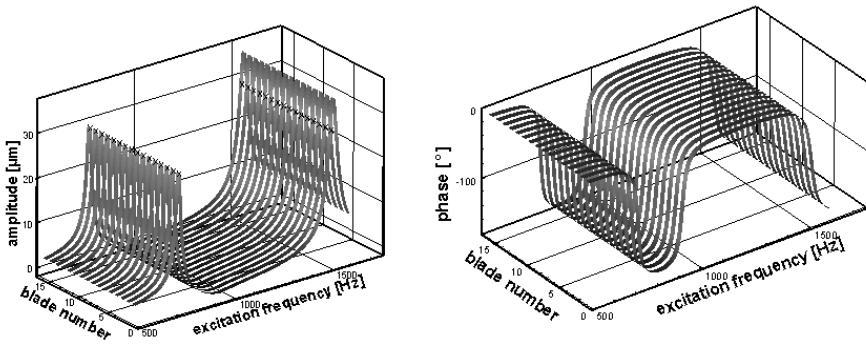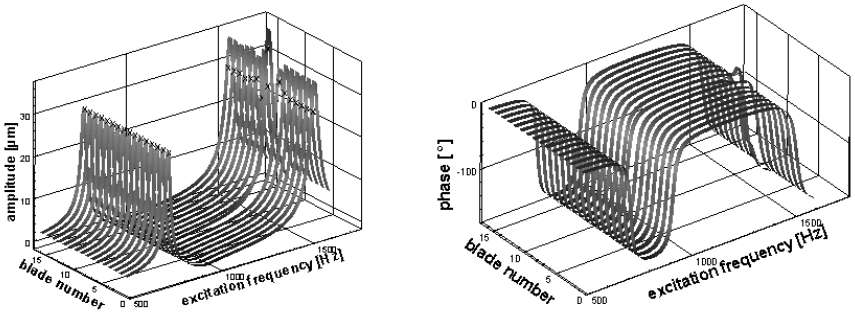


*Fig. 31: Tip trailing edge response amplitude (top) and phase (bottom) of the transonic compressor rotor under 4th EO excitation. Phases individually referenced to each blade's excitation. Blade 8 1T mode mistuned by ε = -0.02.*

It is apparent that the effect of the mistuning in this case is restricted to the 1T resonant response of the mistuned blade itself and its immediate neighbours. This region of special interest is shown in Fig. 32 in more detail, where the response amplitudes of blades 7 through 10 are shown for excitation frequencies ranging from 1400 Hz up to 1600 Hz, along with the values for the tuned configuration of Fig. 30. In Fig. 32, the tuned 1T in-vacuo eigenfrequency of 1505 Hz and the blade 8 mistuned eigenfrequency of 1475 Hz are marked by the vertical grey bars for easier reference. Obviously, the maximum amplitude for the mistuned blade 8 is significantly lower than for the tuned case, by approx. 14%. The highest maximum amplitude arises at blade 9 (situated next to the suction side of blade 8), exceeding the tuned value by approximately 19%. The

remaining blades, including blade 7 to the pressure side of blade 8, show only small deviations from their tuned mode behaviour.



*Fig. 32: Tip trailing edge response amplitude for blades 7 through 10 of the transonic compressor rotor 1T eigenmode under 4<sup>th</sup> EO excitation, blade 8 1T mode mistuned by ε = -0.02. Dashed line shows tuned configuration for reference.*

For easier comparison of different configurations, it is useful to restrict the graph to the maximum amplitudes of the individual blades only, as shown in Fig. 33.



*Fig. 33: Tip trailing edge maximum response amplitude of the transonic compressor rotor 1T eigenmode under 4<sup>th</sup> EO excitation, blade 8 1T mode mistuned by ε = -0.02. Dashed line shows tuned configuration for reference.*

Retaining the simple example of a single mistuned blade in an otherwise tuned cascade, it is interesting to study the effect of varying mistuning strength on the resonant response. Fig. 34 shows the resulting maximum tip amplitudes for all blades, where the 1T mode of blade 8 is mistuned in the range of $\varepsilon$ = -0.25 to $\varepsilon$ = +0.25. The results are shown as a carpet plot, corresponding to Fig. 33, with an additional axis perpendicular to the drawing plane showing the dependence on the mistuning parameter $\varepsilon$. The height of the surface corresponds to the maximum amplitude, additionally, contour lines are shown for clarity. For all values of $\varepsilon$, the effect of the mistuned blade 8 remains restricted to the response amplitudes of blades number 7 through 10. The rest of the blades show very little differences to their tuned mode behaviour. Taking a closer look at blades 7 though 10, the structure of the amplitude distribution is very similar for values of the mistuning strength below approximately $\varepsilon$ = -0.1 and above approximately $\varepsilon$ = +0.1. For these values, blade 7 exhibits a significantly lower amplitude than for the tuned case, while the response of blades 8, 9 and 10 considerably exceeds the tuned mode maximum response.



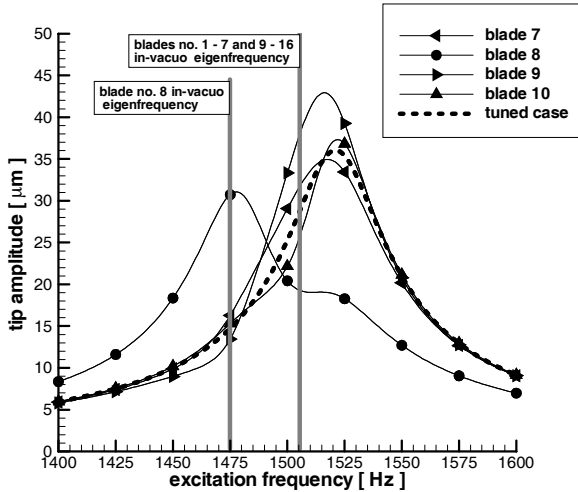**Fig. 34: Tip trailing edge maximum response amplitude of the transonic compressor rotor 1T eigenmode under 4th EO excitation, blade 8 1T mode mistuning varied from ε = -0.25 to ε =+0.25.**

In the region close to the tuned configuration however, i.e. for values of the mistuning strength between $\varepsilon$ = -0.1 and $\varepsilon$ = +0.1, the distribution of the maximum amplitudes on blades 7 through 10 show a large degree of variability that is difficult to assess from the carpet plot shown in Fig. 34. Therefore, the distributions of the maximum response

amplitude for these blades is plotted as a function of the mistuning strength $\varepsilon$ in Fig. 35. This graph corresponds to a number of cuts through the surface of Fig. 34 at values of constant blade number.
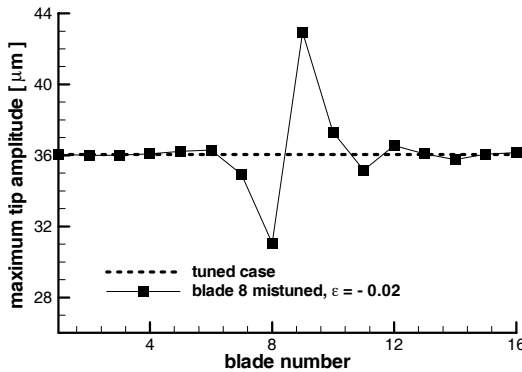


*Fig. 35: Tip trailing edge maximum response amplitude of the transonic compressor rotor 1T eigenmode under 4th EO excitation, blade 8 1T mode mistuning varied from $\varepsilon$ = -0.25 to $\varepsilon$ = +0.25.*

A number of points are worth noting about this figure. Looking at the mistuned blade, number 8, which is shown by the solid lines with the filled symbols, it can be seen that its maximum amplitude is above the tuned value (approximately 36 µm) for all values of the mistuning parameter except in a small range between $\varepsilon$ = -0.05 and $\varepsilon$ = 0, where its maximum amplitude drops significantly.

A similar observation can be made for blade number 9 (denoted by the $\Delta$ symbols), where the maximum amplitude falls below the value of the tuned configuration only in a range of the mistuning parameter between $\varepsilon$ = 0.0 and $\varepsilon$ = +0.03. On the other hand, the maximum amplitude for blade 10 ($\triangleright$ symbols) exceeds the tuned value for the whole range of the mistuning parameter $\varepsilon$, and similarly, the maximum amplitude of blade 7 ($\triangleleft$ symbols) remains below the tuned value all the time. Nevertheless, the maximum amplitude of all blades in the mistuned cascade exceeds the value of the tuned configuration in all cases considered here.

In the tuned configuration, the resonant response of the blades is strongly dependent on the interblade phase angle, which is directly coupled to the engine order of the

excitation, as shown in eq. (44). This is due to the variability of the aerodynamic damping with respect to the interblade phase angle, shown in Fig. 10. Similarly, the effects of mistuning on the amplitudes can change dramatically with a change in interblade phase angle.
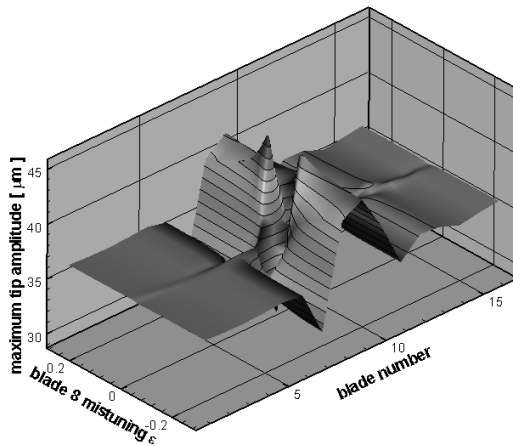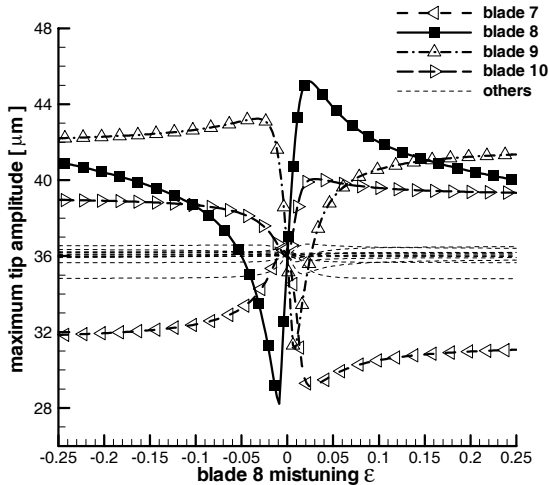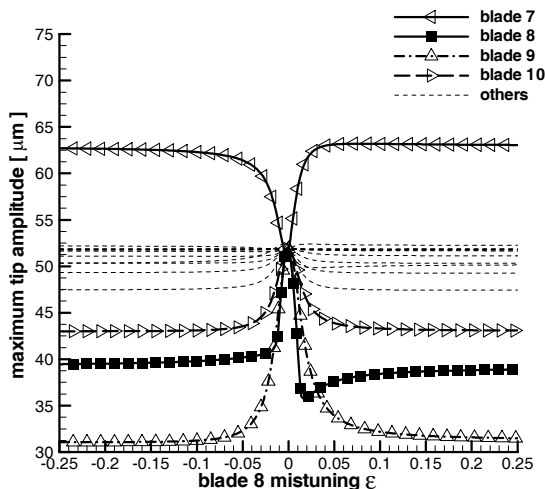


*Fig. 36: Tip trailing edge maximum response amplitude of the transonic compressor rotor 1T eigenmode under 18th EO excitation, blade 8 1T mode mistuning varied from $\varepsilon= -0.25$ to $\varepsilon= +0.25$.*

In Fig. 36, the maximum blade amplitudes are shown for a case that is identical to the one above, but with the interblade phase angle changed to $\sigma = 45°$, corresponding to an 18th EO excitation. In general, the overall amplitude level is considerably higher than for the 4th EO case, reflecting the lower aerodynamic damping of the tuned case. Furthermore, and in contrast to Fig. 35, the amplitudes of blade 7 are now significantly above the tuned value for the whole range of the mistuning parameter $\varepsilon$, while the amplitudes of blades 8, 9 and 10 are now well below the tuned configuration values. Consistent with the 4th EO case, the remaining blades 1-6 and 11-16 are largely unaffected by the blade 8 mistuning. Finally, for all mistuned cases, the maximum amplitude of all the blades always exceeds the tuned configuration value - an observation that was also made for the 4th EO case.

From the designers perspective, the values of interest are the highest amplitudes occurring on any blade for a given mistuning parameter. This corresponds to the upper

envelope of the curves given in Fig. 35 or Fig. 36, regardless of the fact on which blade these maximum values occur in the specific configuration.



*Fig. 37: Tip trailing edge maximum response amplitude of the transonic compressor rotor 1T eigenmode, excitation interblade phase angle varied, maximum of all blades shown. Blade 8 1T mode mistuning varied from $\varepsilon = -0.25$ to $\varepsilon = +0.25$.*

In Fig. 37, these maximum values are plotted for the complete range of interblade phase angles and for the mistuning parameter in the range of $\varepsilon = -0.25$ to $\varepsilon = +0.25$. The mistuned values are given as thin lines, while the reference tuned configuration at $\varepsilon = 0$ is indicated by the thick line marked with diamond symbols. It is apparent that the tuned case is always forming the lower limit of all the mistuned cases considered here.

### 3.3.3 Alternating frequency mistuning

Using the data reduction techniques described in the preceding section, the forced response behaviour of the transonic compressor rotor under alternating frequency mistuning can be explored. In this case, the cascade still possesses a significant symmetry, since every second blade is the same, with periodicity ensured since the rotor features an even number of blades. Consequently, the response behaviour of every second blade is also identical, and thus it is sufficient to investigate any two neighbouring blades.

In section 3.2.3, it was shown that the eigenvalues of the alternately mistuned cascade show a separation of the frequencies according to the blade in-vacuo eigenfrequency

split, but the aerodynamic damping of these eigenvalues converges towards the mean value of the tuned configuration. This is due to the decoupling of neighbouring blades with increasing frequency separation. The convergence of the aeroelastic damping towards the mean value indicates that the damping increases for some values of the interblade phase angle, which should in turn result in lower resonant response amplitudes for these cases. On the other hand, the amplitude for interblade phase angles with tuned damping values above the average should show decreasing damping and thus increasing response amplitudes.

Referring back to Fig. 10, the $4^{th}$ EO ($\sigma = 270°$) case is identified to have an aerodynamic damping near the maximum, while the $18^{th}$ EO ($\sigma = 45°$) is found close to the minimum value. In Fig. 38, the responses for these two excitation EOs are compared for alternating mistuning, the mistuning parameter ranging from $\varepsilon = 0$ to $\varepsilon = 0.05$, i.e. for maximum mistuning, neighbouring blades are off the tuned in-vacuo eigenfrequency by +5% and -5%, respectively. The circles identify the $4^{th}$ EO excitation case, while the triangles denote the $18^{th}$ EO case. Furthermore, the filled symbols show the amplitude response of the blades with negative mistuning (low frequency), the open symbols stand for the remaining, high frequency blades.
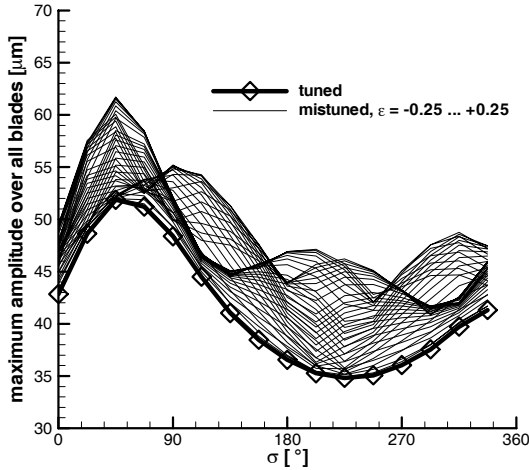


*Fig. 38: Tip trailing edge maximum response amplitude of the transonic compressor rotor 1T eigenmode, excitation interblade phase angle $\sigma = 45°$ and $\sigma = 270°$. Alternating frequency mistuning varied from $\varepsilon = 0$ to $\varepsilon = \pm0.05$, odd and even numbered blade response shown.*

As expected, all blades of the mistuned cascade under 18th EO excitation show smaller responses than for the tuned case, while in the 4th EO excitation case, the high frequency blades significantly exceed the tuned case amplitude for all values of $\varepsilon$. The low frequency blades in this case exhibit lower response amplitudes than for the tuned case in the range of $\varepsilon = 0$ to $\varepsilon \approx \pm 0.02$. For higher values of $\varepsilon$, their amplitudes exceed the tuned response by a small fraction.

In Fig. 39, the maximum response of all blades as a function of interblade phase angle and with varying alternating mistuning is shown. The solid lines denote the extremal values of $\varepsilon$, marked with diamonds for $\varepsilon = 0$ and with circles for $|\varepsilon| = 0.05$.

The figure illustrates the complicated dependence of the response amplitudes for the cascade with alternating mistuning on both mistuning strength and excitation interblade phase angle. As discussed above, the response amplitude increases with mistuning strength for $\sigma = 45°$ and decreases for $\sigma = 270°$. For $\sigma = 90°$, however, the response amplitudes for small mistuning strengths exceed the tuned values, then decrease when $\varepsilon$ rises further and fall below the tuned response amplitudes for values of $\varepsilon \approx 0.05$. Obviously, in this case no simple rule like "mistuning increases the response amplitudes" exists, but rather all relevant configurations have to be analysed to assess the possible consequences of mistuning on the resonant amplitudes.
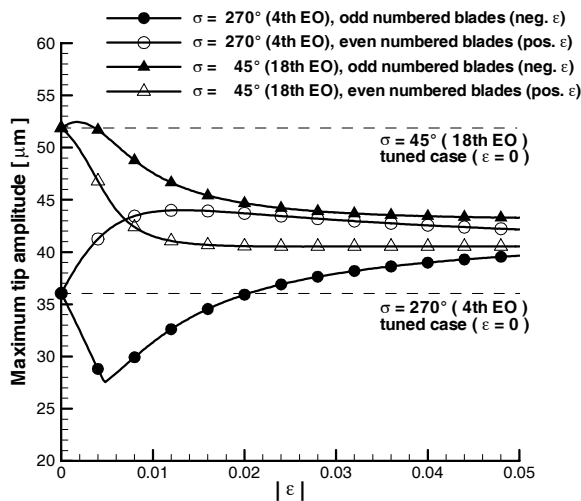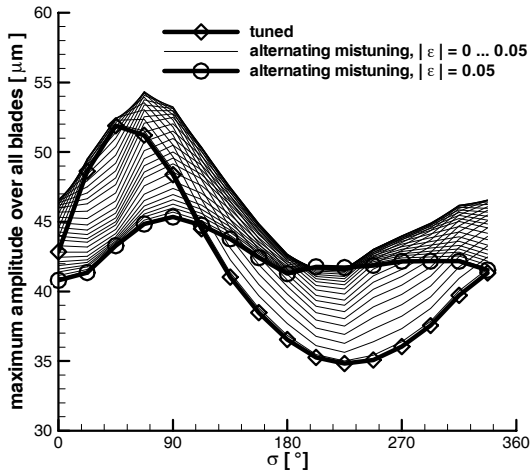


*Fig. 39: Tip trailing edge maximum response amplitude of the transonic compressor rotor 1T eigenmode, excitation interblade phase angle varied. Alternating frequency mistuning varied from ε = 0 to ε = ±0.05, maximum blade response shown.*

### 3.3.4 Modal coupling

While the previous examples of intentional mistuning were related to a single blade eigenmode only, the next case will deal with the forced response behaviour of a configuration where two blade eigenmodes have closely spaced eigenfrequencies. In analogy to section 3.2.6, it is assumed that the blade 1F generalised stiffness is raised considerably, so that the 1F eigenfrequency is of the same magnitude as the 1T eigenfrequency. The cascade is then subjected to a $4^{th}$ EO excitation in the same way as in the previous, single-mode examples. In Fig. 40, the resulting blade tip trailing edge amplitudes are shown for modal mistuning parameters of $\varepsilon_m = $ -0.06 to $\varepsilon_m = 0$ (top) and $\varepsilon_m = $ +0.01 to $\varepsilon_m = $ +0.06 (bottom). In this figure, the response amplitudes are plotted over the excitation frequency, so that the resonant peaks become apparent.

The layout is similar to Fig. 32. Note that in this case all blades of the cascade are identical, hence all blades also show identical response curves and only one curve for an arbitrary blade is shown here. For a modal mistuning parameter of $\varepsilon_m = $ -0.06, two distinct resonant peaks can be found in the corresponding response curve. The broader peak slightly to the right of the 1T in-vacuo eigenfrequency is associated to the 1T mode, the slightly lower and less broad peak at approximately 1430 Hz represents the 1F mode. In this case, the maximum response amplitude of 36 µm is virtually identical to the value of the tuned datum configuration. Note that the 1T resonant peak does not coincide exactly with the in-vacuo 1T eigenfrequency, which is due to the influence of the aerodynamic forces on the eigenvalues, as shown in Fig. 11. The differing width of the two resonant peaks points to the fact that the aerodynamic damping of the 1T mode is significantly higher than that of the 1F mode, as was shown in section 3.2.1.

Despite this difference in damping, the response amplitude for the 1F case is lower than that for the 1T case. The reason for this behaviour, which is also apparent in the datum configuration shown in Fig. 30, is that the 1T mode reacts more strongly to a $4^{th}$ EO excitation than the 1F mode does. In other words, the same $4^{th}$ EO incoming flow disturbance produces a higher generalised force on the 1T mode than on the 1F mode. If we now increase the modal mistuning parameter $\varepsilon_m$ towards zero, so that the two in-vacuo eigenfrequencies are increasingly close to each other, Fig. 40 (top) shows that the maximum response amplitude increases. Up to a value of $\varepsilon_m = $ -0.02, the increase in maximum amplitude remains moderate and the two resonant peaks remain clearly separated. Above values of $\varepsilon_m = $ -0.01, however, the increase in maximum amplitudes is drastic and the two resonant peaks begin to merge.
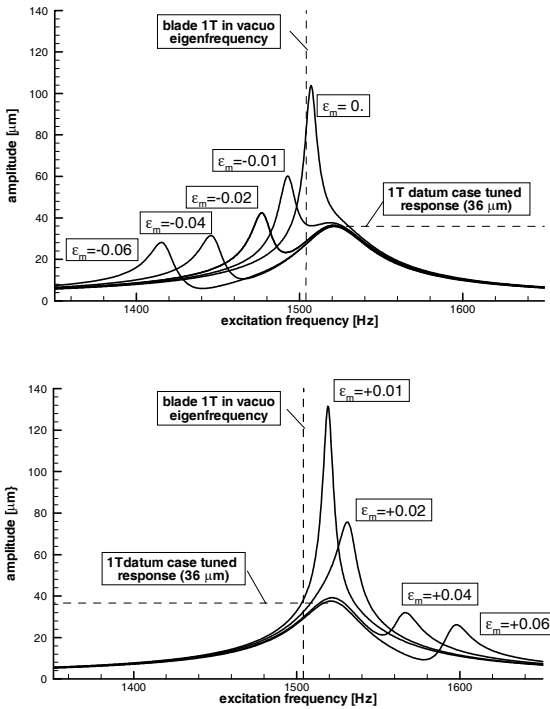
**Fig. 40: Tip trailing edge response amplitude the transonic compressor rotor blades under 4$^{th}$ EO excitation with modal coupling of the 1F and 1T modes. Dashed line shows 1T datum case tuned maximum response level for reference. Top: $\varepsilon_m$= -0.06 to $\varepsilon_m$= 0.0, bottom: $\varepsilon_m$= 0.01 to $\varepsilon_m$= +0.06.**

The highest response amplitudes are reached at a nodal mistuning parameter of $\varepsilon_m$ = +0.01 (Fig. 40, bottom), where only one single resonant peak can be found and maximum amplitudes of 133 µm are reached. This exceeds the datum case amplitudes by a factor of 3.7. For higher values of $\varepsilon_m$, the maximum response amplitudes begin to decay rapidly, while at the same time the response curves begin to show two distinct peaks again, until at $\varepsilon_m$ = +0.06, the situation is again very similar to the datum case and to the case of $\varepsilon_m$ = -0.06.

Changing the excitation engine order to 18$^{th}$ EO results in the response curves shown in Fig. 41. The behaviour of the blades is qualitatively very similar to that for the 4$^{th}$ EO excitation, but the highest response amplitude exceeds the datum case reference value only by a factor of approximately 2 in this case.
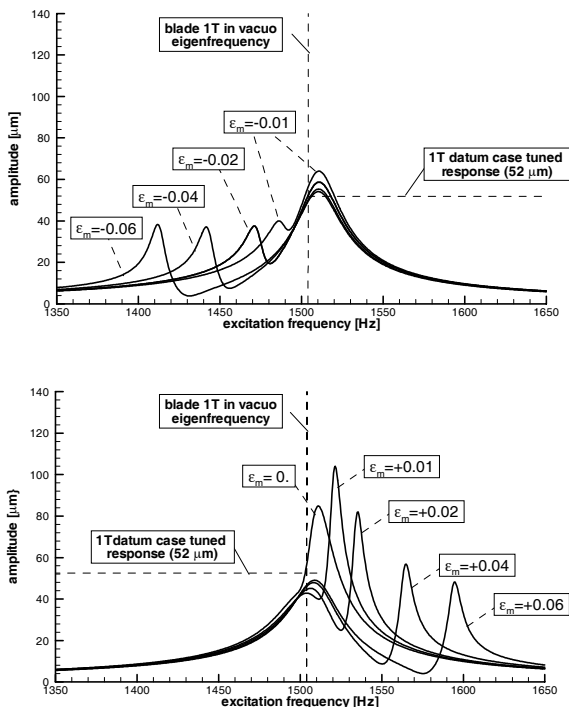
*Fig. 41: Tip trailing edge response amplitude the transonic compressor rotor blades under 18<sup>th</sup> EO*

*Fig. 41: Tip trailing edge response amplitude the transonic compressor rotor blades under 18th EO excitation with modal coupling of the 1F and 1T modes. Horizontal dashed line shows 1T datum case tuned rmaximum response level for reference. Top: $\varepsilon_m$= -0.06 to $\varepsilon_m$= -0.01, bottom: $\varepsilon_m$= 0.0 to $\varepsilon_m$= +0.06.*

The two examples shown demonstrate that the response amplitudes can significantly increase if the blade eigenfrequencies are closely spaced. To clarify the reasons for this behaviour, it is helpful to refer back to the findings of the eigenvalue analysis in section 3.2. In Fig. 28, the variation of the complete set of eigenvalues for the case of modal coupling is shown. Recall that in case of a cascade consisting of identical blades, as we have in the present example, the eigenvectors have a constant interblade phase angle. Consequently, the single engine order excitation applied in the present case will only excite the corresponding eigenvectors.

Furthermore, for the present case, where two blade eigenmodes are considered, two pairs of eigenvalue / eigenvector combinations will exist for each interblade phase angle.

To better understand the behaviour of the cascade for these cases, it is thus sufficient to inspect the variation of those eigenvalues that correspond to the eigenvectors with the same interblade phase angle as that of the excitation used.

In Fig. 42, these eigenvalues are shown. This figure is derived from Fig. 28, but it is restricted to those eigenvalues that correspond to the eigenvectors with $\sigma = 90°$ (4th EO) and $\sigma = 45°$ (18th EO). Furthermore, the abscissa is given in terms of frequency instead of $\eta_{\text{IT}}$, so that the reference to Fig. 40 and Fig. 41 is facilitated.
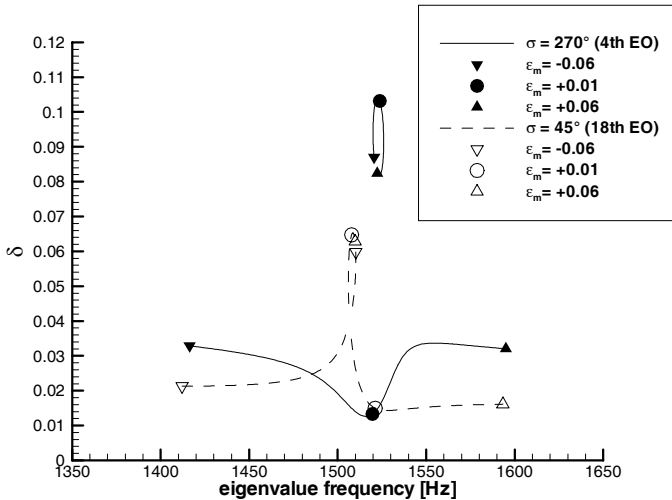


**Fig. 42: Eigenvalues of the transonic compressor rotor for the 1F in-vacuo eigenfrequency varying from $\varepsilon_m$= -0.06 to $\varepsilon_m$= +0.06. Only eigenvalues corresponding to $\sigma = 90°$ and $\sigma = 45°$ shown.**

In Fig. 42, the eigenvalues corresponding to the 4th EO are shown using solid lines and filled symbols, while the ones corresponding to the 18th EO are denoted by the dashed lines and hollow symbols. Furthermore, the gradient symbols identify the case of $\varepsilon_m$ = -0.06, the circles stand for $\varepsilon_m$ = +0.01 and the delta symbols denote $\varepsilon_m$=+0.06. The lines joining the symbols refer to the eigenvalue trajectories for a smooth variation of the modal mistuning parameter between the extremal values of $\varepsilon_m$ = -0.06 and $\varepsilon_m$ = +0.06. As discussed for Fig. 28, the eigenvalue trajectories starting at the lower left of the figure and ending at the lower right correspond to eigenvectors largely dominated by the 1F blade eigenmode, while the ones with smaller frequency variations and higher damping values at the centre of the plot correspond to eigenvectors with large components of the

1T eigenmode. However, in the region around $\varepsilon_m = 0$, most eigenvectors have significant components of both 1T and 1F eigenmodes, as discussed in section 3.2.6.

For the case of 4th EO excitation, the 1F-related eigenvalue in Fig. 42 shows a significant decrease in damping values with increasing values of $\varepsilon_m$, starting from approximately $\delta = 0.035$ and reaching a minimum of approximately $\delta = 0.01$ near $\varepsilon_m = +0.01$. At the same time, the 1T-related eigenvalue shows an increase in damping from approximately $\delta = 0.085$ to $\delta = 0.105$. Although the change in damping is comparable to that of the first eigenvalue, it is significantly less relevant because of much higher absolute level of the second eigenvalue damping. For the 18th EO case, similar observations can be made, although the 1F-related eigenvalue first rises in damping before dropping rapidly to its minimum value, again near $\varepsilon_m = +0.01$. In this case, the change in damping is less pronounced as in the 4th EO case. For both cases, it can be noted that a reduction in damping is observed in the situation where both blade eigenmodes are closely coupled. This partly explains the increased amplitudes under external excitation that are observed in Fig. 40 and Fig. 41. A second reason for the increased amplitudes can be found in the inter-mode influence coefficients that were shown in Fig. 9. These clearly show a large influence of the torsional motion on the bending forces, as was discussed in section 3.2.1. When the eigenfrequencies of both 1F and 1T modes coincide, the motion of the blades in the torsional eigenmode give rise to significant additional forces in the bending direction, which in turn increase the bending amplitude. Thus the amplitude at the coupled resonance condition will exceed the sum of the two uncoupled resonance peeks, as is observed in the examples shown.

These two effects – reduction of damping and increased forcing – explain the strong increase in amplitude when the modal mistuning parameter $\varepsilon_m$ is near zero.

### 3.3.5  Stochastic frequency mistuning

In the previous sections, the effects of intentional mistuning of single or multiple blades were studied. Introducing such a mistuning pattern can be used to achieve specific aeroelastic characteristics, as shown above. The blades of a real turbomachine will, however, also exhibit a certain amount of stochastic frequency variability, for example due to inevitable manufacturing tolerances or small variations in material properties.

The effect of these variations cannot be predicted exactly in most cases, since the precise eigenfrequency will usually not be measured for every manufactured item. Consequently, stochastic mistuning variations can only be assessed in a statistical manner, assuming a certain probability distribution of the blade eigenfrequencies and

examining a multitude of randomly chosen configurations ("Monte-Carlo-Method"). From these results, the maximum, minimum, and most probable response amplitudes can be deduced.

Assuming a uniform eigenfrequency probability distribution in the range of the tuned 1T eigenfrequency plus and minus 25% for the transonic compressor cascade, 500 sets of 16 blades were generated using a numerical random number generator. These 500 sets were then analysed for their response amplitudes for the whole range of excitation interblade phase angles from $\sigma = 0°$ to $\sigma = 360°$. Fig. 43 shows the resulting maximum amplitudes in the same format as in Fig. 39. Here, the amplitudes of the same configuration show no obvious correlation with the excitation interblade phase angle, consequently the lines between corresponding data points were omitted.
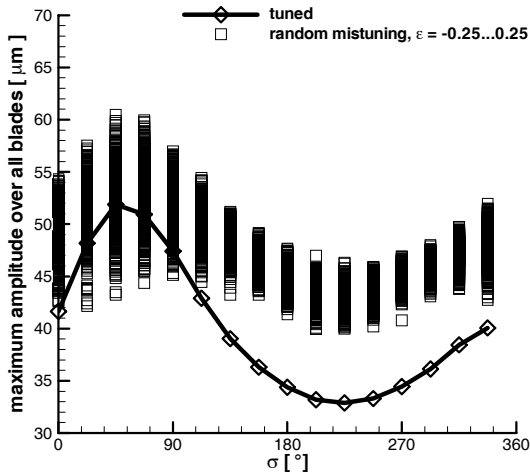


*Fig. 43: Tip trailing edge maximum response amplitude of the transonic compressor rotor 1T eigenmode, excitation interblade phase angle varied. 500 cases of random frequency mistuning with uniform mistuning probability from $\mathcal{E}= 0$ to $\mathcal{E}= ±0.25$, maximum blade response shown.*

The following observations can be made from this graph:

a) For excitation interblade phase angles larger than 90°, all randomly selected frequency distributions result in larger maximum amplitudes than those from the tuned configuration.

b) For excitation interblade phase angles in the range of $\sigma = 0°$ to $\sigma = 90°$, some configurations exist for which the resulting maximum amplitudes are lower than

for the tuned configuration. The majority of the configurations nevertheless yield higher amplitudes than in the tuned case.

c) The maximum amplitude of the worst mistuned case exceeds the tuned amplitude by more than 40%. The largest relative increase occurs for the excitation interblade phase angle with small tuned response amplitudes.

d) The spread of the resulting mistuned maximum amplitudes corresponds to the tuned amplitudes for each excitation interblade phase angle. It is small for the cases with small tuned amplitude and large for cases with large tuned amplitudes.

Given the fact that the actual configuration of the stochastic mistuning in a real machine cannot be controlled or predicted, it is obvious that the predictions from a tuned cascade model do not yield a conservative value for the resulting maximum amplitudes, but generally produce too low values.

In combination with the findings from the single blade and alternating mistuning, which indicate that the largest response amplitudes occur for configurations with small mistuning, it seems possible to use deliberate alternating mistuning as a means to control the maximum resonant amplitudes in such a cascade. This can be achieved by introducing a controlled alternating mistuning that significantly exceeds the uncontrollable stochastic mistuning that is inevitable due to the manufacturing tolerances. In this way, a situation is guaranteed in which adjacent blades in a cascade are largely decoupled, so that the large resonant amplitudes observed for small mistuning magnitudes cannot arise. Although the response amplitudes for the alternating mistuned configuration will in most cases still be larger than the tuned configuration values, they will in many cases be significantly smaller than the amplitudes of the worst possible single blade mistuning configurations.

### 3.3.6  Summary of section 3.3

The resonant response behaviour of the transonic compressor rotor under various types of frequency mistuning was studied in this section. For these, the influence of mistuning strength and excitation engine order (or, equivalently, interblade phase angle) were assessed. The key findings are given below.

For the case of a single mistuned blade:

- The blade exhibiting the maximum amplitude is either the mistuned blade itself or one of its immediate neighbours. This relates closely to the strength of the aerodynamic influence coefficients, which are large only for the eigen-influence and the influence on the immediate neighbours.

- Large positive and large negative mistuning strengths lead to very similar configurations, indicating that in these cases the mistuned blade is strongly decoupled from the rest of the cascade.
- Large variations of the response amplitudes are observed for mistuning strengths close to zero, the region corresponding approximately to the spread of the tuned mode eigenvalues. This is also where the highest absolute response amplitudes arise.
- The maximum amplitude over all blades always exceeds the tuned configuration value, regardless of excitation engine order and mistuning strength.

For the case of alternating mistuning:

- This type of mistuning is characterised by a very ordered structure, resulting in two sets of blades that are more or less decoupled.
- Contrary to the single blade mistuning, cases exist where the mistuned maximum amplitude is smaller than the tuned mode value. This is related to the convergence of the damping values towards a mean damping, as shown in section 3.2.3.
- Similar to the single blade mistuning configurations, the highest overall response amplitudes arise for the cases of small mistuning strength.

For modal coupling:

- When the structural eigenfrequencies of two modes are close to each other, significant coupling is observed. This can lead to a very large increase in the resonant amplitudes, exceeding the decoupled amplitudes by a factor of 3.7 in one of the examples studied. For such cases, a decoupled, individual analysis of the two modes, as used in the energy method approach, would lead to erroneous results.
- The large increase in resonant amplitudes for these cases can be traced to two sources, one being the decrease in aerodynamic damping in the closely coupled system, the other being the additional forcing supplied via the aerodynamic cross-coupling coefficients,

For stochastic mistuning

- Similar to the alternating mistuning case, some configurations exist where the mistuned maximum amplitude is below the tuned mode value. This behaviour is only observed for a small range of excitation interblade phase angles, where the tuned mode response is the highest.

- The majority of all configurations resulted in significantly increased maximum amplitudes, in some cases exceeding the tuned mode values by a factor of two.
- The spread of maximum amplitudes for different, randomly selected configurations seems to be related to the tuned mode response amplitude at the respective interblade phase angle, large tuned mode amplitudes resulting in a large spread of the mistuned maximum amplitudes.
- Since all real cascades will exhibit a certain random mistuning, tuned mode amplitude predictions will in most cases yield too low amplitude values. From the design perspective, the tuned mode approach is not conservative.
- Finally, alternating mistuning is identified as a means to control the maximum resonant amplitude of a stochastically mistuned configuration. Although the amplitude of the cascade with alternating mistuning will in most cases exceed the ones of the ideally tuned cascade, it will still be lower than the worst possible stochastically mistuned configuration. In this way, the unknown stochastically mistuned configuration is replaced by a controlled configuration with alternating mistuning.

## 4    Case study 2: HP turbine rig

### 4.1    Design parameters and steady flow conditions

This test case is a single stage turbine rig, representative of a modern high-pressure turbine stage. It was designed in the course of the IMT Area 3 turbine project [53]. The main geometric parameters are given in Table 2, a 3D view of the rotor and stator blading is shown in Fig. 44

| | |
|---|---|
| Number of vanes | 43 |
| Number of blades | 64 |
| Hub – to – tip ratio | 0.86 |
| Tip radius | 0.274 m |
| Stator Aspect ratio (inlet) | 0.71 |
| Rotor Aspect ratio | 1.07 |

*Table 2: Geometric parameters of the high pressure turbine stage.*

The rig was used as a cornerstone in various European research programs [41]. In the recently concluded ADTurB and in the currently running ADTurBII programme [26], the main emphasis is on aeroelastic effects. In the ADTurB programme, the excitation of the rotor due to the stator wakes was studied, with a special focus on the influence of mechanical mistuning of the rotor blades.
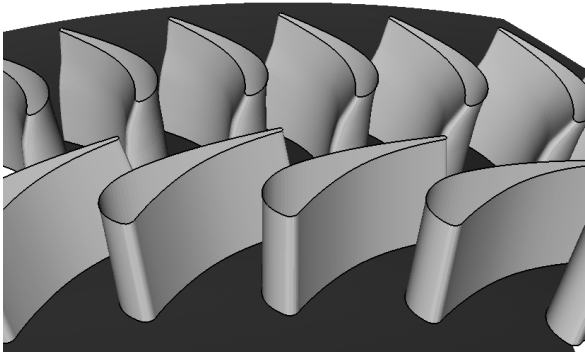


*Fig. 44: ADTurB stator and rotor blading 3D view, front looking aft.*

To evaluate the aeroelastic behaviour of the ADTurB rotor, the mechanical in-vacuo characteristics must be known first. Fig. 45 shows the Campbell diagram for this rotor, derived from a structural analysis of the blades using a commercial finite-element program. The diagram depicts the eigenfrequencies of the blades along with the excitation frequency due to the stator wakes, as a function of rotor speed. Note that due to data confidentiality, all values are non-dimensional and referenced to the calculated frequency of the 43rd EO / 1T resonant crossing. The main features of interest are the horizontal lines, characterising frequencies of the fundamental blade eigenmodes 1st bending (1F), 1st edgewise (1E), 1st torsion (1T), 1st chordwise and 2nd edgewise (2F). Along with these, the dashed lines indicate relevant engine order excitations. Apart from the low engine orders 1 to 5 that will always be present to a certain amount due to mechanical excitations (e.g. rotor imbalance), the main excitation is expected for the 43rd EO due to the wakes of the stator vanes immediately in front of the rotor.
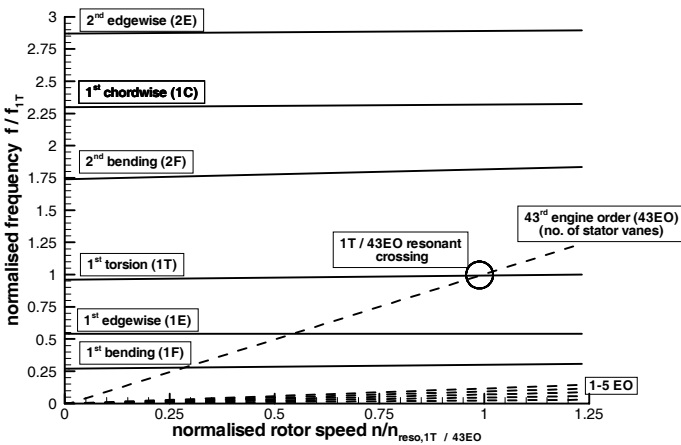


*Fig. 45: Campbell diagram of the ADTurB HP turbine rig rotor.*

The resonant crossing of the 43rd engine order with the 1st torsional eigenmode was studied experimentally in the ADTurB programme. The data gathered in this effort will be used in the following to validate the current method for forced response calculations under mistuned conditions.

The operating point of the test vehicle is slightly transonic with exit Mach numbers just exceeding unity in the stator as well as in the rotor. Fig. 46 shows the steady iso-Mach contours in the mid-span section of the stator and the rotor. The Mach numbers are given in the respective relative frame of reference, consequently being discontinuous at the stator-rotor interface.
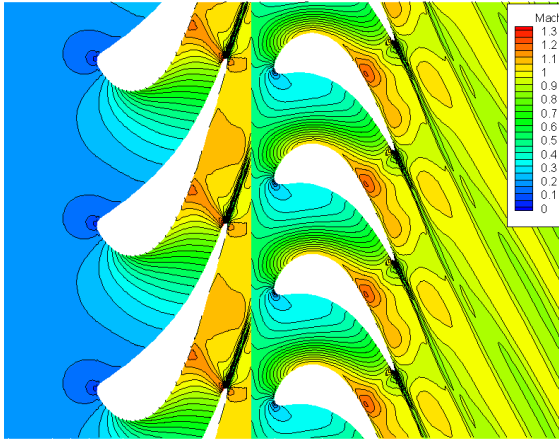


*Fig. 46: ADTurB stator and rotor mid-span section iso-Mach contours.*

For this operating point, the aerodynamic coefficients were computed for 36 interblade phase angles $\sigma$ with the airfoils oscillating in the 1T mode. The modeshape and frequency were taken from a standard FE calculation.

The rotor is situated at a small distance behind the stator vanes, so that the rotor blades periodically pass through the circumferentially inhomogeneous flow field due to the pressure field and the wakes generated by the stator vanes. The pressure field and the wakes, though stationary in the stator frame of reference, are experienced as unsteady disturbances in the rotor frame of reference, thus giving rise to unsteady aerodynamic forces on the rotor blades at a frequency equal to the rotational speed of the rotor times the number of stator vanes. To calculate the corresponding generalised forces for the 1T mode, an unsteady linearised Euler calculation was performed on the rotor. In this calculation, incoming disturbances are prescribed which correspond to the circumferential distribution of the steady flow field downstream of the stator, which was calculated using a turbulent, steady Navier-Stokes simulation of the isolated stator. This steady calculation was performed using the well-established and calibrated TRACE_S code [18].

The eigenfrequencies of all rotor blades were determined by experimental modal analysis with the blades clamped to a massive supporting root block device. It was found that most blades 1T eigenfrequencies clustered around a mean value to within +/- 1.5%, while seven blades exhibited significantly lower eigenfrequencies, deviating in excess of 5%. This large deviation was due to the fact that the blades were manufactured in different batches, which resulted in variations of the geometric tolerances and possibly in the properties of the raw material used. As a consequence of this finding, these seven blades were not included to calculate the mean frequency that is used in the following analysis. The resulting mistuning pattern is shown in Fig. 47, highlighting the severe mistuning of blades 5, 11, 17, 42 and 55 to 57.
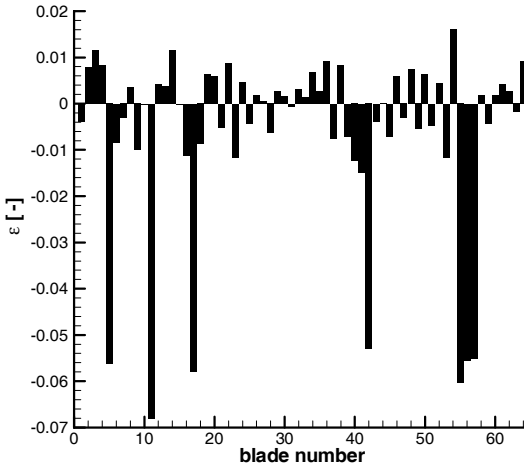


*Fig. 47: ADTurB rotor 1T mistuning pattern.*

In the rig experiment, the blades are mounted on a disc, which adds significantly more flexibility to the blade root than the clamping device of the modal analysis. Furthermore, the disc introduces mechanical coupling between the individual blades, quite in the same way as discussed for the transonic compressor rotor in the preceding chapter. To account for these effects, the generalised stiffness used in the analysis is assumed to be 11% lower than the value resulting from the FE calculation and a coupling stiffness of 0.9% between each two neighbouring blades is introduced into the system. These values were estimated after the experiments from the measured resonant frequencies.

Experimentally determined blade amplitudes are available for 23 of the 64 rotor blades. In Fig. 48, the measured amplitudes for blade 34 are shown as a typical example. The data is measured during a slow acceleration of the rotor through the 1T / 43rd EO resonance. The resulting unsteady signal is Fourier-transformed to be plotted in this figure in the manner of a Campbell diagram. The blue colour corresponds to a very low amplitude, the red regions correspond to high amplitudes. Note that the levels in between are spaced logarithmically. The rotor speeds as well as the response frequencies are non-dimensionalised using the same mean measured frequency that was used for the mistuning distribution above. Similarly, the response amplitudes have been normalised using the mean value of the measured peak amplitudes of all blades.
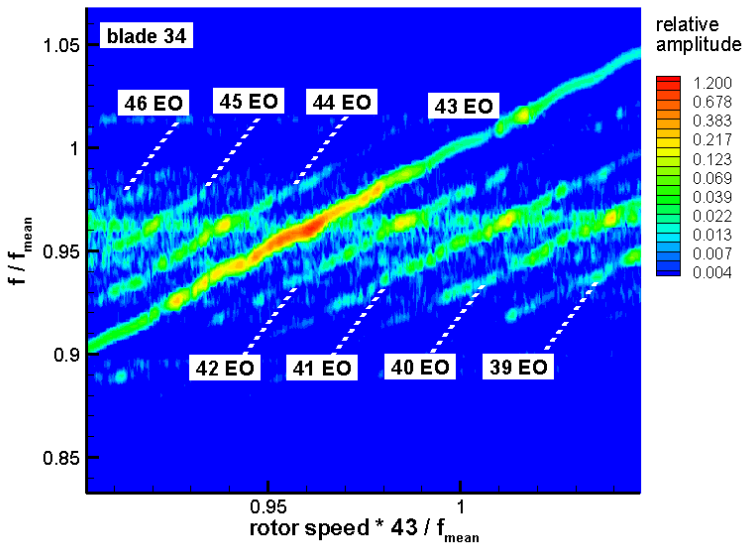


*Fig. 48: Fourier-transformed measured amplitudes on blade 34 for 1T / 43rd EO crossing.*

The horizontal green region at a non-dimensional frequency of approximately 0.96 corresponds to the 1T mode of blade 34. It can be found in the whole rotor speed range shown here. Remembering that the measured value of the blade 34 frequency from the experimental modal analysis was very close to the mean frequency, this observation confirms the aforementioned reduction of the eigenfrequencies due to the added flexibility in the disc.

The strong diagonal line rising with increasing rotor speed corresponds to the 43rd engine order excitation due to the stator wakes. Where the two lines of 1T mode and 43rd EO overlap, the highest response amplitudes are reached. Additionally, parallel, weaker engine order lines can be identified in the picture. These correspond to engine orders 40, 41, 42, 44 and 45. Even some small parts of the 39th EO and 46th EO lines can be found in this picture. Assuming that all the excitations seen here are resultant from aerodynamic effects, these sidebands can be identified as the effect of small imperfections in the periodicity of the stator pitch and stagger. These imperfections lead to the stator wakes arriving at the rotor blade not ideally periodic with a 43 per rev. periodicity, but with small phase differences. To quantify this effect, traces along the engine order lines of Fig. 48 have been performed. These amplitude traces are shown in Fig. 49 for engine orders 40 through 45.
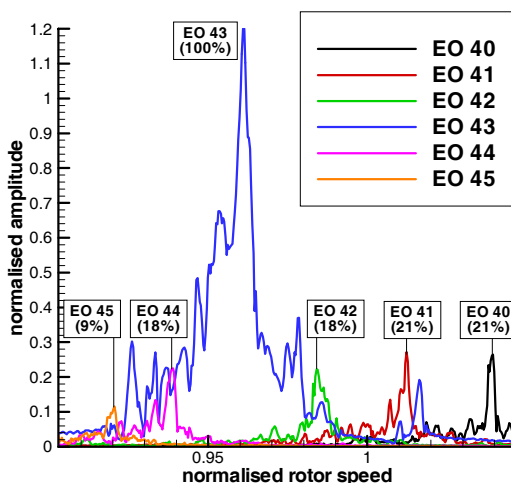


Fig. 49: Sideband intensity for ADTurB rotor blade 34 1T / 43rd EO resonance.

Four of the sidebands lead to a response on the order of 20% relative to the main 43rd EO resonance. This considerable sideband intensity can only be achieved if, at the same time, the intensity of the main engine order resonance is significantly reduced relative to an ideally periodic configuration. Using a simple estimation procedure (outlined in Appendix C), a 20% reduction of the 43rd EO intensity compared to the ideally periodic configuration is assumed. Since the previously discussed computational

values for the generalised forces on the rotor due to the stator interaction were derived under the assumption of such an ideally periodic configuration, the value of these generalised forces will be scaled by a factor of 0.8 accordingly for the following analysis.

## 4.2 Numerical analysis

The aeroelastic eigenvalues of the ADTurB rotor for the 1T / 43rd EO resonance operating conditions were determined analytically, comparing an ideally tuned configuration with the mistuned configuration according to the blade frequency measurements. In Fig. 50, the resulting eigenvalues are plotted for both configurations. The "x" symbols, denoting the tuned configuration, align into an orderly stability loop. The values of damping as well as those of the aeroelastic eigenfrequencies show fairly small variations, indicative of the rather small unsteady aerodynamic forces for this case. In the mistuned configuration, denoted by the "o" symbols, the spread of damping is even smaller, while the frequency spread is much larger, due to the significant frequency mistuning that was shown in Fig. 47. The mistuned eigenvalues seem to form three groups, at low, intermediate and high aeroelastic eigenfrequency values. Of each group, one typical representative was selected for closer inspection.
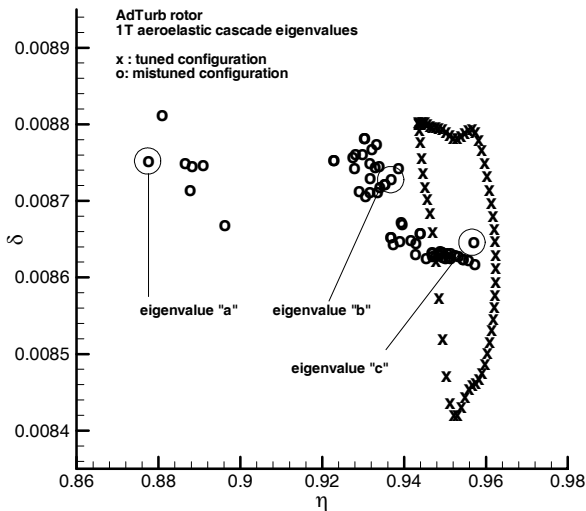


**Fig. 50: ADTurB rotor 1T aeroelastic cascade eigenvalues at 1T / 43rd EO resonance operating conditions, x: tuned configuration, o: mistuned configuration.**

In Fig. 51, the eigenvector localisation parameter $\psi$ is plotted for the mistuned configuration (in the tuned configuration, the eigenvectors are non-localised and the values of $\psi$ are zero). The values corresponding to the eigenvalues "a", "b" and "c" shown in Fig. 50 are marked accordingly.

It can be found that the localisation parameter varies in the range of $\psi \approx 0.6$ to $\psi \approx 0.95$. This implies that all eigenvectors are considerably localised, while some are close to the maximum value of $\psi = 1.0$, where only one blade participates in an eigenvector. This is confirmed by Fig. 52, where the amplitude distribution on all blades for eigenvectors "a", "b" and "c" is shown. Eigenvector "a", corresponding to an eigenvalue with very low aeroelastic eigenfrequency and a high localisation parameter, is almost entirely dominated by the contribution of blade 11, with small participation of its immediate neighbours, 10 and 12. Recall from Fig. 47 that blade 11 is one of the blades with extremely low frequencies. As such it is very strongly decoupled from the rest of the rotor blades, resulting in the high localisation of the eigenvector.
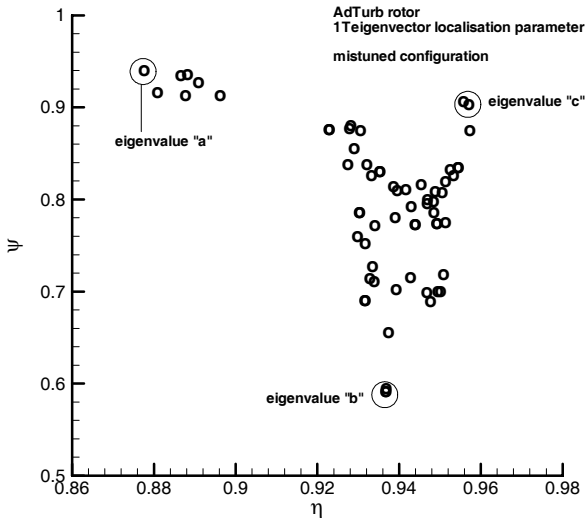


**Fig. 51: ADTurB rotor 1T aeroelastic cascade eigenvector localisation parameter at 1T / 43rd EO resonance operating conditions, mistuned configuration.**

In contrast to this, the eigenvector corresponding to eigenvalue "b", with moderate aeroelastic eigenfrequency and a comparably low localisation parameter of $\psi \approx 0.6$,

corresponds to an eigenvector where a large number of blades participate, with considerable amplitudes for a range of blades from number 23 through to number 50, where many blades feature very similar in-vacuo eigenfrequencies.

Finally, the eigenvector corresponding to eigenvalue "c", with high aeroelastic eigenfrequency and a localisation parameter almost as large as for eigenvalue "a", features an eigenvector that is very similar to the one for eigenvalue "a". This time, the dominant contribution is from blade 54, with some participation from blades 52, 53 and a very small component for blade 55. Checking with the mistuning pattern in Fig. 47 reveals that blade 54 is the one with the largest positive mistuning, explaining its strong decoupling from the rest of the cascade. Furthermore, its immediate neighbour, blade 55 displays a large negative mistuning parameter $\varepsilon$, so that its very small participation in this eigenvector is consistent.
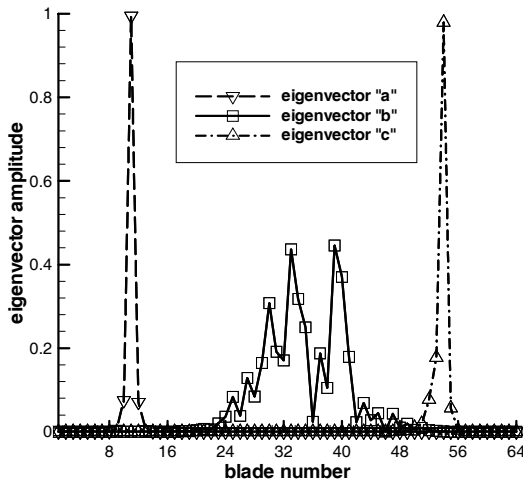


**Fig. 52: ADTurB rotor 1T aeroelastic cascade eigenvectors "a", "b" and "c" at 1T / 43$^{rd}$ EO resonance operating conditions, mistuned configuration.**

On the whole, these results indicate that the mistuned ADTurB rotor features only weak coupling between the individual blades, especially for the blades with large negative or positive values of the mistuning parameter. The resultant eigenvectors are strongly localised, with even the least localised ones showing contributions of blades spanning no more than one third of the rotor circumference.

## 4.3   Comparison of experimental and numerical response amplitude results

Using the values for the excitation forces determined from the sideband analysis shown above and sweeping the excitation frequency through the whole range of interest, the maximum response amplitudes of all blades were computed. A similar procedure was used in the experiment, where the variation of excitation frequency was achieved by speeding up the rotor. This was done sufficiently slowly, so that the influence of transient processes can be assumed to be small.

Fig. 53 shows the comparison of the resulting measured and computed maximum response amplitudes for all the blades that have experimental data available. The measured data for the various blades was taken from a number of different test runs, so that data from more than one run is available for a few of the blades. All the available data is included in this figure, so that the spread of the values for one blade, e.g. blade 32, gives an indication of the repeatability and measurement uncertainty of the experimental data. The figure indicates that the agreement between measured and computed data is quite acceptable. Not only is the mean response amplitude over the whole cascade matched well by the computation, but also the spread between the minimum and the maximum response of any blade is reproduced with good accuracy. Furthermore, in many instances the distribution of the amplitudes to the individual blades is shown by the computation in much the same manner as by the experiments.
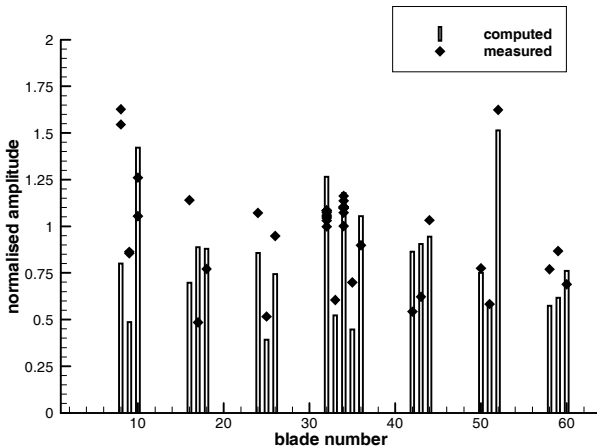


*Fig. 53: Comparison of computed and measured maximum ADTurB rotor 1T / 43rd EO blade amplitudes.*

Particularly, the amplitudes at blades number 24 to 26, 32 to 36 and 50 to 52 are extremely well met by the computation. Nevertheless, some of the other blades show larger differences between the measured and the computed values.

Recalling the particular mistuning pattern shown in Fig. 47, the question arises whether the resonant amplitude distribution is in any way correlated to the mistuning pattern. In Fig. 54, the measured and computed amplitudes are plotted over the individual mistuning parameter for each blade. In this case, the computational values are shown for all blades, not only the ones for which measured amplitude data is available. Both measured and computed data points appear as fairly widespread clusters. While the regions covered by the respective clusters agree well, no clear trend of amplitude with mistuning strength is apparent. Nevertheless, the limited amount of measured data available for this comparison does not lend itself to a definite assessment of this correlation.
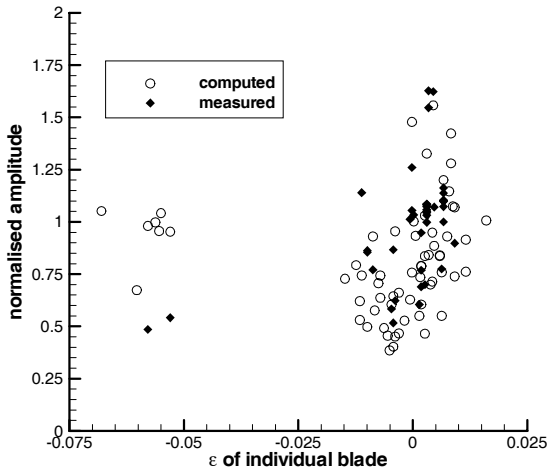


Fig. 54: Comparison of computed and measured maximum ADTurB rotor 1T / 43$^{rd}$ EO blade amplitudes, shown as a function of the individual blade mistuning, $\varepsilon$.

To further evaluate the ability of the current method to model the dominant effects of mistuning in this cascade, the amplitude distribution for the complete frequency sweep is compared to experimental values in Fig. 55. Here, the blades 32 to 36 are chosen for comparison, since the corresponding measured values on these blades were measured

simultaneously in a single run, making them particularly well suited for such a comparison. The dashed lines in Fig. 55 indicate the measured values, while the solid lines denote the computed results.
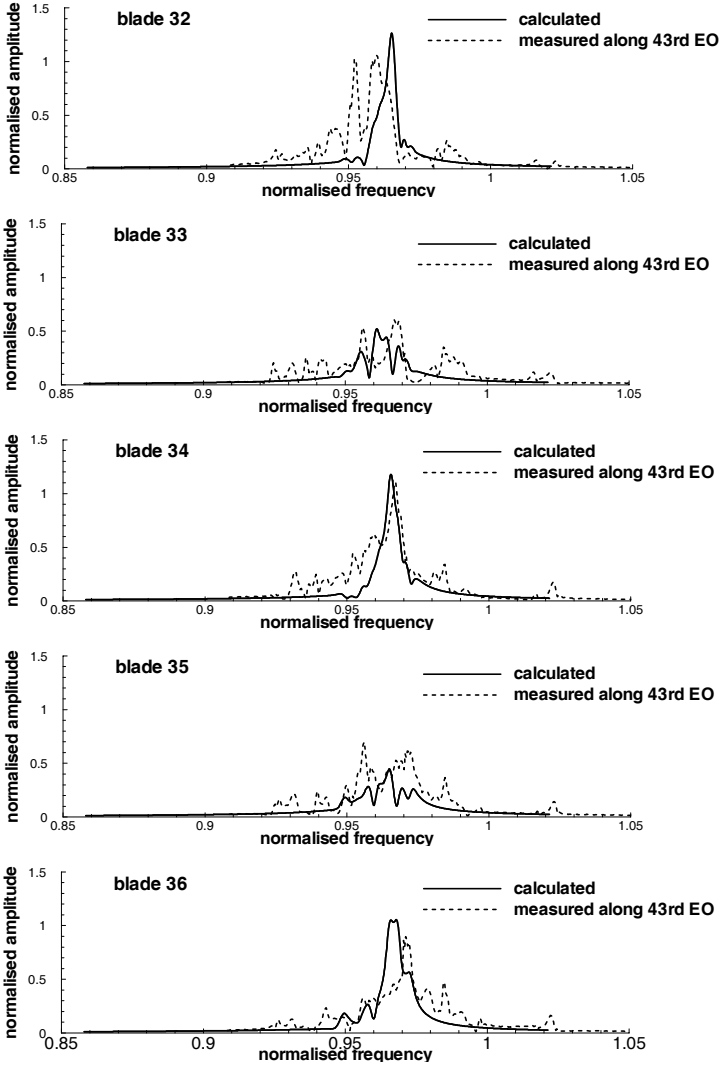


*Fig. 55: Comparison of computed and measured ADTurB rotor blade 32 to 36 response amplitudes.*

Comparing the different graphs again shows the good agreement between the computed and the measured maximum amplitudes. Furthermore, the frequency at which this maximum occurs is also well met by the computation. Nevertheless, some significant differences are also visible between the measured and the computed results. First, the computed distributions show much smoother curves than the measurements. It is not clear at this point if this behaviour can be attributed to stochastic effects in the experiment or if there are deterministic phenomena at work that are not modelled by the current method. Secondly, especially blade number 32 shows two distinct maxima of almost equal magnitude, a fact that is not captured by the computation.

Finally, all measured amplitudes show another, smaller peak at a normalised frequency of approximately 0.985, that is again not reproduced in the computation. In fact, closer inspection of this second maximum reveals that it is present at almost the same amplitudes on all the blades shown here. There seems to be no significant mistuning effect for this blade response. These observations point towards the presence of a system mode of the bladed disc at this frequency, which is not visibly changed by the differing torsional eigenfrequencies of the blades themselves. However, inspection of the FEM structural analysis results showed no indication of such a mode in this frequency range. From the current data, the nature of this second response maximum cannot be answered conclusively.

## 4.4 Effect of stochastic blade rearrangement

In the experimental set-up, only a single arrangement of the blades with their given individual mistuning on the rotor circumference could be studied. From these experiments alone, it is thus not possible to differentiate between the influence of individual blade mistuning and the influence of blade arrangement on the rotor. It remains unclear, whether the specific experimental configuration represents a typical case or – by mere chance – is a rare one with extraordinary high or low amplitudes. Furthermore, from the single configuration studied experimentally, it cannot be shown conclusively whether some correlation between resonant amplitude and mistuning strength exists. To acquire more information on these topics, a further analytical study was performed. Here, 1500 cases were studied, where for each of these the blades were randomly rearranged on the rotor. Each configuration was then analysed using the same procedure as described above for the experimental configuration. In Fig. 56, the resulting amplitude values are displayed. Here, the individual maximum blade

amplitudes are shown as an interval, where the maximum and minimum for each blade have been marked with the solid gradient and delta symbols, respectively. Note that the blade numbers given here refer to the blades themselves, not to the blade position on the rotor. Each blade number hence corresponds to a single mistuning strength $\varepsilon$. Further symbols shown in the figure are the solid squares, denoting the median of blade amplitudes for each blade (i.e. the configuration whose amplitude is larger than the lower half of the configurations and smaller than the other half), and finally the open diamonds, showing the computational results for the experimental configuration, as in Fig. 53. The figure clearly indicates that the relative positioning of the blades on the rotor has an enormous influence on the response amplitudes. For some blades, the maximum and minimum amplitudes are more than a factor of 5 apart.
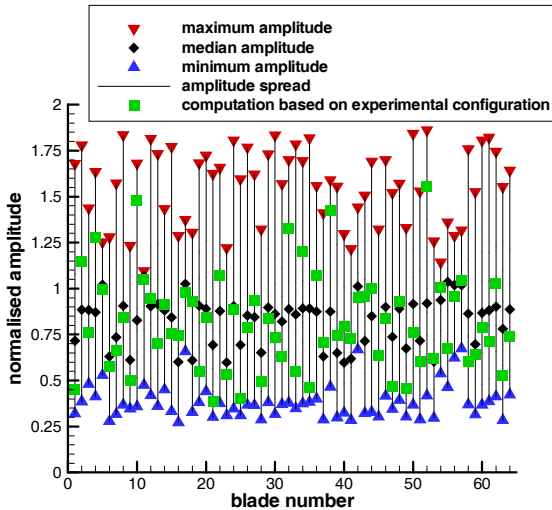


*Fig. 56: ADTurB rotor 1T / 43$^{rd}$ EO blade amplitudes of each blade for 1500 configurations of random rearrangement. Minimum, median, maximum and results of the computation based on the experimental configuration shown.*

Recall that these amplitude values correspond to the maximum measured values of a frequency sweep over the whole resonant frequency range. For practical purposes, this implies that a strain gauged blade on a test rotor might exhibit vibratory stresses that are well within the fatigue life limits, while another blade on the same rotor might experience vibration amplitudes five times higher at the same time. Then, after dismantling the rotor and rebuilding it with the same hardware, but with some blades at different positions, the

situation could be completely reversed with the instrumented blade now displaying the highest amplitudes.

The median values, representing the highest probability of the amplitudes, however, are restricted to a much smaller band, ranging from normalised amplitude values of 0.6 to 1.1, approximately. The values taken from the experimental configuration blend into the range given, covering most of the amplitude region. This leads to the conclusion that the experimental configuration is not exceptional in any way. Furthermore, the distribution of the median values close to normalised amplitudes of 1 indicates that the average of the experimentally observed amplitudes, which was taken as the reference value, is very representative of a typical configuration.

Arranging the same data points over the individual blade mistuning in the same manner as in Fig. 54 results in the graph shown in Fig. 57. Here a certain dependence of the minimum, maximum and median amplitude values on the blade mistuning is apparent. Obviously, the spread of minimum and maximum amplitudes is highest for small positive values of $\varepsilon$, while it is lower for large negative or positive $\varepsilon$. The median amplitudes are highest for the blades with large negative mistuning, then drop to significantly lower amplitudes for small negative values of $\varepsilon$ and rise again sharply with small positive $\varepsilon$.
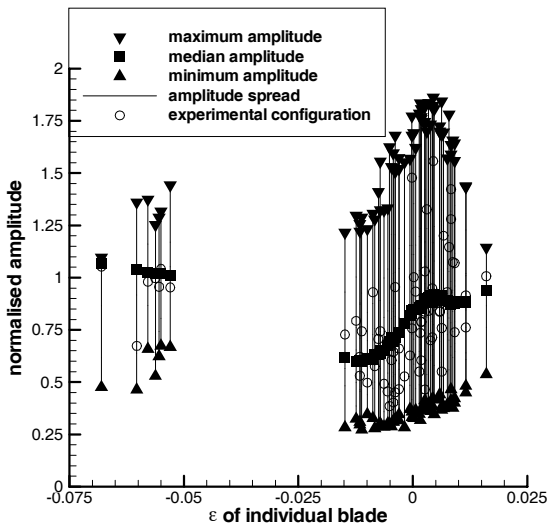


*Fig. 57: ADTurB rotor 1T / 43$^{rd}$ EO blade amplitudes of each blade for 1500 configurations of random rearrangement, plotted over individual blade mistuning $\varepsilon$. Minimum, median, maximum and results for the experimental configuration shown.*

## 4.5   Effect of stochastic blade frequency variation

While the previous section has demonstrated the strong influence of rearranging a given set of blades on the rotor, now the effect of stochastic mistuning on the individual blades will be evaluated. Similar to the previous study, 1500 configurations were studied, where each blade in each configuration was attributed a random frequency mistuning in the range of $\varepsilon$ = -0.08 to $\varepsilon$ = +0.08 with a constant probability for the whole frequency range. This range is larger than the spread of frequencies measured for the blades used in the experimental configuration.
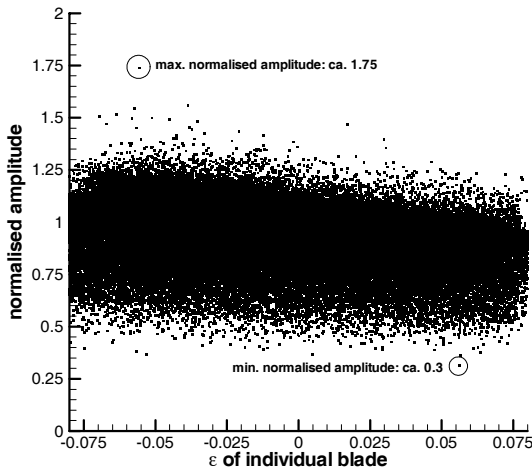


*Fig. 58: ADTurB rotor 1T / 43$^{rd}$ EO blade amplitudes of each blade for 1500 configurations of random frequency mistuning, $\varepsilon$ = -0.08 to $\varepsilon$ =+0.08.*

In Fig. 58, the resulting maximum amplitude for each blade in each configuration is shown as a single dot. Like in the case of random rearrangement, the amplitudes show a significant spread, ranging from normalised amplitudes of approximately 0.3 up to a single configuration exceeding the value of 1.75. A slight trend of decreasing amplitudes with increasing $\varepsilon$ is visible. This effect is mostly due to the increasing stiffness with increasing frequency (recall that the frequency mistuning is accomplished by changing the stiffness), which will lead to a similar behaviour already for a tuned system. Apart from this, no specific structure or even correlation between amplitude and $\varepsilon$ can be found in this picture.

## 4.6　Summary of chapter 4

In this section, the numerical procedure was validated against a high pressure turbine rig experiment.

The main findings are:

- The test case is characterised by large mistuning of the individual blades, leading to strong decoupling of the blades. The unsteady aerodynamic forces in this case are weak, the main interaction between the blades is accomplished by structural coupling in the disc.

- Apart from the dominant harmonic produced by the stator vane count, significant sideband harmonics can be identified in the measured data, indicating sideband intensity of up to 20% of the stator vane count harmonic.

- When correctly adjusting the single unknown parameter of structural blade coupling, the current method yields good agreement with the measured amplitudes. In particular:

    - The measured mean response amplitude of all blades in the rotor agrees very well with the mean computed value.

    - The spread between the highest and the lowest response blades is closely reproduced by the computation.

    - The individual blade response amplitudes agree very well for some blades, while for others, more or less large discrepancies between measurement and computation are apparent.

    - Where available, measured response behaviour over frequency was compared to the computational results. The agreement was found to be acceptable.

- The inspection of response over frequency measurements revealed a previously unidentified blade response frequency. It appears at the same frequency for all 5 blades examined here, indicating that it is not affected by the blade mistuning in the torsional mode. Since the FEM results indicate no additional modeshape at this frequency, the nature of this resonance remains open - possibly some geometric detail that was not modelled in the FEM is responsible for this lack of fidelity.

- The sensitivity of the response pattern to rearrangement of the blades on the rotor was studied using a stochastic variation. It was found that rearranging the same set of blades on the rotor has an overwhelming effect on the response

amplitudes, in some cases changing the response amplitude of an individual blade by a factor of more than five. The same variation implied a certain dependence of the median amplitudes and the amplitude spread on the mistuning strength for a given set of blades. However, the spread is in any case so large that no sensible correlation between response amplitude and mistuning strength can be given.

- Similarly, the influence of individual blade frequency mistuning on the response pattern was studied, again using a stochastic variation. Apart from the known dependence of a tuned system amplitude on the mean blade frequency, no apparent correlation between amplitude and mistuning was found. Again, the amplitude spread between the various configurations is very large, the difference between the minimum and the maximum amplitudes exceeding a factor of five.

## 5    Summary and conclusions

The main goal of the present study is to facilitate the inclusion of mistuning effects in the analysis of turbomachine blading aeroelastic behaviour. Although impressive results have been achieved by various researchers using direct simulation of large models with coupled, non linear aerodynamic and structural analysis methods, it was felt that this approach is neither well suited for studies to assess the importance or negligibility of certain parametric variations, nor is it currently usable for standard design procedures due to the enormous computational effort required for a single simulation.

Instead of using massive computational power, the approach chosen is to set up a reduced model of the cascade that retains the most important system characteristics in terms of the aerodynamic as well as the structural behaviour, while at the same time being sufficiently coarse to allow rapid studies of parametric variations or case studies using Monte Carlo methods.

Accordingly, the structural model of the cascade is reduced to a small number of degrees of freedom per individual blade, for which the amplitudes of the tuned blade eigenmodes are used. The variability between the individual blades is then introduced by changing the generalised mass, stiffness or damping quantities of the blade modes. If appropriate, disc effects can be introduced by an additional coupling stiffness between adjacent blades of the cascade. The aerodynamic coupling is modelled using the intra-mode and inter-mode aerodynamic influence coefficients that are currently calculated from tuned travelling wave linearised Euler calculations using a transformation procedure.

The resulting formulation is a compact system of equations in the form of a complex linear eigenvalue problem for analysis of the aeroelastic stability and in the form of a system of complex linear equations for the analysis of forced response problems. A central feature of this method is the inclusion of the aerodynamic damping and the aerodynamic coupling between the blades and between their individual eigenmodes, using the results of a modern 3D unsteady aerodynamic solver, which is applicable to configurations under subsonic as well as transonic flow conditions. The aerodynamic coefficients can be readily calculated for arbitrary eigenmodes of the blades. Furthermore, the change of aerodynamic coefficients with vibration frequency is taken into account when calculating the true aeroelastic eigenmodes and eigenfrequencies of

the tuned or mistuned cascades. Using this formulation, any blade specific changes in the generalised quantities mass, stiffness or damping can be varied individually and separately for each blade and each mode of vibration in the cascade, so that a very wide range of realistic configurations can be studies with relative ease and with moderate requirements for computational resources. These abilities discriminate the current method from previous works by other authors.

The methodology is applied to a detailed study of two realistic test cases taken from recently tested rig hardware, namely a transonic compressor rotor and a high pressure turbine rotor.

The investigation of the aeroelastic stability for the transonic compressor rotor concentrates on the two lowest eigenmodes, these are the first bending and first torsional mode. The speed of the method makes it possible to study not only a few cases of mistuning, but rather assess the transitioning of the aeroelastic system between extremal states with the continuous change in certain parameters. To facilitate the interpretation of the large amount of data generated by such studies, three parameters are defined: The mistuning parameter $\varepsilon$ characterises the amount of variation of the in-vacuo eigenfrequencies, the localisation parameter $\psi$ indicates how strongly a certain eigenvector is localised on one or a few blades of the cascade and the modal coupling parameter $\chi$ relates to the amount of coupling between different blade structural eigenmodes in a single cascade eigenvector.

The key findings with respect to the transonic compressor rotor are:

- For the tuned system, the eigenvalue analysis results are almost identical to those from the energy method, although the mass parameter is very low.
- The aerodynamic influence coefficients reveal a strong influence of the oscillating suction side on the pressure side of the neighbouring blade, while the reverse effect is much smaller.
- Any kind of mistuning, either single blade, alternating, or random, frequency or damping mistuning, reduces the coupling of the blades in the cascade. The overall behaviour of the cascade shows a trend towards the case of fully decoupled blades with increasing mistuning strength.
- Strong coupling leads to a wide spread of the eigenvalue damping, while decoupling results in a convergence of the damping values to the mean of the tuned case.

- A similar behaviour can be found in the cascade when the frequency split between adjacent blade modes is varied. If the frequencies are spaced far apart, the coupling between the modes is negligible, both modes form separate clusters of eigenvalues. When the frequencies are situated close together, a coupled system with a widely spread single cluster of eigenvalues results. This is also confirmed by the nature of the cascade eigenvectors, which in this case display strong participations from both blade modes.
- The forced response behaviour of the mistuned cascade is found to be closely linked to the eigenvalue distribution, as could be expected. For the case of single blade mistuning, the major deviations from the tuned response are limited to the mistuned blade and its immediate neighbours. Dependent on the mistuning strength and on the excitation engine order, the maximum resonant amplitude can arise on the mistuned blade or on one of its neighbours.
- In the case of single blade mistuning, the maximum amplitude over the whole cascade will exceed the tuned system response in any case.
- For alternating mistuning, a small range of parameters exists where the response of the mistuned system remains below the tuned system. This is again linked to the cascade decoupling, which leads to an increase in damping for some cases.
- If two structural eigenfrequencies are closely spaced, strong modal coupling can be observed. The resulting large increase in the resonant amplitudes can be traced to the decrease in aerodynamic damping and to the additional forcing supplied via the aerodynamic cross-coupling coefficients.
- For stochastic mistuning, a limited number of cases with reduced resonant amplitudes was observed, similar to what was found for the alternating mistuning study. However, the majority of cases resulted in a significant increase in response amplitude.
- If moderate stochastic mistuning is unavoidable, deliberate alternating mistuning of significant magnitude is identified as a possible means of controlling the maximum resonant amplitudes.

For the HP turbine rig rotor, detailed experimental data is available. The analysis and the comparison with the measured values lead to the following key points:

- The agreement between the measured and the analytical results is generally good. While the mean amplitude and the spread are reproduced very well by the analysis, not all measured blade amplitudes are closely met by the computed results. In the individual blade amplitude over frequency responses, certain

features are identified that are obviously beyond the fidelity of the structural analysis used as the basis of the present study.

- Analytical variations of blade positioning and of the individual blade eigenfrequencies revealed a very strong dependence of the resulting amplitudes on these parameters. Changes in resonant amplitudes by a factor of five are observed when merely changing the arrangement of a certain set of blades on the disc.

- No parametric dependence of the individual response amplitudes on the mistuning strength is apparent for this test case. However, for the rearrangement of the given experimental frequency distribution, a certain dependence of the amplitude spread and of the median amplitude values on the individual mistuning strength is found. Consistent with previous findings, the amplitude spread is largest for the blades with small mistuning strengths.

Finally, the following general conclusions can be drawn:

- The newly developed method is capable to assess the dominant effects of mistuning and coupling in turbomachinery cascades, including the mechanical and aerodynamic coupling of multiple modes with arbitrarily complex modeshapes. In this method, the aerodynamic characteristics of the cascade are accurately represented using the generalised unsteady aerodynamic coefficients derived from a modern three-dimensional flow solver, applicable to both sub- and transonic configurations.

- The simplifications employed significantly contribute to the computational efficiency of the method, making it applicable for design purposes as well as for the assessment of large parametric variations or for statistical studies of stochastically mistuned configurations.

- The current method is successfully validated by a comparison of numerical to experimental data. The applicability and accuracy is demonstrated by the favourable agreement between measured and computed results.

- Based on these validations, the method is applied to study the influence of major parameters on the aeroelastic behaviour of the selected test cases. The results show a wide range of phenomena, dependent on the type and strength of mistuning, frequency, modeshape and interblade phase angle. The results highlight the close inter-dependence of the aeroelastic stability derived from the eigenvalue analysis and the resonant amplitudes derived from the forced response analysis.

## 6  <u>Literature</u>

[1]    Afolabi, D.: The Frequency Response of Mistuned Bladed Disk Assemblies, *in: Kielb, R.E. (ed.): Vibrations of Blades and Bladed Disk Assemblies,* pp. 15-22, ASME, 1985.

[2]    Afolabi, D.: The Eigenvalue Spectrum of a Mistuned Bladed Disk, *in: Kielb, R.E. (ed.): Vibrations of Blades and Bladed Disk Assemblies,* pp. 23-30, ASME, 1985.

[3]    Bendiksen, O.O.: Flutter of Mistuned Turbomachinery Rotors, *Trans. ASME J. Eng. Gas Turbines and Power,* Vol. 106, pp. 25-33, Jan. 1984.

[4]    Bladh, R.; Castanier, R.; Pierre, C.: Reduced Order Modelling and Vibration Analysis of Mistuned Bladed Disk Assemblies with Shrouds, *Journal of engineering for Gas Turbines and Power,* Vol. 121, pp. 515-522, 1999.

[5]    Bladh, R.; Castanier, M.P.; Pierre, C.: Component-Mode-Based Reduced Order Modeling Techniques for Mistuned Bladed Disks, Part I: Theoretical Models, *ASME 2000-GT-0360, May 2000.*

[6]    Bladh, R.; Castanier, M.P.; Pierre, C. Component-Mode-Based Reduced Order Modeling Techniques for Mistuned Bladed Disks, Part II: Application, *ASME 2000-GT-0361, May 2000.*

[7]    Blaha, C.; Kablitz, S.; Hennecke, D.K.; Schmidt-Eisenlohr, U.; Pirker, K.; Haselhoff, S.: Numerical Investigation of the Flow in an Aft-Swept Transonic Compressor Rotor, *ASME-GT-0490,* May 2000.

[8]    Bölcs, A.; Fransson, T.H.: Aeroelasticity in Turbomachines: Comparison of theoretical and Experimental Cascade Results, *Communication du Laboratiore de Thermique Apliquée et de Turbomachines,* No. 13, Ecole Polytechnique Fédérale de Lausanne, 1986.

[9]    Brouillet, B.: *Zeitgenaue dreidimensionale Simulation des Flatterns in Turbomaschinen durch numerische Lösung der Navier-Stokes-Gleichungen,* Shaker Verlag, Aachen, 2001.

[10]  Campobasso, M.S.; Giles, M.B.: Flutter and Forced Response of Mistuned Turbomachinery, Oxford University Computing Laboratory, *Numerical Analysis Group Report No. 00/20*, Oct. 2000.

[11]  Carta, F.O.: Coupled Blade-Disk-Shroud Flutter Instabilities in Turbojet Engine Rotors, *Journal of Engineering for Power,* pp. 419-426, July 1967.

[12]  Chew, J.W.; Marshall, J.G.; Vahdati, M.; Imregun, M.: Part-Speed Flutter Analysis of a Wide Chord Fan Blade, in: *Fransson, T.H. (ed): Unsteady Aerodynamics and Aeroelasticity of Turbomachines,* pp. 707-724, Kluver Academic Publishers, 1998.

[13]  Choi, B.-K.; Lentz, J.; Rivas-Guerra, A.; Mignolet, M.: Optimization of Intentional Mistuning Patterns for the Reduction of the Forced Response Effects of Unintentional Mistuning: Formulation and Assessment, *ASME-2001-GT-0293,* 2001.

[14]  Collar, A.R.: The Expanding Domain of Aeroelasticity, *Journal of the Royal Aeronautic Society,* Vol. 50, pp. 613.636, Aug. 1946.

[15]  Craig, R.R.; Bampton, M.C.C.: Coupling of Substructures for Dynamic Analyses, *AIAA Journal,* Vol. 6, pp. 1313-1319, 1968.

[16]  Crawley, E.F.: Aeroelastic Formulation for Tuned and Mistuned Rotors, in: *Platzer, M.; Carta, F.O. (eds): AGARD Manual on Aeroelasticity in Axial-Flow Turbomachines, Vol.2: Structural Dynamics and Aeroelasticity, AGARD-AG-298 Vol. 2*, pp. 19-1 – 19-24, Jun. 1988.

[17]  Ewins, D.J.: Structural Dynamic Characteristics of Bladed Assemblies, in: *Platzer, M.; Carta, F.O. (eds): AGARD Manual on Aeroelasticity in Axial-Flow Turbomachines, Vol.2: Structural Dynamics and Aeroelasticity, AGARD-AG-298 Vol. 2,* pp. 15-1 – 15-37, Jun. 1988.

[18]  Fritsch, G., Hoeger, M., Blaha, C. and Bauer, D.: Viscous 3D Compressor Simulations in Parallel Architectures – Design Tool Development and Application to a Transonic Compressor Stage. *AIAA-paper 97-2876,* 1997.

[19]  Gerolymos, G.A.: Periodicity, Superposition and 3D Effects in Supersonic Compressor Flutter Aerodynamics, *International Journal of Turbo and Jet Engines, 7,* pp. 143-152, 1990.

[20] Giles, M.B.: Non-Reflecting Boundary Conditions for the Euler Equations, *Computational Fluid Dynamics Laboratory Report CFDL-TR-86-6,* Massachusetts Institute of Technology, 1986.

[21] Giles, M.B.: Calculation of Unsteady Wake Rotor Interaction, *AIAA Journal of Propulsion and Power,* Vol.4, No. 4, pp. 365-362, 1988.

[22] Hall, K.C; Crawley, E.F.: A Linearised Euler Analysis of Unsteady Flows in Turbomachinery, *NASA-CR-180987,* Massachusetts Institute of Technology, Jun. 1987.

[23] Hall, K.C.; Lorence, C.B.: Calculation of Three-Dimensional Unsteady Flows in Turbomachinery Using the Time Linearized Euler Equations, *ASME 92-GT-136,* 1992.

[24] Happel, H.W.; Stubert, B.: Computation of 3D Cascade Flows and Comparison with Experiments, *AGARD-CP-437,* pp. 31-1 – 31-11, 1988.

[25] He, L.: An Euler Solution for Unsteady Flows Around Oscillating Blades, *ASME Journal of Turbomachinery,* Vol. 112, pp. 714-722, 1990.

[26] Hennings, H.; Elliot, R.: Forced Response Experiments in a High Pressure Turbine Stage, *ASME-GT-2002-30453,* 2002.

[27] Holmes, D.G.; Chuang, H.A.: 2D Linearized Euler flow analysis for Flutter and Forced Response, in *Atassi, H.M. (ed): Unsteady Aerodynamics, Aeroacoustics and Aeroelasticity of Turbomachines,* Springer-Verlag, New York, 1993.

[28] Holmes, D.G.; Lorence, C.B.: Three Dimensional Linearized Navier-Stokes Calculations for Flutter and Forced Response, in: *Fransson, T.H. (ed): Unsteady Aerodynamics and Aeroelasticity of Turbomachines,* pp. 211-224, Kluver Academic Publishers, 1998.

[29] Hüttl, T.; Kahl, G.; Kennepohl, F.; Heinig, K.: Resolution Requirements for the Numerical Computation of Tonal Noise in Compressors and Turbines of Aeroengines, *NATO RTO/AVT Symposium on Aging Mechanisms and Control, Part A: Development in Computational Aero- and Hydro-Acoustics,* Manchester, UK, Oct. 8-11, 2001.

[30] Jeffers, J.D.; Meece, C.E., Jr.: F100 Fan Stall Flutter Problem Review and Solution, *Journal of Aircraft,* Vol. 12, pp. 324-332, Apr. 1975.

[31] Judge, J.; Pierre, C.: Experimental Investigation of Mode Localization and Forced Response Amplitude Magnification for a Mistuned Bladed Disk, *ASME 2000-GT-0358,* May 2000.

[32] Kahl, G.; Klose, A.: Computation of Time Linearized Transonic Flow in Oscillating Cascades, *ASME 92-GT-296,* 1993.

[33] Kahl, G.: Application of a Time Linearized Euler Solver to Aeroelastic Problems in Turbomachinery, *ASME 95-GT-123,* 1995.

[34] Kahl, G.: Abschlußbericht HTGT – Turbotech, Arbeitspaket Nr. 1.1.3.3, Berechnung der instationären, transsonischen, dreidimensionalen Strömung durch schwingende Schaufelgitter unter der Annahme kleiner Schwingungsamplituden. MTU München, Technischer Bericht *MTUM-B95EW-0011,* 1995.

[35] Kahl, G.: Structural Mistuning and Aerodynamic Coupling in turbomachinery Bladings, in: *Fransson, T.H. (ed): Unsteady Aerodynamics and Aeroelasticity of Turbomachines,* pp. 335-346, Kluver Academic Publishers, 1998.

[36] Kahl, G.; Hennings, H.: Computational Investigation of an Oscillating Compressor Cascade Experiment, *9. ISUAAAT conference,* Lyon, Sept. 4.-9. 2000.

[37] Kennepohl, F.; Kahl, G.; Heinig, K.: Turbine Blade / Vane Interaction Noise: Calculation with a 3D Time-Linearised Euler Method, *AIAA-2001-2152,* 2001.

[38] Kielb, R.E.; Kaza, K.R.V: Aeroelastic Characteristics of a Cascade of Mistuned Blades in Subsonic and Supersonic Flow, *Trans. ASME J. Vibration, Acoustics Stress and Reliability in Design,* Vol. 105, pp. 425-433, Oct. 1983.

[39] Kielb, R.E.; Kaza, K.R.V.: Effects of Structural Coupling on Mistuned Cascade Flutter and Response, *Trans. ASME J. Eng. Gas Turbines and Power,* Vol. 106, pp. 17-24, Jan. 1984.

[40] Kielb, R.E.: *Introduction to Aeroelastic Blade Design,* A Three Day Intensive Course during the 8th International Symposium on Unsteady Aerodynamics and Aeroelasticity in Turbomachines, Stockholm, Sweden, Sept. 11-13, 1997.

[41] Kost, F.; Hummel, F.; Tiedemann, T.: Investigation of the Unsteady Rotor Flow Field in a Single Stage HP Turbine Stage, *ASME-2000-GT-432,* 2000.

[42] Lane, F.: System Mode Shapes in the Flutter of Compressor Blade Rows, *Journal of the Aeronautical Sciences,* Vol. 23, No. 1, pp. 54-66, 1956.

[43] Moyroud, F.; Fransson, T.; Jaquet-Richardet, G.: A Comparison of Two Finite Element Reduction Techniques for Mistuned Blades, *ASME-2000-GT-0362,* 2000.

[44] Namba, M.: Three-Dimensional Flows, in *Platzer, M.F. (ed.): AGARD Manual on Aeroelasticity, AGARD-AG-298, Vol. 1,* Ch. 4, 1987.

[45] Ni, R.H.: *Non-Stationary Aerodynamics of Arbitrary Cascades in compressible Flow,* Stevens Institute of Technology, Jun. 1974.

[46] Nixon, D.: Computation of Unsteady Transonic Cascade Flows", *AIAA Journal,* Vol. 21, No. 5, pp. 780-792, 1982.

[47] Ott, P.: Oszillierender Senkrechter Verdichtungsstoss in einer ebenen Düse, *Communication du Laboratoire de Thermique Apliquée et de Turbomachines de l'École Polytechnique Fédérale de Lausanne*, No. 18, 1992.

[48] Petrov, E.P.; Ewins, D.J.: Analysis of the Worst Mistuning Patterns in Bladed Disc Assemblies, *ASME-2001-GT-0292,* 2001.

[49] Pierre, C.; Murthy, D.V.: Aeroelastic Modal Characteristics of Mistuned Blade Assemblies: Mode Localization and Loss of Eigenstructure. *AIAA Journal,* Vol. 30, No. 10, pp. 2483-2496, 1992.

[50] Pierre, C. et al: Localization of Aeroelastic Modes in Mistuned High-Energy Turbines, *J. of Propulsion and Power,* Vol. 10, No. 3., pp. 318-328, 1994.

[51] Reddy, T.S.R; Bakhle, M.A.; Srivastava, R.; Mehmed, O.; Stefko, G.L.: A Review of Recent Aeroelastic Methods for Propulsion at NASA Lewis Research Center, *NASA-TP-3406,* 1993.

[52] Rivas-Guerra, A.; Mignolet, M.: Local / Global Effects of Mistuning in the Forced Response of Bladed Disks, *ASME-2001-GT-0289,* 2001.

[53]  Seinturier, E. et al.: A New Method to Predict Flutter in Presence of Structural Mistuning. Application to a Wide Chord Fan Stage, *9. ISUAAAT conference,* Lyon, Sept. 4.-9. 2000.

[54]  Seinturier, E.; Lombard, J.-P.; Berthillier, M.; Sgarzi, O.: Numerical Method for Mistuned Bladed Disk Forced Response, *to be presented at ASME Turbo Expo 2002,* Amsterdam, The Netherlands, Jun. 3.-6. 2002.

[55]  Santoriello, G.; Colella, A.; Colantuoni, S.: Rotor Blade Aerodynamic Design, Alfa Romeo Avio, IMT Area 3 turbine project technical report, *AER2-CT92-0044,* 1993.

[56]  Smith, S.N.: Discrete Frequency Sound Generation in Axial Flow Turbomachinery, *Aeronautical Research Council, R&M 3709,* 1973.

[57]  Srinivasan, A.V.; Fabunmo, J.A.: Cascade Flutter Analysis of Cantilevered Blades, *Trans. ASME J. Eng. Gas Turbines and Power*, Vol. 105, pp. 34-43, Jan. 1984.

[58]  Srinivasan, A.V.; Tavares, G.G.: Direct Use of Unsteady Aerodynamic Pressures in the Flutter Analysis on Mistuned Blades, *ASME 94-GT-347*, 1994.

[59]  Verdon, J.M.: A Linear Aerodynamic Analysis for Unsteady Transonic Cascades, *NASA-CR-3833*, 1984.

[60]  Verdon, J.M.: The Unsteady Aerodynamic Response to Arbitrary Modes of Blade Motion, *Journal of Fluids and Structures,* Vol. 3, No. 3, pp. 255.274, 1989.

[61]  Whitehead, D.S.: Force and Moment Coefficients for Vibrationg Airfoils in Cascades, *Aeronautical Research Council, R&M 3254*, Feb. 1960.

[62]  Whitehead, D.S.: Cambridge University Engineering Department Report *CUED/A Turbo/TR 118*, 1982.

[63]  Yang, M.-T.; Griffin, J.: A Reduced Order Model of Mistuning Using a Subset of Nominal System Modes, *ASME 99-GT-288,* 1999.

[64]  Yoon, S.: A Navier-Stokes Solver Using the LU-SSOR TVD Algorithm, *NASA-CR-179608,* Sverdrup Technology Inc. / NASA Lewis Research Center, Mar. 1987.

# 7 <u>List of symbols</u>

## 7.1 Latin

| Symbol | unit | description |
| --- | --- | --- |
| $\vec{a}$ | - | vector of modal amplitudes |
| $\vec{A}$ | m | surface normal vector |
| **A,B,C,D** | various | Jacobian matrices in the linearised Euler solver |
| c | m / s | absolute velocity |
| **C** | kg m$^2$ / s$^2$ | Aerodynamic coupling matrix |
| d | kg m$^2$ / s | modal damping |
| **D** | kg m$^2$ / s | Damping matrix |
| *DOF* | - | number of degrees of freedom |
| $e_{rot}$ | kJ / kg | internal energy |
| **E** | - | unit matrix |
| **F** | various | flux vector |
| f | Hz | frequency |
| $\vec{F}$ | Nm | External generalised forces |
| $i$ | - | imaginary unit, $\sqrt{-1}$ |
| k | kg m$^2$ / s$^2$ | modal stiffness |
| $k, l$ | - | blade number indices |
| **K** | kg m$^2$ / s$^2$ | stiffness matrix |
| m | kg m$^2$ | modal mass |
| $n_{rot}$ | 1 / min | rotational speed |
| **M** | kg m$^2$ | mass matrix |
| $\vec{n}$ | m | unit surface outward normal vector |
| ND | - | nodal diameter |
| p | Pa | pressure |
| r | m | radial coordinate |
| S | m$^2$ | surface |
| t | s | time |
| w | m / s | relative velocity |
| $\vec{w}$ | m / s | relative flow vector |
| V | m$^3$ | volume |
| $\vec{x}$ | m | position vector |
| z | m | axial coordinate |

## 7.2   Greek

| | | |
|---|---|---|
| $\alpha$ | - | artificial dissipation scaling factor |
| $\gamma$ | 1 / s | decay constant |
| $\delta$ | - | logarithmic decrement |
| $\varepsilon$ | - | mistuning magnitude $\varepsilon = \omega / \omega_0 - 1$ |
| $\zeta$ | 1 / s$^2$ | transformed eigenvalue, $\zeta = (\lambda - i\,d\,/\,2m)^2$ |
| $\zeta$ | - | artificial dissipation parameter |
| $\eta$ | - | frequency ratio $\eta = f / f_0$ |
| $\lambda$ | 1 / s | eigenvalue, $\lambda = \omega + i\gamma$ |
| $\xi$ | - | coupling stiffness ratio, $\xi = k_c / k$ |
| $\rho$ | kg / m$^3$ | density |
| $\sigma$ | ° | inter-blade phase angle |
| $\phi$ | ° | circumferential coordinate |
| $\vec{\Phi}$ | m | blade structural eigenvector |
| $\chi$ | - | modal coupling parameter |
| $\psi$ | - | localisation parameter |
| $\omega$ | 1 / s | angular frequency of oscillation, $\omega = 2\pi f$ |
| $\Omega$ | 1 / s | angular frequency of rotation, $\Omega = 2\pi n_{rot} / 60$ |

## 7.3   Superscripts

| | |
|---|---|
| ( )´ | disturbance quantity |
| $\overline{(\ )}$ | time mean (steady) quantity |
| $(\dot{\ })$ | derivative with respect to time |
| $(\tilde{\ })$ | FEM model quantity |

## 7.4   Subscripts

| | |
|---|---|
| $\phi$ | in circumferential direction |
| 0 | tuned configuration quantity |
| b | blade specific quantity |
| r | in radial direction |
| rc | in Cartesian mean radial direction |
| z | in axial direction |

## Appendix A    Derivation of the unsteady generalised aerodynamic forces

The differential force $d\vec{F}$ on a blade surface element $d\vec{A}$ can be calculated from the instantaneous static pressure $p$ by

$$d\vec{F} = -pd\vec{A} \qquad (45)$$

For harmonically varying values of the pressure $p = \overline{p} + p'e^{i\omega t}$ and the surface element $d\vec{A} = d\overline{\vec{A}} + d\vec{A}'e^{i\omega t}$, the generalised differential force $d\vec{F}_m^g$ in the direction of the eigenmode $m$ with the complex displacement amplitude $\vec{\Phi}_m$ at this blade surface element is

$$dF_m^g = -\vec{\Phi}_m^* pd\vec{A} \qquad (46)$$

Inserting the exponential approach for $p$ and $d\vec{A}$ yields

$$dF_m^g = -\vec{\Phi}_m^* \left[ \overline{p}d\overline{\vec{A}} + p'd\overline{\vec{A}}e^{i\omega t} + \overline{p}d\vec{A}'e^{i\omega t} + p'd\vec{A}'e^{i2\omega t} \right] \qquad (47)$$

If we define

$$F_m^g = \overline{F}_m^g + F_m'^g e^{i\omega t} + O(2) \qquad (48)$$

where $O(2)$ represents a term of products of disturbance terms $\vec{\Phi}_m^* p'd\vec{A}'$ that is small of second order and is neglected in the evaluation, the unsteady complex amplitude of the differential generalised force $dF_m'^g$ reduces to

$$dF_m'^g = -\vec{\Phi}_m^* \left[ p'd\overline{\vec{A}} + \overline{p}d\vec{A}' \right] \qquad (49)$$

The complex amplitude of generalised force $F_m^g$ for the whole blade can now be obtained by integration over the blade surface $A$ as

$$F_m'^g = -\oint_A \vec{\Phi}_m^* \left[ p'd\overline{\vec{A}} + \overline{p}d\vec{A}' \right] \qquad (50)$$

Obviously, the resulting generalised force consists of two parts. The first is dependent on the unsteady pressure perturbations, this corresponds to the effect of the unsteadiness in the flow field on the aerodynamic forces. As an example, consider an airfoil undergoing torsional oscillations. This motion effectively changes the flow incidence angle on the airfoil, which in turn induces a change in the pressure distribution. The unsteady pressure distribution finally causes a change in the lift and moment acting on the airfoil. The second part is only dependent on the motion of the airfoil and the steady pressure distribution. This term is not so obvious at first glance. Taking the previous example, this effect corresponds to the change of the surface normal direction with the airfoil motion. Since the forces resulting from the steady pressure field always act normal to the surface, this in turn changes the direction in which the steady flow forces act on the airfoil.

**Appendix B    Linearised Euler method**

In the present study, an unsteady 3D linearised Euler flow solver was used to determine the aerodynamic coefficients for vibrating cascades as well as the unsteady generalised forces on cascades due to flow disturbances like wakes or pressure fields.

The solver is the 3D extension of the quasi-3D method presented in [32] and [33]. In this chapter, the fundamentals of the method will be outlined.

**B.1   Fundamental equations**

The method is the linearised unsteady version of a steady Euler method described in [24]. It is based on the 3D Euler equations, thus modelling inviscid flow. The fundamental equations are given in integral form for cylindrical coordinates in a rotating frame of reference. The control volumes $dV$ are assumed to be deforming and moving with the velocities $v_r$, $v_\phi$ and $v_z$ in the radial, tangential and axial directions, respectively.

$$\int_V \left( \frac{\partial \mathbf{u}}{\partial t} - v_r \frac{\partial \mathbf{u}}{\partial r} - \frac{v_\phi}{r} \frac{\partial \mathbf{u}}{\partial \phi} - v_z \frac{\partial \mathbf{u}}{\partial z} \right) dV + \oint_S \left( \mathbf{F}_r dS_r + \mathbf{F}_\phi dS_\phi + \mathbf{F}_z dS_z \right) = \int_V \mathbf{H} \, dV \quad (51)$$

These equations constitute the conservation of mass, momentum and energy, with the conservative variables given in the vector $\mathbf{u}$ as:

$$\mathbf{u} = \begin{bmatrix} \rho \\ \rho w_{rc} \\ \rho r(w_\phi + \Omega r) \\ \rho w_z \\ \rho e_{rot} \end{bmatrix} \quad (52)$$

The second line, constituting one of the momentum conservation equations, is not formulated in the radial direction, which would imply a change of direction with the circumferential co-ordinate $\phi$, but in a Cartesian form in the radial direction at the mean circumferential position $\phi_m$ in the computational domain. The corresponding velocity component is labelled $w_{rc}$. Furthermore, the third equation describes conservation of the moment of momentum in the absolute frame of reference. This formulation was chosen to minimise the source terms arising in the vector $\mathbf{H}$, defined in eq. (56).

The flux vectors $\mathbf{F_r}$, $\mathbf{F_\phi}$, $\mathbf{F_z}$ and the source term $\mathbf{H}$ are then given by

$$\mathbf{F_r} = \begin{bmatrix} \rho w_r \\ \left(\rho w_r^2 + p\right)Co - \rho w_r w_\phi Si \\ \rho r(w_\phi + \Omega r)w_r \\ \rho w_z w_r \\ \left(\rho e_{rot} + p\right)w_r \end{bmatrix} \tag{53}$$

$$\mathbf{F_\phi} = \begin{bmatrix} \rho w_\phi \\ \rho w_r w_\phi Co - \left(\rho w_\phi^2 + p\right)Si \\ \rho r(w_\phi + \Omega r)w_\phi + pr \\ \rho w_z w_\phi \\ \left(\rho e_{rot} + p\right)w_\phi \end{bmatrix} \tag{54}$$

$$\mathbf{F_z} = \begin{bmatrix} \rho w_z \\ \rho\left(w_r Co - w_\phi Si\right)w_z \\ \rho r(w_\phi + \Omega r)w_z \\ \rho w_z^2 + p \\ \left(\rho e_{rot} + p\right)w_z \end{bmatrix} \tag{55}$$

$$\mathbf{H} = \begin{bmatrix} 0 \\ \Omega\rho\left[\left(2w_\phi + \Omega r\right)Co + 2w_r Si\right] \\ 0 \\ 0 \\ 0 \end{bmatrix} \tag{56}$$

The following abbreviations were used:

$$Co = \cos\Delta\phi, \quad Si = \sin\Delta\phi, \quad \Delta\phi = \phi - \phi_m \tag{57}$$

To close the system of equations, an ideal gas is assumed, so that the total internal energy in a rotating frame of reference can be written as:

$$e_{rot} = \frac{1}{\kappa - 1}\frac{p}{\rho} + \frac{1}{2}\left[w_r^2 + w_\phi^2 + w_z^2 - \left(\Omega r\right)^2\right] \tag{58}$$

## B.2  Time linearisation

The time linearisation of the Euler equations, as first used by Ni [45], assumes that the unsteady flow variables can be written as the sum of the steady flow variables plus a small, harmonically varying unsteady perturbation at a known frequency $\omega$:

$$\mathbf{u}(r,\phi,z,t) = \overline{\mathbf{u}}(r,\phi,z) + \mathrm{Re}\left[\mathbf{u}'(r,\phi,z,t)e^{i\omega t}\right] \qquad (59)$$

The unsteady perturbation amplitudes are complex values, carrying the information on magnitude and phase of the disturbances. The same assumption is made for the values of the grid coordinates and for the control volume sizes:

$$
\begin{aligned}
r(t) &= \overline{r} + \mathrm{Re}\left[r'e^{i\omega t}\right] & \phi(t) &= \overline{\phi} + \mathrm{Re}\left[\phi'e^{i\omega t}\right] \\
z(t) &= \overline{z} + \mathrm{Re}\left[z'e^{i\omega t}\right] & V(t) &= \overline{V} + \mathrm{Re}\left[V'e^{i\omega t}\right]
\end{aligned}
\qquad (60)
$$

This approach is then inserted into the fundamental equations given in (51). The flux vectors are expanded into a Taylor-series, and the terms of the same order are collected. The zero order terms, constituting the steady flow Euler equations, cancel out, since the underlying steady flow with no grid deformation exactly fulfils eq. (51). The second and higher order terms are neglected, since they are consisting of products of the disturbance terms, which are already small themselves. Following this argument, the remaining terms, after dropping the common exponential term, constitute the unsteady time linearised Euler equations:

$$\int_V \left(\frac{\partial \mathbf{u}'}{\partial t} + i\omega\mathbf{u}' - \mathbf{D}\mathbf{u}'\right)dV + \oint_S \left(\mathbf{A}\mathbf{u}'dS_r + \mathbf{B}\mathbf{u}'dS_\phi + \mathbf{C}\mathbf{u}'dS_z\right) = R.S. \qquad (61)$$

Note that the unsteady flow perturbation amplitudes $\mathbf{u}'$ are assumed to be *time dependent* in eq. (59), although additionally a harmonic variation in time is assumed. This results in the term $\partial\mathbf{u}'/\partial t$ in the above equation. By this, the linearised Euler equations show a structure much alike to the original non-linear Euler equations, making it possible to use a similar numerical solution scheme for the linearised method. However, this time dependence is more a pseudo-time, since it describes the evolution of a single frequency amplitude only. The pseudo-time mainly fulfils the role of a relaxation parameter in the numerical procedure. Again, this approach was pioneered by Ni [45] and later used in most linearised Euler or Navier-Stokes analyses , e.g. [23], [28], [32].

The matrices $\mathbf{A}, \mathbf{B}$ and $\mathbf{C}$ in eq. (61) denote the Jacobians of the flux vectors with respect to the conservative variables, while the matrix $\mathbf{D}$ is the Jacobian of the source term $\mathbf{H}$ :

$$\mathbf{A} = \frac{\partial \mathbf{F}_r}{\partial \mathbf{u}}\bigg|_{\bar{u}}, \quad \mathbf{B} = \frac{\partial \mathbf{F}_\phi}{\partial \mathbf{u}}\bigg|_{\bar{u}}, \quad \mathbf{C} = \frac{\partial \mathbf{F}_z}{\partial \mathbf{u}}\bigg|_{\bar{u}}, \quad \mathbf{D} = \frac{\partial \mathbf{H}}{\partial \mathbf{u}}\bigg|_{\bar{u}} \tag{62}$$

In detail, the matrices can be written as:

$$\mathbf{A} = \begin{bmatrix} -w_r Ta & \dfrac{1}{Co} & \dfrac{Ta}{r} & 0 & 0 \\[2mm] \rho w_{rc}\dfrac{\partial w_r}{\partial u_1} + \dfrac{\partial p}{\partial u_1}Co & w_{rc} + w_r\left(\dfrac{1}{Co} - \kappa - 1\right) & w_{rc}\dfrac{Co}{r} + \dfrac{\partial p}{\partial u_3} & (1-\kappa)w_z Co & (\kappa-1)Co \\[2mm] -\dfrac{rc_\phi}{Co}\left(w_{rc} + c_\phi Si\right) & \dfrac{rc_\phi}{Co} & wr + c_\phi Ta & 0 & 0 \\[2mm] -\dfrac{w_z}{Co}\left(w_{rc} + c_\phi Si\right) & \dfrac{w_z}{Co} & \dfrac{w_z Ta}{r} & w_r & 0 \\[2mm] w_r\dfrac{\partial p}{\partial u_1} + (u_5 + p)\dfrac{\partial w_r}{\partial u_1} & w_r\dfrac{\partial p}{\partial u_2} + (u_5 + p)\dfrac{\partial w_r}{\partial u_2} & w_r\dfrac{\partial p}{\partial u_3} + (u_5 + p)\dfrac{\partial w_r}{\partial u_3} & w_r(1-\kappa)w_z & \kappa w_r \end{bmatrix} \tag{63}$$

$$\mathbf{B} = \begin{bmatrix} -w_r & 0 & \dfrac{1}{r} & 0 & 0 \\[2mm] -w_{rc}c_\phi - Si\dfrac{\partial p}{\partial u_1} & w_\phi + Ta(\kappa - 1)w_r & \dfrac{w_{rc}}{r} - Si\dfrac{\partial p}{\partial u_3} & Si(\kappa - 1)w_z & Si(1-\kappa) \\[2mm] -r\left(c_\phi + \dfrac{\partial p}{\partial u_3}\right) & rw_r\dfrac{1-\kappa}{Co} & c_\phi + w_\phi + r\dfrac{\partial p}{\partial u_3} & (1-\kappa)rw_z & (\kappa-1)r \\[2mm] -c_\phi w_z & 0 & \dfrac{w_z}{r} & w_\phi & 0 \\[2mm] w_\phi\dfrac{\partial p}{\partial u_1} - \dfrac{c_\phi(u_5 + p)}{\rho} & -w_r w_\phi\dfrac{1-\kappa}{Co} & w_\phi\dfrac{\partial p}{\partial u_3} + \dfrac{(u_5 + p)}{\rho r} & (1-\kappa)w_z w_\phi & \kappa w_\phi \end{bmatrix} \tag{64}$$

$$\mathbf{C} = \begin{bmatrix} 0 & 0 & 1 & 0 & 0 \\[2mm] -w_{rc} & w_z & 0 & w_{rc} & 0 \\[2mm] -rc_\phi w_z & 0 & w_z & rc_\phi & 0 \\[2mm] -w_z^2 + \dfrac{\partial p}{\partial u_1} & -\dfrac{\kappa - 1}{Co}w_r & \dfrac{\partial p}{\partial u_3} & (3-\kappa)w_z & (\kappa-1) \\[2mm] \left(\dfrac{\partial p}{\partial u_1} - \dfrac{u_5 + p}{\rho}\right) & -\dfrac{\kappa - 1}{Co}w_r w_z & \dfrac{\partial p}{\partial u_3}w_z & (1-\kappa)w_z^2 + \dfrac{u_5 + p}{\rho} & \kappa w_z \end{bmatrix} \tag{65}$$

$$\mathbf{D} = \begin{bmatrix} 0 & 0 & 0 & 0 & 0 \\ \Omega\left[2\,Si\left(w_r + \rho\dfrac{\partial w_r}{\partial u_1}\right) - \Omega Co\right] & -2\Omega Ta & \dfrac{2\Omega}{r\,Co} & 0 & 0 \\ 0 & 0 & 0 & 0 & 0 \\ 0 & 0 & 0 & 0 & 0 \\ 0 & 0 & 0 & 0 & 0 \end{bmatrix} \tag{66}$$

Here, the following abbreviations have been used:

$$Ta = \frac{\sin\Delta\phi}{\cos\Delta\phi} = \tan\Delta\phi,$$

$$\frac{\partial w_r}{\partial u_1} = -\frac{1}{\rho Co}\left(w_{rc} + c_\phi Si\right) \tag{67}$$

$$\frac{\partial w_r}{\partial u_2} = \frac{1}{\rho Co}$$

$$\frac{\partial w_r}{\partial u_3} = -\frac{Ta}{\rho r}$$

$$\frac{\partial p}{\partial u_1} = \frac{\kappa - 1}{2}\left\{\frac{1}{Co^2}\left[\left(w_{rc} + c_\phi Si\right)^2 - \left(\Omega r Si\right)^2\right] + c_\phi^2 + w_z^2\right\}$$

$$\frac{\partial p}{\partial u_2} = w_r\frac{1-\kappa}{Co} \tag{68}$$

$$\frac{\partial p}{\partial u_3} = \frac{1-\kappa}{r\,Co^2}\left[w_{rc}Si + c_\phi - \Omega r\right]$$

Finally, the term *R.S.* on the right hand side of eq. (61) holds a number of additional source terms that arise due to the deformation of the control volumes:

$$R.S. = \int_V \left( i\omega\left[r'\frac{\partial\overline{\mathbf{u}}}{\partial r}\bigg|_{\bar r} + \phi'\frac{\partial\overline{\mathbf{u}}}{\partial\phi}\bigg|_{\bar\phi} + z'\frac{\partial\overline{\mathbf{u}}}{\partial z}\bigg|_{\bar z}\right] + r'\frac{\partial\overline{\mathbf{H}}}{\partial r}\bigg|_{\bar r} + \phi'\frac{\partial\overline{\mathbf{H}}}{\partial\phi}\bigg|_{\bar\phi}\right)d\overline{V}$$

$$- \oint_S \left(\left[r'\frac{\partial\overline{\mathbf{F}}_r}{\partial r}\bigg|_{\bar r} + \phi'\frac{\partial\overline{\mathbf{F}}_r}{\partial\phi}\bigg|_{\bar\phi}\right]d\overline{S}_r + \left[r'\frac{\partial\overline{\mathbf{F}}_\phi}{\partial r}\bigg|_{\bar r} + \phi'\frac{\partial\overline{\mathbf{F}}_\phi}{\partial\phi}\bigg|_{\bar\phi}\right]d\overline{S}_\phi + \left[r'\frac{\partial\overline{\mathbf{F}}_z}{\partial r}\bigg|_{\bar r} + \phi'\frac{\partial\overline{\mathbf{F}}_z}{\partial\phi}\bigg|_{\bar\phi}\right]d\overline{S}_z\right) \tag{69}$$

$$- \oint_S \left(\overline{\mathbf{F}}_r dS_r' + \overline{\mathbf{F}}_\phi dS_\phi' + \overline{\mathbf{F}}_z dS_z'\right)$$

This term does not depend on the unsteady flow perturbation amplitudes $\mathbf{u}'$, but only on the steady flow variables and on the unsteady perturbations of the coordinate values. Consequently, this term can be calculated in closed form and stored, once the steady flow and the grid deformations are known.

## B.3   Numerical scheme

### B.3.1  Discretisation

Conforming to the steady Euler solver [24] that was used as a basis for this method, eq. (61) is discretised using a finite-volume cell-vertex scheme. The complex unsteady perturbation amplitudes are then time marched to a "steady" state, corresponding to a purely harmonic oscillation with constant amplitude, where all transients have decayed. This is done using a 3 step Runge-Kutta scheme. Since the time marching is performed in pseudo-time, it is not necessary to use a constant time step throughout the whole computational domain. As a result, local time stepping with individual time steps based on the local CFL numbers are used in all cells.
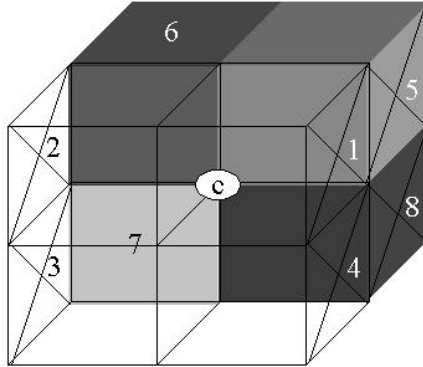


*Fig. 59: Schematic view of the cell-vertex finite volume discretisation.*

Fig. 59 shows a sketch of the discretisation scheme. It shows the 8 hexahedra surrounding a centre node "c". All the geometric and flow variables are stored for the corners of the hexahedra. To calculate the flux balances, fluxes across all surfaces of the mesh are calculated first. This is achieved by averaging the flow variables for the 4 nodes forming one surface and using the resulting values to calculate the flux quantities in the centre of the surface. In a second step, the balances of these fluxes are summed up for all the surfaces belonging to one hexahedron. Finally, the resulting balances of the 8 hexahedra surrounding one node are summed to yield the residual for this node. Multiplying with the appropriate pseudo-time step finally gives the change in the conservative variables.

### B.3.2  Artificial dissipation

The spatial finite volume scheme employed corresponds to a central finite difference scheme. It is second order accurate in space, but it is also unstable for the Euler equations without additional artificial dissipation. The form of artificial dissipation employed in the current method is based on the proposal of Yoon [59], enabling the use of concepts from the Total Variation Diminishing (TVD) methodology in the context of a central finite volume scheme.

The procedure for calculation of the artificial dissipation is implemented as follows:

1) Evaluate pressure sensor

$$DP_i = \left| \frac{\bar{p}_{i-1} - 2\bar{p}_i + \bar{p}_{i+1}}{\bar{p}_{i-1} + 2\bar{p}_i + \bar{p}_{i+1}} \right| \tag{70}$$

2) Determine dissipation scaling factor

$$\alpha_i = \zeta \min \left[ DP_{max}, \max(DP_{min}, DP_i, DP_{i+1}) \right] \tag{71}$$

Here, $\zeta$, $DP_{min}$ and $DP_{max}$ are adjustable parameters

3) Calculate first differences

$$\mathbf{D1}_i = \mathbf{u}'_{i+1} - \mathbf{u}'_i \tag{72}$$

4) Calculate limited third differences

$$\mathbf{D3} = \alpha_t \left( \mathbf{BL}_i - 2\mathbf{D1}_i + \mathbf{BL}_{i+1} \right) \tag{73}$$

with

$$\mathbf{BL}_i = \min \left( |\mathbf{D1}_{i-1}|, |\mathbf{D1}_i| \right) \frac{sign(\mathbf{D1}_{i-1}) + sign(\mathbf{D1}_i)}{2} \tag{74}$$

5) Evaluate scaled dissipation term

$$\mathbf{DF}_i = \mathbf{D3}_i - \mathbf{D3}_{i-1} \tag{75}$$

The resulting dissipative flux term $\mathbf{DF}$ is added to the inviscid fluxes and effectively suppresses numerical oscillations as well as odd/even decoupling (checkerboard mode) of neighbouring vertices.

## B.4  Boundary Conditions

In the current context of a solver for turbomachinery cascade aerodynamics, three distinct types of boundary conditions have to be considered. These are the far-field boundary conditions at the in- and outlet of the computational domain, the solid body surface boundary conditions on the hub, tip and blade surfaces and finally the periodicity boundary conditions on the tangential boundaries of the computational domain that are not formed by solid surfaces. Each of these boundary conditions will be discussed in some more detail below.

### B.4.1  Far-field boundary conditions

In the present analysis, the unsteady aerodynamic forces of a single blade row are to be assessed. In this approach, the interaction of neighbouring blade rows with the unsteady flow field generated on the blade row under consideration is not taken into account. Furthermore, since the computational domain is necessarily limited in the axial direction, boundary conditions need to be applied that take care of the perturbations emanating from the computational domain. Presently, these boundary conditions are set up to minimise the reflections caused on the boundaries, hence they are intended to model the behaviour of an isolated cascade in an infinite duct. The procedure implemented in the current method is based on the work of Giles [20], who derived exact non-reflecting boundary conditions for two-dimensional flows. These are strictly valid for cases where the flow is uniform in the circumferential direction. In the present analysis, these boundary conditions have been applied following Hall et al. [23], where the 2D methodology is implemented for each radial station separately, assuming that the effect of radially varying unsteady perturbations can be neglected. The methodology for each of the radial stations is briefly outlined below, detailed information can be found in the mentioned references.

If the steady flow is homogeneous, the Jacobians in eq. (61) are independent of $z$ and $\phi$. Furthermore, if the unsteady mesh deformations are zero, the right hand side term *R.S.* vanishes. Finally, if all the gradients in radial direction are zero, eq. (61) becomes a linear partial differential equation (PDE) with constant coefficients. This PDE can be cast into the form of an eigenvalue problem and can be solved analytically. The result is a set of four independent perturbation waves for each circumferential wave number. These waves can be identified as up- and downstream travelling pressure waves (two downstream travelling pressure waves for axially supersonic flow), plus one entropy and one vorticity wave, both of which are convected downstream.

As these perturbation waves are independent of each other, it is possible to separate the unsteady flow field at the far field boundaries into these wave components. The values

of the waves travelling out of the domain will be left unaffected, while the incoming waves are set to zero, or to a specified value for the case of a known incoming disturbance.

### B.4.2  Solid surface boundary conditions

On the oscillating airfoils, the inviscid flow remains tangent to the airfoil surfaces at all times. Assuming an arbitrary motion of the airfoils, the boundary condition on the airfoil surfaces is

$$\left( \vec{w} - \frac{\partial \vec{x}}{\partial t} \right) \vec{n} = 0 \tag{76}$$

Here, $\vec{w} = \bar{\vec{w}} + \vec{w}' e^{i\omega t}$ is the surface flow velocity vector, $\vec{x} = \bar{\vec{x}} + \vec{x}' e^{i\omega t}$ is the blade surface position vector and $\vec{n} = \bar{\vec{n}} + \bar{\vec{n}} e^{i\omega t}$ is the unit outward surface normal vector. Under the same assumptions used for linearising the Euler equations, the linearised flow tangency condition reads

$$\left( \vec{w}' - i\omega \vec{x}' \right) \bar{\vec{n}} + \bar{\vec{w}} \vec{n}' = 0 \tag{77}$$

The first term of this equation relates to the equality of the normal velocity between the airfoil and the flow, while the second term is due to the turning of the steady flow with any change in the airfoil normal direction.

### B.4.3  Periodicity boundary conditions

In the present solver it is assumed that all blades of the cascade vibrate in the same modeshape with a constant time lag between the motions of neighbouring blades, i.e. a constant interblade phase angle $\sigma$. This mode of oscillation is also known as a *travelling wave mode*. In this case, a similar condition applies to the flow variables on the circumferential boundaries that are not associated with solid surfaces. Their amplitudes will be equal with a phase shift equal to the interblade phase angle. The application of this boundary condition allows the restriction of the computational domain to a single blade passage without loss of accuracy or generality.

## B.5  Influence coefficients

As pointed out above, the linearised Euler method utilises travelling wave modes for the computation of the unsteady aerodynamics. For the mistuning methodology however, an influence coefficient formulation is more suitable. In this formulation, the aerodynamic

forces generated by a single oscillating blade on all the blades of the cascade are used. Assuming a linear method, these two formulations are completely equivalent and can be readily transformed into one another, as shown for example by Gerolymos [19] or Srinivasan *et al.* [58]. For a cascade with a blade count of $n_{blades}$, an equal number of travelling wave modes exists with interblade phase angles of

$$\sigma_n = \frac{2\pi}{n_{blades}}(n-1) \tag{78}$$

If the corresponding tuned force coefficients are $c_{tuned,n}$, the influence coefficients $c_{k-l}$ can then be calculated from

$$c_{k-l} = \frac{1}{n_{blades}} \sum_{n=0}^{n_{blades}-1} c_{tuned,n} \, e^{\left[i(k-l)\frac{2\pi n}{n_{blades}}\right]} \tag{79}$$

Here, $c_{k-l}$ indicates the force coefficient indicating the force on blade number $k$ due to the oscillation of blade number $l$. Since a periodic cascade has been assumed, the influence coefficients are not dependent on the absolute blade position in the cascade, but only on the distance $(k-l)$ of the current blade from the oscillating blade. In this reasoning, it was assumed that we are dealing with one mode only, hence the influence coefficients here carry no additional index to reference the modes. In case of multiple blade modes being analysed, as described in section 2.2.2, two additional indices are affixed to the influence coefficients, denoting the blade vibration mode that generates the aerodynamic forces and the mode that these forces act on.

## B.6   Validation

The method presented here has been extensively validated over the last years. In [34], comparisons to the experimental and numerical results from the Standard Configurations SC4 [8] and SC10 [59] have been performed. In [36], good agreement has been shown when comparing the numerical results achieved with the current method to experimental data from measurements in an oscillating compressor cascade in sub- and transonic flows. Finally, the application of the current method to aeroacoustic problems in turbines and compressors in [27] and [37] has yielded encouraging results. These validations have shown that the presented linearised Euler solver is able to calculate the unsteady aerodynamic coefficients required in the current mistuning analysis with sufficient accuracy.

### Appendix C    Estimation of sideband intensity effects

In chapter 4, the experimental results of the HP single stage turbine rig were presented and discussed. The response spectra of the rotor blades revealed significant response amplitudes not only for the 43rd engine order (EO) excitation, corresponding to the number of stator vanes, but also for neighbouring EOs, mainly 41st, 42nd, 44th and 45th EO, as shown in Fig. 49. The magnitude of these amplitudes is approximately 20% of the reference mean measured amplitude for 40th though 44th EO. These values indicate that a significant portion of the excitation energy contained in the stator wakes is shifted from the fundamental 43rd EO to the neighbouring, sideband EOs. Consequently, the response to the 43rd EO excitation will be lower than for an ideally symmetric system where no sideband excitations are present. In the following, a simple model for the source of the sideband intensity is presented and the reduction of the fundamental excitation EO relative to an ideal system with no sideband excitation is estimated.

The excitation considered in this case is due to the wakes shed from the stator vanes preceding the HP turbine rotor. If all stator vanes are identical, the rotor blades will pass though identical wake structures 43 times per revolution, so that the excitation spectrum contains only the 43rd EO and multiples thereof. However, small imperfections in the stator vane shape, positioning and stagger angle as well as circumferential variations of the inflow conditions will lead to variations in the width, depth and circumferential positioning of the wakes. The rotor blades passing through these wakes will then not experience a periodic situation for every wake, but only for each revolution. As a result, the excitation spectrum can under these circumstances contain contributions from all EOs. However, since the imperfections and variations around the circumference are probably small, the spectrum will still be dominated by the fundamental 43rd EO.

Two effects are considered especially relevant in this context, namely variations in stator spacing and stagger angle. These variations will induce corresponding variations in the wake positions and hence in the wake sequence that the rotor blades pass through. While a small, say, 1% variation will have an equally small effect on the wake position in the rotor plane, small variations in the stagger angle have a significant influence on the wake position. In Fig. 60, this is shown schematically (note that the stagger angle change is exaggerated to clarify the effect). The large change in the position where the wake impinges on the rotor leading edge is due to the high flow angle at the stator exit (approximately 72° at midspan).
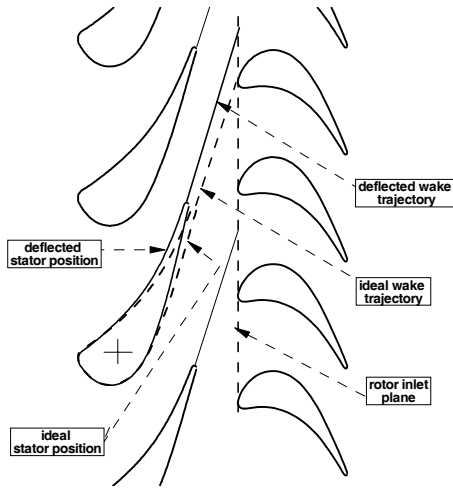
*Fig. 60: Effect of the stagger angle variation on the wake impingement position (schematic, stagger angle variation exaggerated).*

In the present configuration, a change in vane stagger angle of only 0.5° (with an assumed centre of rotation at the centroid of the vane) will result in a shift of the tangential position of the vane in the leading edge plane of the rotor that exceeds 8% of the vane spacing. The large variation of the position where the wake impinges on the rotor translates into an equally large time shift for the unsteady forces acting on the rotor blade when it passes through the wake. When viewed over the whole period of one rotor rotation, this results in significant amplitudes of aerodynamic forces at engine orders different from the fundamental EO.

For the real stator used in the experiments, the actual stagger angle deviations are unknown. To nevertheless quantify the probable effect of the stagger angle variations on the excitation amplitudes at different amplitudes, the following model is used:

- The stator wake is modelled using an analytic wake model, where the wake width and depth are adjusted to match the measured wake profile.
- The stagger angle for each stator vane is stochastically varied using a random number generator with a maximum deviation of ±0.5° from the nominal value.
- The wake position in the rotor inlet plane resulting from each vane is calculated using the mean flow angle and the axial distance of stator and rotor.
- The resulting wakes are joined to yield the flow velocity distribution around the circumference.

- This distribution is Fourier-analysed. The resulting disturbances are normalised using the 43rd EO value resulting from a distribution without stagger angle variations.
- The procedure is repeated for 100 vane stage configurations to give an impression of the statistical distribution of the excitation force spectrum.
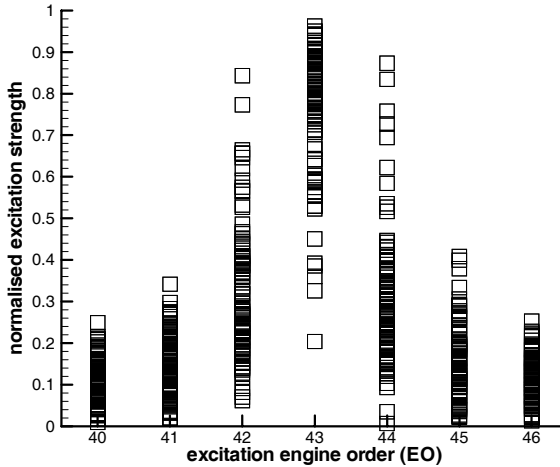


*Fig. 61: Excitation force spectrum at rotor inlet plane, stator stagger angle stochastically varied by*
*±0.5°, 100 stator configurations plotted.*

In Fig. 61, the resulting excitation force amplitudes are plotted for all configurations, showing the EOs 40 through 46. Obviously, there is a large spread of the specific EO amplitudes, depending on the actual distribution of the stagger angles around the stator circumference. In the 100 randomly selected configurations, the fundamental 43rd EO amplitude varies between 20% and 100% of the ideally symmetric value, with a significant clustering of the values slightly below 80%. Similarly, the neighbouring EOs 42 and 44 range from near 0% up to almost 90% (!) of the reference value. For these, typical values seem to amount to 20% - 30%. The 40th, 41st, 45th and 46th EOs range up to approximately 35%, with a bias around 15-20%.

These values resemble the amplitude distribution of the experiment shown in Fig. 49 fairly well, given the fact that only a single feature that is deemed dominant is modelled in this simple approach. Assuming that the values calculated using this model are somewhat typical for the real situation encountered in the experiment, a reduction of the fundamental 43rd EO amplitude to 80% of the ideally periodic case was taken as the reference value for the computations presented in chapter 4.

## Appendix D    Computational procedures and resource requirements

This appendix describes the computational procedures into which the mistuning analysis tool is embedded. Furthermore, indications of typical computational resources required for the individual steps are given.

Regardless of whether a forced response problem is to be studied or whether the aeroelastic stability of a cascade is to be assessed, the unsteady aerodynamic influence coefficients are needed in any case. The schematic of the procedures used to calculate these coefficients is shown in Fig. 62. In this figure, the data sets used are denoted by capital letters A through E, the computational programs are identified by the numbers 1 through 5.
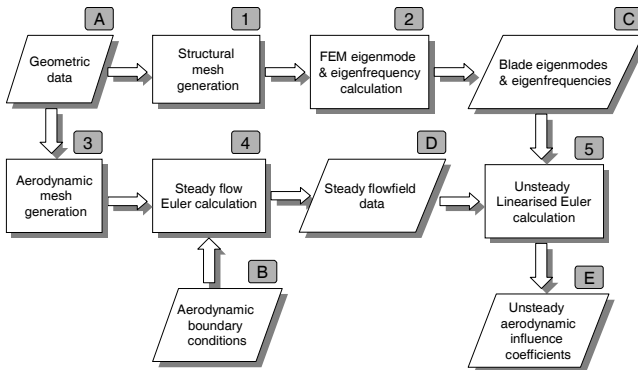


*Fig. 62: Schematic of the procedures used for calculation of the unsteady aerodynamic influence coefficients.*

The fundamental data needed as input to the whole procedure is the definition of the geometry of the configuration to be studied (file "A" in Fig. 62). This information is needed to generate the mesh for the aerodynamic analysis as well as for the structural analysis tools. The structural mesh usually includes the disc for a rotor or the casing for a stator, along with the blade root, the platform, the blade profile and the shroud, if such is present in the configuration studied. Using a commercial mesh generator "PATRAN" (program no. 1 in Fig. 62), the geometry is discretised onto a mesh suitable for the finite

element method (FEM) analysis. This analysis is performed by the commercial FEM code NASTRAN (2). Apart from the mesh file, control information concerning rotational speed, temperatures, type of analysis, requested frequency range etc. has to be input to the program, this is not shown in Fig. 62. In Table 3, the computational resource requirements of all used programs are shown. These relate to a typical case, like the transonic compressor rotor studied in section 3, which will also serve as an example for the other computation steps described below. The CPU times given are approximate values for SGI MIPS10000 processor workstations under the IRIX64 operation system. The speed of these machines is comparable to a PC with 1GHz AMD Athlon processors under the LINUX operation system. It must be noted, however, that this comparison is strongly dependent on the actual programs used. In Table 4, the file sizes of the relevant files used in the computation procedures are listed, giving an indication of the hard disk space required for the complete analysis.

| No. | Program name | Purpose | Unit run | CPU time per unit run | Typical units required | Parallel | memory required |
|-----|--------------|---------|----------|----------------------|------------------------|----------|-----------------|
| 1 | Patran | Structural mesh generator | 1 blade row | 5 min. | 1 | N | 50 MB |
| 2 | Nastran | FEM structural analysis | 1 blade row, 4 eigenmodes | 2 hours | 1 | N | 200 MB |
| 3 | Geo3D | Aerodynamic mesh generator | 1 blade row | 20 sec. | 3 | N | 20 MB |
| 4 | Eul3D | Steady Euler flow solver | 1 blade row | 2 hours | 3 | N | 40 MB |
| 5 | Lin3D | Linearised unsteady Euler flow solver | 1 blade row 1 eigenmode 1 IBPA | 1 hour | 32 | Y | 80 MB |
| 6 | TraceS | Steady Navier-Stokes flow solver | 1 blade row | 5 hours | 3 | Y | 80 MB |
| 7 | Aeval | Mistuning Analysis | 1 blade row w. 16 blades, eigenvalue analysis + frequency sweep | 5 s | 1000 | N | 100 MB |

*Table 3: Typical computational resource requirements.*

For the current case, the structural mesh generation does not require much computational power, although a significant amount of user input is needed. The structural analysis, on the other hand, would complete in approximately 2 hours CPU

time without the need for any user interaction, once the job is started. The result of such an analysis is a binary file containing the lowest blade eigenmodes and eigenfrequencies. The number of eigenfrequencies calculated does not strongly influence the computation time, it does however linearly influence the size of the output file (C), because the deflections are stored for every grid point and every eigenmode.

For the transonic compressor rotor with 2 eigenmodes output on file, the size of file (C) amounts to roughly 10 MB.

| No. | File contents | Typical file size |
|---|---|---|
| A | CAD geometric data (Blade, disc, shroud, platform, firtree, flowpath) | 5 MB |
| B | Aerodynamic boundary conditions | 10 KB |
| C | Blade eigenmodes and eigenfrequencies | 10 MB |
| D | Steady flow field data | 3 MB |
| E | Unsteady aerodynamic influence coefficients | 20 KB |
| F | Wake strength and pressure disturbances | 10 KB |
| G | Unsteady aerodynamic generalised forces | 5 KB |
| H | Mistuning information | 2 KB |
| I | Aeroelastic eigenvalues, response amplitudes | 2 MB |

*Table 4: Typical data file sizes.*

The second program utilising the geometric data is the mesh generator (3) for the aerodynamic solvers. It uses the data describing the blade and flow path (hub and casing) surfaces to generate the structured mesh used by the steady Euler solver. The mesh generation process is using parametric input data that controls the distribution of the grid points. The mesh generation itself is very fast, it takes only approximately 20 seconds of CPU time and usually yields a mesh of sufficient quality after only a few adjustments of the input data.

The resulting mesh is used by the steady Euler flow solver Eul3D (4). As further input, the aerodynamic boundary conditions (B) are needed. These include the inlet flow profile, prescribing total temperature, total pressure and flow direction at the inlet, the static pressure at the outlet and the rotation speeds of the individual blade rows. The steady Euler flow solver is capable of calculating the flow through a whole component, like the complete transonic compressor rig of our example, consisting of rotor, stator and struts.

The computation time as well as the memory requirement of the steady Euler solver scales almost linearly with the number of grid points used in the computation, and hence also with the number of blade rows that are included in the model. Typically, approximately 2 hours of CPU time are needed per blade row, so that for the transonic compressor example 6 CPU hours are needed. The main memory needed is roughly 40 MB. The result of the computation is the complete steady flow field through the component studied. It is stored in one file per blade row (D), containing the co-ordinates, density, pressure and velocity components for each grid point. The size of such a steady flow data file is approximately 3 MB.

The key program in this computation is the unsteady linearised Euler solver "Lin3D", (5), which is described in detail in Appendix B. It calculates the unsteady aerodynamic coefficients for arbitrary blade eigenmodes and arbitrary interblade phase angles with the assumption of travelling wave modes. From a complete set of such travelling wave mode coefficients, the aerodynamic influence coefficients can be derived using a simple transformation, as shown in Appendix B.5. This transformation is not shown in the schematics since it is considered trivial, in the current program structure it is performed in the mistuning analysis program. The linearised Euler solver requires the steady flow data (D) and the blade eigen-modeshape / eigenfrequency information (C) as input, along with some control information (not shown).

The computation is performed using the same mesh as the steady Euler flow solver (4), so that no interpolation or transformation of the steady flow solution (D) is necessary. A single combination of operating point, eigenmode / eigenfrequency and interblade phase angle takes approximately 1 hour to compute, with a main memory requirement of approximately 80 MB. However, usually a large number of such computations are needed. In the present example of the transonic compressor rotor with 16 blades and 2 eigenmodes, 32 computations have to be performed. To keep the wall clock time needed for such a computation down to an acceptable value, the linearised Euler solver (5) was parallelised. In this way, several computations can be performed simultaneously and the turnaround time is significantly reduced. The result of such a set of computations is a file (E) containing the unsteady aerodynamic influence coefficients, or the equivalent travelling wave mode coefficients. The size of such a file (E) is very moderate, at approximately 20 KB.

If the forced response due to wake excitation is to be studied, the strength of the incoming wake and the resulting generalised forces acting on the vibrating blades are needed. The procedure used to calculate these values is shown schematically in Fig. 63.
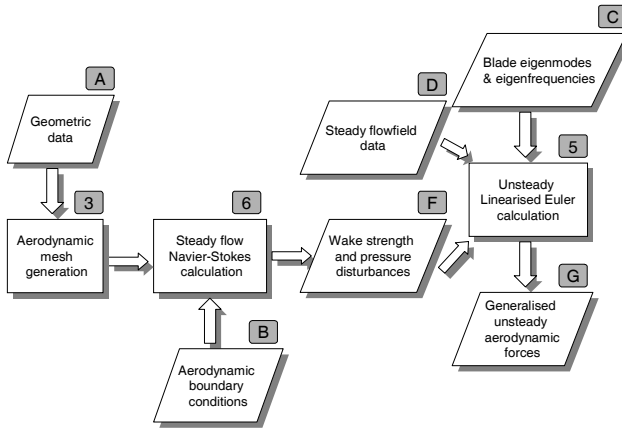
*Fig. 63: Schematic of the procedures used for calculation of the generalised unsteady aerodynamic forces due to wakes or pressure disturbances.*

Since the generation of wakes is an inherently viscous process, it cannot be calculated using an inviscid Euler flow solver. Instead, a Navier-Stokes method is needed. It is however assumed that the wake strength does not strongly depend on the unsteady flow phenomena and can hence be calculated with sufficient accuracy using a steady Navier - Stokes flow solver (6). The procedures used to start such a calculation are not fundamentally different from those to set up the steady Euler flow solver (4). Due to the requirement to resolve the viscous boundary layers that are crucial for the accurate prediction of the wake strength, a finer mesh than for the Euler solver is needed and the CPU and memory requirements are somewhat higher, amounting to approximately 5 hours per blade row. To bring down the computation times, the steady Navier - Stokes flow solver (6) also has the capability to run in parallel on several computers. From the resulting flow field, the wake strength or the pressure disturbances can be found (F), which are then used as input data for the unsteady linearised Euler solver (5). The unsteady linearised Euler calculation yields the generalised unsteady aerodynamic forces (G) due to such wakes or pressure disturbances in much the same way as it yields the unsteady aerodynamic influence coefficients (G) due to the blade vibration described above. When the unsteady aerodynamic influence coefficients (E) as well as

the unsteady aerodynamic generalised forces (G) have been calculated, the mistuning analysis (7) can be started, which is shown schematically in Fig. 64.
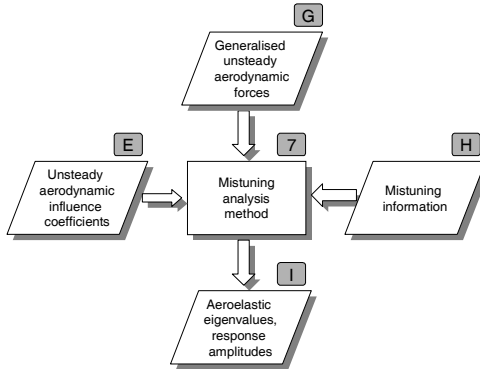


*Fig. 64: Schematic of the procedures used for calculation of the aeroelastic eigenvalues and response amplitudes under the influence of mistuning.*

Additionally, information about the type and strength of mistuning present in the actual configuration is needed. For the current transonic compressor example, one analysis run for a specific configuration is very fast, taking only around 5 seconds of CPU time. This makes it possible to study a great number of configurations in a short time. For the transonic compressor rotor example, the analysis of the 500 randomly mistuned configurations shown in Fig. 43, each computed for 16 excitation interblade phase angles, was completed in as little as 10 hours.

## Curriculum Vitae

| | |
|---|---|
| **Name** | Hans Gerhard KAHL |
| **Date of birth** | 23. Jan. 1962 in Hamburg (Germany) |
| **Nationality** | German |
| **Address** | Försterweg 14 |
| | D-85757 Karlsfeld, Germany |
| **e-Mail** | kahlkarlsfeld@aol.com |

### Education

| | |
|---|---|
| 1980 | Abitur GYMNASIUM MÜSSENREDDER, Hamburg, Germany |
| 1988 | Diplom-Ingenieur Maschinenbau (Mechanical Engineering Diploma), UNIVERSITY OF HANNOVER, Germany |

### Army service

| | |
|---|---|
| 1981 - 1982 | Neumünster, Itzehoe, Hamburg |

### Employment

| | |
|---|---|
| 1983 -1985 | INSTITUT FÜR MECHANIK, UNIVERSITY OF HANNOVER Assistant teacher for undergraduate students |
| 1985 -1988 | MAHRENHOLTZ+PARTNER, Hannover Assistant project engineer, programmer |
| 1988 - 2002 | MTU AERO ENGINES, Munich currently Senior Engineer Aeroelasticity |